Cellulose Nanocrystals:
Size Characterization and Controlled Deposition by Inkjet Printing

Fernando Navarro

Dissertation submitted to the faculty of the Virginia Polytechnic Institute and State University in partial fulfillment of the requirements for the degree of

Doctor of Philosophy

In

Macromolecular Science and Engineering

Maren Roman, Chair

Alan R. Esker

Richey M. Davis

Scott H. Renneckar

Orlando J. Rojas (NC State University)

June 29th, 2010

Blacksburg, VA

Keywords: *Cellulose nanocrystals, Size distribution, AFM, XPS, Streaming potential, Particle alignment, Inkjet printing, Micropatterning.*

Cellulose Nanocrystals:
Size Characterization and Controlled Deposition by Inkjet Printing

Fernando Navarro

Abstract

Inkjet printing has generated considerable interest as a technique for the patterning of functional materials in the liquid phase onto a substrate. Despite its high promise, the phenomena associated with inkjet printing remain incompletely understood. This research project investigates inkjet printing of cellulose nanocrystals (CNCs) as a possible method for the fabrication of cellulose micropatterns. CNCs were prepared from wood pulp by H_2SO_4 hydrolysis and characterized in terms of length, width, and thickness distributions by atomic force microscopy (AFM) and dynamic light scattering. Aqueous CNC suspensions were characterized in terms of shear viscosity with a rheometer. Glass substrates were cleaned with a detergent solution, aqua regia, or a solvent mixture, and characterized in terms of surface chemical composition, surface free energy, polarity, roughness, ζ-potential, and surface charge distribution in air by X-ray photoelectron spectroscopy, contact angle measurements, AFM, streaming potential, and scanning Kelvin probe microscopy (SKPM). Additionally, poly(ethylene glycol)-grafted glass substrates were prepared and characterized in terms of surface free energy, polarity, and roughness. Aqueous CNC suspensions were printed in different patterns onto the different glass substrates with a commercial, piezoelectric drop-on-demand inkjet printer. Inkjet deposited droplet residues and micropatterns were analyzed by AFM, scanning electron microscopy, and polarized-light microscopy. At low CNC concentrations (0.05 wt %), inkjet-deposited droplets formed ring-like residues due to the "coffee drop effect". The "coffee drop effect" could be suppressed by the use of higher CNC concentrations. The resulting dot-like droplet residues exhibited Maltese cross interference patterns between crossed polarizers, indicating a radial orientation of the birefringent, elongated CNCs in these residues. The observed Maltese cross interference patterns represent unprecedented indirect evidence for a center-to-edge radial flow in drying droplets. The degree of definition of the micropatterns depended strongly on the surface properties of the glass substrates. Well-defined micropatterns were obtained on aqua

regia-cleaned substrates. In addition to the surface free energy and polarity, other factors seemed to play a role in the formation of the inkjet-printed micropatterns. If these factors can be identified and controlled, inkjet deposition of CNCs could become an attractive method for the fabrication of cellulose micropatterns.

Keywords: *cellulose nanocrystals, AFM, size distribution, inkjet printing, micropatterning*

Acknowledgements

First and foremost, I would like to thank my advisor, Dr. Maren Roman, for her patience, time, support, and excellent guidance. Without her effort and dedication, this endeavor would not have been accomplished.

I would also like to thank my committee members, Dr. Richey Davis, Dr. Alan Esker, Dr. Orlando Rojas, and Dr. Scott Renneckar, for their many insightful comments and discussions, which have contributed to enrich the outcome of this work. Their willingness to share their experience and knowledge is profoundly acknowledged.

My special thanks go to Dr. Wolfang Glasser for his advice, which encouraged me to start my Ph.D. studies here at Virginia Tech.

I thank my friends and colleagues from the Wood Science and Paper Research Department of the University of Guadalajara, Dr. Juan Ramos, Dr. Rogelio Ramirez, Dr. Lucia Barrientos, M. Sc. Jesús Vargas, and Florentina Dávalos for their friendship, help, and continuous support.

I would also like to thank my fellow research group members, Hezhong Wang, Feng Jiang, Shuping Dong, Chen Qian, and especially my friend Jung Ki Hong, for their help and valuable assistance during the course of this work. Jung Ki and my friend Raquel Mejia-Ariza, from Dr. Davis's research group, I also thank for their friendship and moral support. I would furthermore like to extend my acknowledgements to the staff of the Nanoscale Characterization and Fabrication Laboratory, operated by the Institute for Critical Technology and Applied Science, and the Department of Wood Science and Forest Products for their help and assistance.

This project was supported by the National Research Initiative of the USDA Cooperative State Research, Education and Extension Service, grant number 2005-35504-16088, and by the National Science Foundation under grant numbers CHE-0724126 and DMR-0907567. I also gratefully acknowledge the generous scholarship support for my Ph.D. studies by the Mexican

Secretariat of Public Education (SEP) through its Professional Development for Teachers Program (PROMEP).

Of course, this endeavor would not have been possible without the continuous support and sacrifice of my wife Socorro Navarro, whom I love and cherish dearly. She and my two little angels, Fernando José and Alan Javier, have been the inspiration of my life. I dedicate this work to them.

Finally, but not least important, I would like to express my profound gratitude to my parents, Salvador and Esther Navarro, as well as my brothers. Their unconditional love and guidance has made me the man that I am today, for which I am deeply grateful.

Glossary

γ_e .....Zisman critical surface tension

γ_L and γ_S .....Surface energy of a liquid (L) and a solid (S), respectively

γ_S^D and γ_L^D .....Dispersive component of the surface energy of a solid (S) and a liquid (L), respectively

γ_S^P and γ_L^P .....Polar component of the surface energy of a solid (S) and a liquid (L), respectively

γ_S^+ and γ_L^+ .....Electron-acceptor parameter of the surface energy a solid (S) and a liquid (L), respectively

γ_S^- and γ_L^- .....Electron-donor parameter of the surface energy a solid (S) and a liquid (L), respectively

γ_S^{AB} and γ_L^{AB} .....Polar component of the surface energy of a solid (S) and a liquid (L), respectively, in terms of Lewis acid-base interactions

γ_S^{LW} and γ_L^{LW} .....Polar component of the surface energy of a solid (S) and a liquid (L), respectively, in terms of Lifshitz-van der Waals interactions

Γ .....Decay rate

η .....Solvent viscosity

θ .....Contact angle

π_e .....Film pressure

σ .....Standard deviation

ADSA .....Axisymmetric drop shape analysis

AFM .....Atomic force microscopy

a_p .....Particle major semiaxis

BO .....Bridging oxygen

b_p .....Particle minor semiaxis

BSEs .....Backscattered electrons

CNCs .....Cellulose nanocrystals

d .....Diameter

DDLS .....Depolarized dynamic light scattering

DI .....Dionized (water)

DLS .....Dynamic light scattering

DOD .....Drop-on-demand

DP .....Degree of polymerization

D_R .....Rotational diffusion coefficient

D_T .....Translational diffusion coefficient

E .....East

FCC .....Feedback calculation circuit

FE-SEM .....Field emission scanning electron microscopy

ICC .....International Color Consortium

k_b .....Boltzmann constant

L .....Length

LODP .....Leveling off degree of polymerization

MCC .....Microcrystalline cellulose

N.....North

NBO .....Non-bridging oxygen

NMR .....Nuclear magnetic resonance

P .....Pitch

PDDA .....Poly(diallyldimethyl ammonium chloride)

PEG .....Poly(ethylene glycol)

PLM .....Polarized-light microscopy

P^o.....Vapor pressure of saturation

PSS .....Poly (sodium 4-styerene sulfonate)

RMS .....Root-mean-square

r_p .....Particle radius

r_{tip} .....Tip radius

S .....South

SANS .....Small angle neutron scattering

SAXS .....Small angle X-ray scattering

SE .....Standard error

SEM .....Scanning electron microscopy

SEs .....Secondary electrons

SKPM .....Scanning Kelvin probe microscopy

SLS.....Soda-lime-silica

TEM .....Transmission electron microscopy

W .....West

w_a .....Apparent particle width

W_A .....Work of adhesion

W_A^{AB} .....Work of adhesion due to the Lewis acid-base interactions

W_A^{LW} .....Work of adhesion due to Lifshitz-van de Waals interactions

w_p .....Particle width

XPS .....X-ray photoelectron spectroscopy

Table of contents

Chapter 3

Chapter 4

Chapter 5

Chapter 6

Chapter 7

Chapter 8

List of figures

Chapter 2

Chapter 3

Chapter 4

Chapter 5

Chapter 6

Chapter 7

List of tables

Chapter 2

Chapter 3

Chapter 4

Chapter 5

Chapter 7

Chapter 1

Introduction

Nano-sized materials and structures made of them have attracted tremendous and continued attention for use and study in many technological and scientific disciplines. Owing to their small size, nanomaterials exhibit unique properties and characteristics that differ from those of bulk materials. Many different types of nanomaterials have been developed from both natural and synthetic sources. However, renewable material sources have gained increasing attention in the last decades. In this context, cellulose has enormous potential as a nanomaterial. This non-toxic polysaccharide is abundantly found in nature and possesses a nanofibrillar structure. Cellulose also has other interesting attributes, such as outstanding mechanical properties, low cost, high stiffness, and biodegradability, among others, which make cellulose an interesting material for use in novel and challenging nanotechnology applications. The hydrolysis of cellulose by strong mineral acids gives nano-sized, highly crystalline, rod-like particles. When sulfuric acid is used for the hydrolysis, these rod-like cellulose particles, commonly termed cellulose nanocrystals, exhibit a negative surface charge, which makes aqueous colloidal cellulose nanocrystal suspensions highly stable.

Nano-sized materials have been used in novel applications, such as reinforcing material in composites, device miniaturization, tissue engineering, development of “smart” 3-D structures, and light emitting devices, among others. For many of these applications, the precise deposition of the nano-materials onto various substrates is critical, and very often inkjet printing has been the preferred deposition method. Inkjet printing is a non-impact, rapid, versatile, low cost technology, capable of depositing materials with a high degree of precision. However, application of this technology in the deposition of functional materials presents several challenges, such as colloidal stability, chemical compatibility of the “inks” with the components of the printing device, substrate choice and preparation, and the control of solvent evaporation. Other critical issues include the surface tensions and viscosities of the “inks”, the solid–liquid and solid–solid interactions between the substrate and the often colloidal “inks”, as well as the selection and conditioning of the printing device. For most new inkjet printing-based deposition methods for nano-sized materials, understanding of the above mentioned parameters is important for good printer performance and repeatability of results.

The aim of this project was to develop a fast, precise, and reproducible method, based on inexpensive commercial inkjet printers, for the creation of well-defined cellulose patterns on non-absorbing, glass substrates.

The specific objectives of this project were to:

- ***Select and adapt a commercial inkjet printer for printing of cellulose nanocrystal suspensions***

- ***Determine the properties of cellulose nanocrystals and their aqueous suspensions relevant for their use as an inkjet "ink"***

- ***Determine the properties of suitable printing substrates***

- ***Understand the relationships between "ink" and substrate properties and the morphology of the printed patterns***

- ***Evaluate inkjet printing of cellulose nanocrystals as a method for the fabrication of cellulose micropatterns***

This dissertation is divided into eight chapters. An introduction and a review of the relevant literature are given in Chapters 1 and 2, respectively. Chapters 3 through 7 report, in manuscript format, individual studies of the properties of cellulose nanocrystals and glass substrates and of the factors that govern the morphology of air-dried and inkjet-deposited droplet residues and inkjet-printed micropatterns. The overall conclusions are presented in Chapter 8.

Chapter 2

Literature Review

2. 1. Cellulose

2. 1. 1. Definition and history

Cellulose is a linear homopolysaccharide composed of β-D-glucose pyranosidic units, joined through β-(1, 4) glycosidic linkages. It is an abundant natural polymer and has been extensively used by humans for thousands of years in several forms. Cellulose is utilized as raw material for residential buildings (wood), clothing (cotton and other plant tissues), as well as energy source (wood chips or logs, and energy crops). In addition, cellulose has played an important role in several cultures as a writing material, starting with the use of papyrus by the Egyptians and culminating in the development of modern paper.

Despite its long history of use, it was not until 1838 that cellulose was identified as the main component of cell walls in plants by the French chemist Anselme Payen,[1-2] who found that treatment of several plant tissues with acid and ammonia, followed by extraction with alcohol, water, and ether, gave a fibrous solid with a white appearance. Payen discovered that the chemical composition of the material was approximately 44-45% carbon, 6.0-6.5% hydrogen, and the remainder oxygen. Using these values, he derived the empirical chemical formula $C_6H_{10}O_5$.

Two decades after Payen's discovery, cellulose became an important chemical raw material for the manufacture of synthetic products based on wood cellulose. The first successful cellulose derivative was developed by Hyatt Manufacturing Co. The company used a nitric acid treatment of cellulose to obtain cellulose nitrate (celluloid), which became a widely used thermoplastic polymer. After the successful production of cellulose nitrate, growing interest in cellulose chemistry by the industrial and scientific communities led to intense research in this area. However, it was not until 1926 that the polymeric nature of cellulose was postulated by the German chemist Hermann Staudinger, who utilized a series of non-degrading chemical reactions, as well as osmometry and viscometry, for the determination of the molar mass of the molecule.[3-4]

2. 1. 2. Sources

Using solar energy, water, and carbon dioxide, cellulose is biosynthesized by trees and perennial plants, which represent the main producers of this natural polymer. Cellulose is estimated to be produced at an annual rate on the order of 50 billion metric tons, and it is considered the world's most abundant organic molecule.[5]

Cellulose constitutes between 40 and 60 wt % of dry wood and can account for more than 80 wt % of flax and 90 wt % of cotton. In plants, cellulose is synthesized as structural microfibrils in their cell walls with different microfibril arrangements: a random network of individual elements forming bundles is present in the primary wall, whereas ordered or layer-like structures are found in the secondary wall. Cellulose microfibrils have diameters between 2 and 200 nm and lengths in the range of several microns depending on their origin.[4, 6]

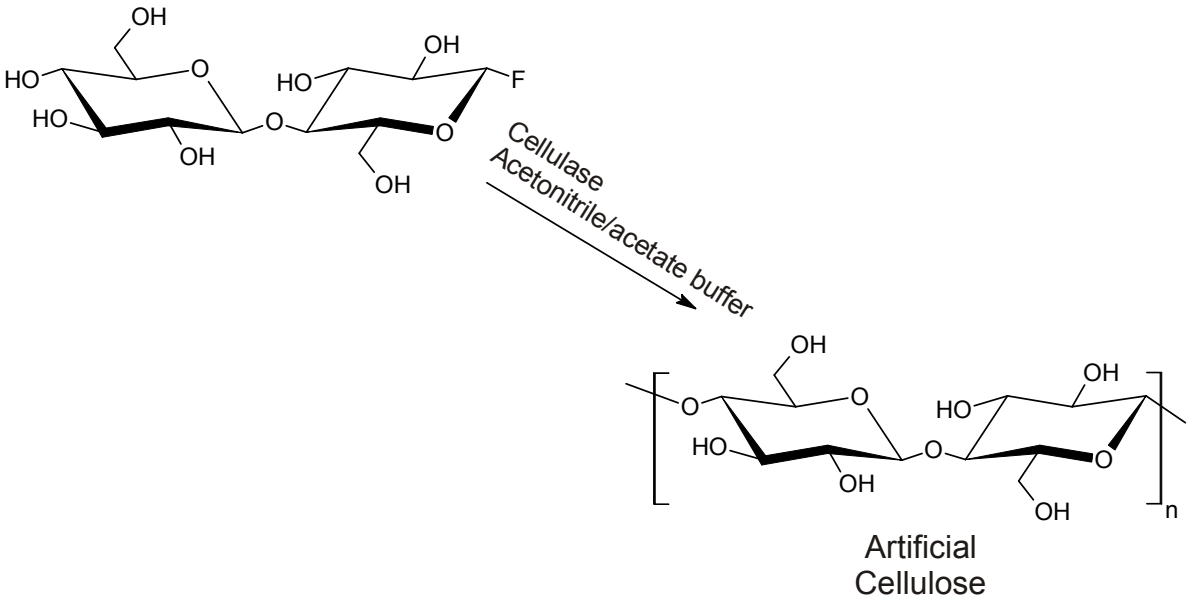

Figure 2. 1. Scheme of the synthesis of "artificial" cellulose in a single-step reaction by polycondensation of β-D-cellobiosyl fluoride. (Reprinted from ref 7 ; fair use, Copyright 2001 American Chemical Society)

The vegetal kingdom is not the only source of cellulose. Certain types of bacteria (such as Acetobacter xylinum) can produce cellulose with high tensile strength, modulus, and crystallinity. Some species of fungi and algae have also been reported as capable of synthesizing cellulose in their cell walls and membranes.[6, 8-9] On the other hand, the first report of successful in vitro synthesis of cellulose was published by Kobayashi et al. in 1992. The group employed an enzymatic process (Figure 2.1) using cellulase and β-cellobiosyl fluoride in a mixture of acetonitrile/acetate buffer to create synthetic cellulose with a degree of polymerization of 22.[10]

2. 1. 3. Chemical structure

Several spectrometric studies have analyzed the conformation of glucose units in the cellulose molecule. The studies have revealed that the glucose residues are in their β-D-pyranosidic form with $^4C_1$-chair conformation (lowest energy conformation) and that they are linked through β–(1, 4) glycosidic linkages. In this arrangement, the –OH groups in the 2 and 3 position, the -CH_2OH group and the bonds forming the glycosidic linkage, are all equatorial.[5]

Figure 2.2 illustrates the molecular structure of cellulose. As is shown, most glucose units in the cellulose molecule are chemically similar, except for the two residues at either end of the backbone chain. The terminal anhydro glucose unit on the left in Figure 2.2 constitutes the non-reducing end of the cellulose molecule, with an equatorial OH group located at position 4, whereas the terminal unit on the right constitutes the reducing end of the cellulose molecule, with an OH group at position 1, which is in equilibrium with the original aldehyde structure of the glucose molecule.

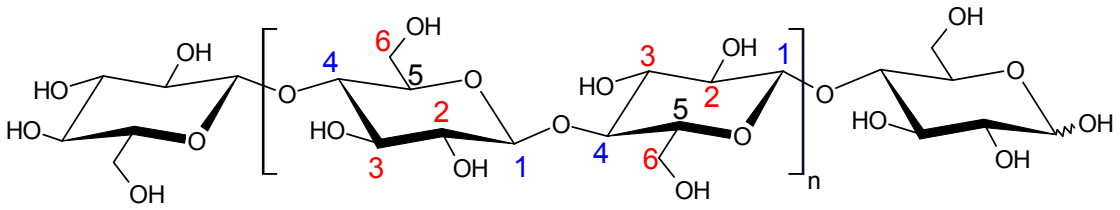

Figure 2. 2. Structure of cellulose.

The basic repeating unit in a cellulose molecule is also depicted in Figure 2.2. The repeating unit, enclosed in brackets, is called "cellobiose" and is composed of two β-D-glucose units rotated 180° with respect to their ring planes. As is also illustrated, cellulose has three hydroxyl groups, located at positions 2 and 3 (secondary), and at position 6 (primary) on each β-D-glucose unit. The primary hydroxyl group is the most reactive group in esterification reactions, whereas the secondary OH positioned at C-2 is the most reactive in etherifications, due to a more acidic nature. The hydroxyl groups of cellulose can interact with each other both intra- and inter-molecularly, leading to the formation of hydrogen bonds with strengths on the order of 25 kJ/mol (approximately 100 times stronger than van der Waals forces).[5]

The intra-molecular hydrogen bonding in cellulose is responsible for the high molecular rigidity of cellulose, its strong tendency to crystallize, and the high viscosity of cellulose solutions. Cellulose is known as a quasi-insoluble compound because of its low solubility in common solvents. Strong acids, metal complexes, or hydrogen bonding systems (e. g., amino based) are among the solvents usually used to dissolve cellulose.[3, 5, 11]

Cellulose is a high molecular weight polymer with different degrees of polymerization (DPs) depending on the source and treatment of the raw material. For example, the DP of cellulose found in wood could be as high as 14,000, in wood pulped fibers it is commonly in the range 300 to 1700, while in cotton and other plant fibers, as well as in bacterial cellulose, the DP of cellulose can be in the range of 800 to 18,000 depending on treatment. As many natural polymers, cellulose is polydisperse and thus, reported DPs are average values.[5, 12-13]

2. 1. 4. Crystalline structure

The first model for the structure of crystalline cellulose was proposed by the Swiss biologists Naegli and Schwender in 1865. Naegli and Schwender postulated that cellulose microfibrils have a "micellar structure" in which the micelles are joined by "glue-like" substances. It was also suggested that the micellar structure had colloidal dimensions. The proposed model of Naegli and Schwender of a "micellar structure" was modified in the 1920s by several researchers, including Hengstenberg,[14] Mark[15] and Meyer et al.,[16] as well as Staudinger, who developed the

concept of the "fringe-micellar" structure. According to the "fringe-micellar" concept, cellulose forms a two phase-network of "micelles" or crystallites and an amorphous matrix.

Figure 2.3 depicts several examples of the "fringe-micellar" concept. The drawings demonstrate how cellulose microfibrils can contain highly ordered segments (crystalline domains) and less organized segments (amorphous zones) with structural imperfections, such as twists or kinks. Cellulose crystallinity has tremendous impact on the overall properties of the material. For example, it governs the chemical and enzymatic accessibility, swelling, and various physical properties of cellulose.[5-6, 17]

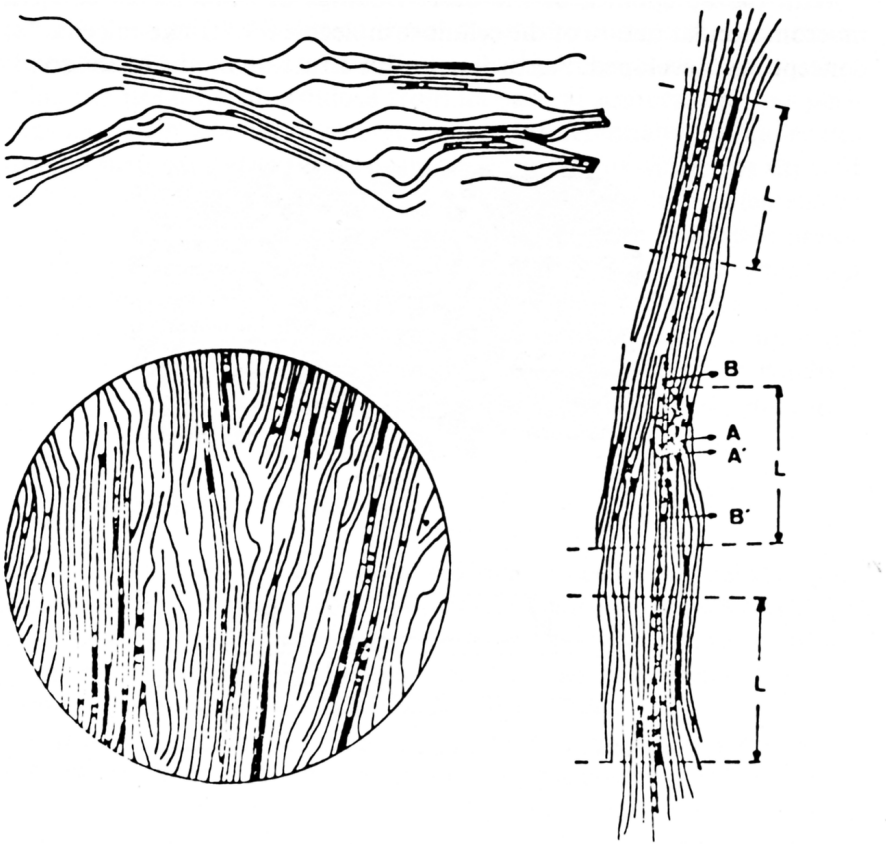

Figure 2. 3. Examples of fringe-micellar models according to Meyer and van der Wyk[16], and Mark.[15] (Reprinted from ref 5; fair use; Copyright 1993 Gordon and Breach Science Publishers).

Meyer and co-workers used cellulose from ramie to study and develop the first crystal structure for native cellulose. They postulated that native cellulose has a monoclinic unit cell containing two parallel chains. However, further investigations by Sarko and co-workers[18] did not support Meyer's results. Sarko et al. used cellulose obtained from the alga Valonia and proposed a triclinic unit cell containing one polysaccharide chain. The monoclinic and triclinic unit cells are depicted in Figure 2.4. In 1984, Atalla and co-workers[19] proposed a new theory based on ^{13}C nuclear magnetic resonance studies. They postulated that native cellulose I is a mixture of two crystal allomorphs: cellulose I_α, occurring in cellulose from algae and bacteria, and cellulose I_β, present in most plants and trees. This theory was supported by subsequent studies by Nishiyama et al.[20-21] and Langan et al.,[22] who used X-ray and neutron diffraction and confirmed the existence of two crystal allomorphs for native cellulose (I_α and I_β).

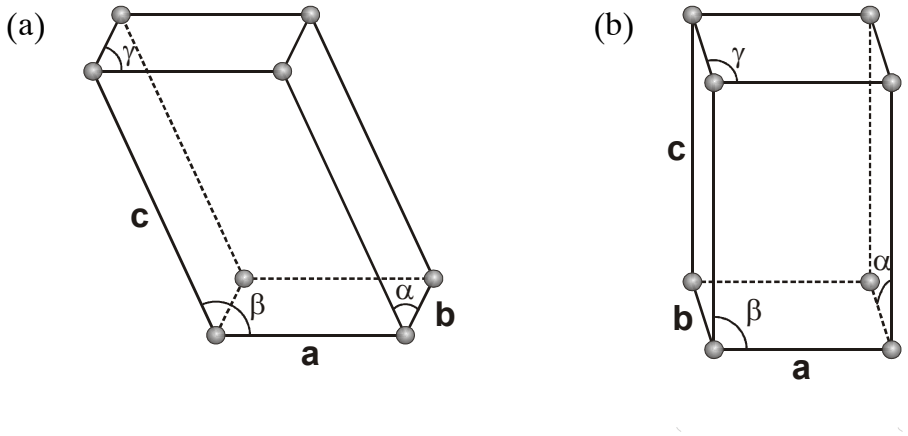

Figure 2. 4. Unit cells of a triclinic (a) and monoclinic (b) crystal lattice.

It is now known that the unit cell of a monoclinic cellulose crystal lattice (I_β), containing two parallel chains, has dimensions of a = 7.760 Å, b = 8.200 Å, c = 10.370 Å (fiber axis), $\alpha=\beta=90°$, $\gamma = 96.62°$,[23] and that of a triclinic lattice (I_α), containing only one chain, of a = 6.717 Å, b = 5.962 Å, c = 10.400 Å, $\alpha = 118.08°$, $\beta = 114.80°$, $\gamma = 80.37°$.[20] The cellulose chains in each of the two allomorphs are densely packed and arranged in sheets. Hydrogen bonding between the sheets was not observed. According to Langan et al.[22], the main difference between cellulose I_α

and I_β is the spatial displacement of the sheets in the chain direction. In addition to the two native allomorphs, when chemically treated, cellulose can adopt additional crystal structures, known as cellulose II, III_1, III_2, IV_1 and IV_2.[17, 21-22, 24]

Cellulose II can be obtained by subjecting native cellulose to a mercerization process or by dissolving cellulose I, followed by precipitation/regeneration of the material as a fiber or film. Cellulose II crystallizes as a monoclinic system having two antiparallel chains, and has dimensions of a=8.10 Å, b=9.05 Å, c=10.31 Å, $\alpha=\beta=90°$, $\gamma=117.1°$. Due to its antiparallel arrangement is thermodynamically more stable than native cellulose.[25-26]

When cellulose I or cellulose II are treated with dry liquid ammonia, cellulose can form cellulose-ammonia complexes and crystallize in a new polymorph after the evaporation of the ammonia. This polymorph is known as cellulose III_1 or III_2, depending of the starting material (native or regenerated cellulose).[26] Cellulose III_1 crystallizes as a monoclinic crystal lattice having one-chain in a parallel fashion, and has dimensions of a=10.25 Å, b=7.78 Å, c=10.34 Å, $\alpha=\beta=90°$, $\gamma=122.4°$.[27] The crystalline structure of cellulose III_2 has been proposed as a monoclinic unit cell with an antiparallel arrangement, however, this structure has not been well defined.[26]

Cellulose IV can be obtained when cellulose III_1 or III_2 are treated with glycerol at 260 °C for 20 min. After treated, cellulose can crystallize as two new polymorphs known as cellulose IV_1 or cellulose IV_2. The crystalline structure of Cellulose IV_1 has not been well defined, Wada et al. [28] argued that this material has the same structure of cellulose I_β but with a lateral disorder due to fragmentation of the cellulose crystallites when the precursor is prepared and subjected to a thermal treatment. The crystalline structure of cellulose IV_2 has been defined as an orthorhombic crystal lattice with an antiparallel chain arrangement, and has dimensions of a=7.99 Å, b=8.10 Å, c=10.34 Å, $\alpha=\beta=\gamma=90°$. It was also reported that such structure resides in an energy minimum, not found in cellulose IV_1.[25-26]

2. 1. 5. Hydrolytic degradation by strong acids (hydrolysis)

Cellulose is sensitive to strong acids, such as sulfuric or hydrochloric acid, which can cleave the β-glycosidic bonds between the glucose units. The anomeric carbon atoms of each glucose residue constitute acetal groups, which are susceptible to ionization, and the resulting carbocation can capture a nucleophile. However, hydrolysis of cellulose is not uniform throughout the polymer because cellulose contains densely packed sections (crystalline domains) with limited access for acid hydrolysis, and less dense packed sections (amorphous region), offering easier access for the hydronium ions. Consequently, in the course of cellulose hydrolysis, the crystalline domains are released.[17]

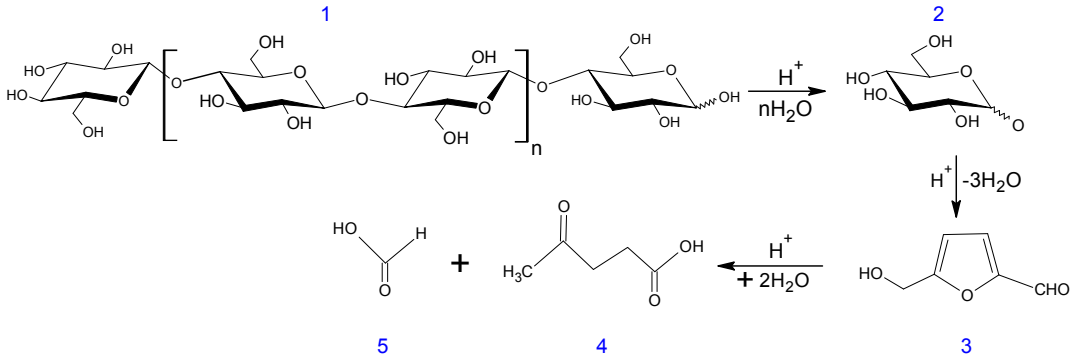

Figure 2. 5. Scheme showing the acid-hydrolysis of (1) cellulose to smaller molecules such as (2) glucose, (3) 5-hydroxymethyl furfural, (4) levulinic acid and (5) formic acid. (Adapted from ref [29]; fair use; Copyright 2007 American Chemical Society).

Figure 2.5 shows the reaction pathway for the hydrolysis of cellulose into smaller molecules by strong acids. First, the cellulose backbone is broken down and reduced to shorter fragments, which are further reduced to glucose if the reaction is allowed to continue. Glucose reacts with the hydronium ions and is converted into 5-hydroxymethylfurfural, levulinic, and finally formic acid. A detailed description of the steps involved in the acidic hydrolysis of cellulose was published by Xiang and co-workers[30] in 2003. The authors stated that the hydrolysis process starts with the interaction of a hydronium ion with the oxygen of the glycosidic linkage, leading

to the formation of the conjugate acid and a cyclic carbonium ion. Finally, when water is added, glucose is liberated.

Acid hydrolysis of cellulose is not a homogenous reaction. Nevertheless, for simplified modeling of the reaction kinetics, it has been assumed to be a series of pseudo-homogeneous reactions, following first order kinetics. The pioneering work in this field was done by Saeman and co-workers in 1945.[31] They proposed that the rate constants (k_i) can be calculated using a slightly modified Arrhenius equation, to include the effect of acid concentration:

$$k_i = k_{io} \times A^{m_i} \times e^{-\frac{E_i}{RT}} \qquad [2.1]$$

where k_{io} is the pre-exponential factor, A is the acid concentration, m_i is the exponent for the acid concentration effect, E_i is the activation energy, R is the universal gas constant, T is the temperature in Kelvin, and i is the reaction index, *1* for hydrolysis and *2* for decomposition.

Equation 2.1 is valid for any acid used as a catalyst for cellulose hydrolysis. However, subsequent studies showed that the model used by Saeman et al. was not optimal and some modifications were suggested. One notable modification was proposed by Malester et al.[32] in 1992, who developed a model that uses pH instead of the acid concentration as shown by the following equation:

$$k_i = k_{io} \times e^{\left[-\frac{E_i}{RT} - 2.303 m_i (pH)\right]} \qquad [2.2]$$

According to the authors, equation 2.2 gives more accurate reaction rate constants.

Studies involving acid-catalyzed hydrolysis of cellulose have employed the following two approaches: (a) low acid concentration (0.05-0.07%) and high temperature (170-240 °C), and (b) high acid concentration (31-72%) and low temperature (20-50 °C). The first method has

primarily been used for studies of reaction mechanisms and kinetics, whereas the second method dominates studies involving the preparation of nanoscale cellulose particles.

Several groups[33-35] studying the hydrolysis of cellulose by dilute acid have found that the depolymerization of cellulose initially proceeds rapidly but then slows down until it reaches a "leveling off degree of polymerization" (LODP). This LODP is related to the accessibility of the starting material to acid during the hydrolysis reaction and therefore to the arrangement of amorphous and crystalline domains. Thus, the LODP depends on the origin of the cellulose used in the hydrolysis reaction, for example, Battista et al. [34, 36] reported LODP values in the range of 140-170 for kraft pulps and 190-270 for sulfite pulps.

Different acids have been used for the hydrolysis of cellulose, however, the most common are sulfuric and hydrochloric acid. Sulfuric acid has been used in both dilute form for kinetic studies and concentrated form for the preparation of cellulose nanocrystals. Concentrated sulfuric acid is the preferred acid for the preparation of cellulose nanocrystals because it causes rapid cellulose degradation without causing swelling of the crystalline domains. Because the amorphous domains are degraded more rapidly than the crystalline domains, the latter can be isolated by terminating the hydrolysis before degradation is complete.

Xiang et al. investigated the effect of sulfuric acid concentration and temperature on the degradation of α-cellulose. α-cellulose is the insoluble portion of a lignocellulosic material subjected to concentrated sodium hydroxide.[37] Depending on the H_2SO_4 concentration, they observed anything from no change in the cellulose sample to a drastic modification of the physical state. Figure 2.6 shows the hydrolysis profiles for different acid concentrations. At 60 wt %, cellulose degraded slowly, whereas degradation was rapid at 65 wt %.[38]

In addition to depolymerization, H_2SO_4 causes esterification of the more accessible hydroxyl groups on the surface of the remaining crystalline domains. Figure 2.7 illustrates the esterification reaction. The introduction of sulfate groups to the surface of the crystalline cellulose domains generates nanoparticles with a negative surface charge, resulting in enhanced

colloidal stability through electrostatic repulsion in aqueous media. These colloidal suspensions have been the basis for numerous studies, including the present work.[38-41]

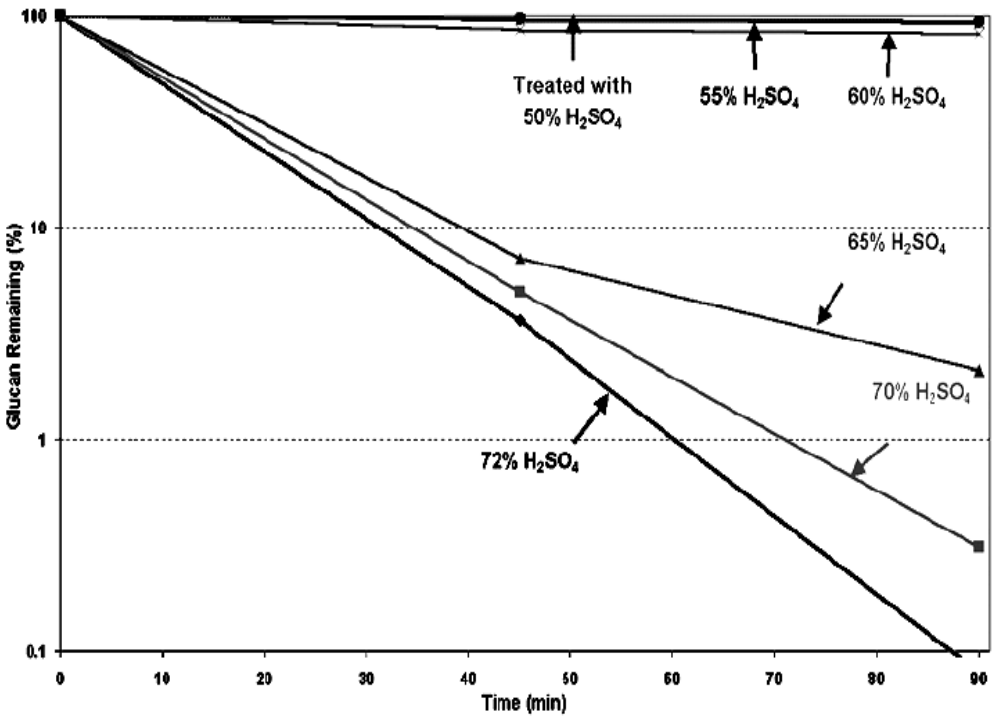

Figure 2. 6. Hydrolysis profiles of α-cellulose treated with various concentrations of H_2SO_4. (Reprinted from ref [38]; fair use; Copyright 1967 Interscience Publishers).

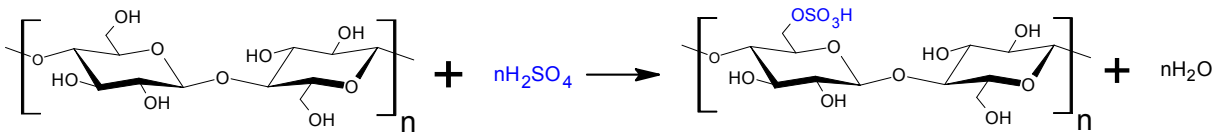

Figure 2. 7. Reaction scheme showing the esterification of the hydroxyl groups of glucose units when sulfuric acid is used as catalyst for the hydrolysis of cellulose. (Adapted from ref 40; fair use; Copyright 2006 American Chemical Society).

2. 2. Cellulose nanocrystals

2. 2. 1. Definition

Cellulose nanocrystals are highly crystalline, rigid, rod-like particles obtained by controlled hydrolysis of cellulose with strong acids. These particles, also known as cellulose whiskers, are very small with lengths between a few hundred nanometers to several micrometers and diameters from <5 to 20 nanometers, depending on the source of cellulose.[17, 24, 42]

The first report of cellulose whiskers was made by Rånby and co-workers[43] in the 1950s. Subsequent research by Battista and Smith[44] in 1961 led to the development and commercialization of microcrystalline cellulose (MCC). MCC is obtained by subjecting cellulose to hydrochloric acid and has found widespread use in the food and pharmaceutical industries. In addition, the properties of cellulose nanocrystals (e. g. mechanical, optical, and morphological) have inspired several research projects.[42]

2. 2. 2. Preparation

Cellulose nanocrystals/whiskers are generally obtained by reacting purified cellulose starting materials with mineral acids, such as sulfuric or hydrochloric acid, using moderate conditions. As mentioned earlier, amorphous cellulose regions are more susceptible to degradation by the hydronium ions than the crystalline regions, because these regions have a less ordered structure and are less densely packed. The most important parameters in the acid-catalyzed hydrolysis of cellulose are the type and concentration of the acid, temperature, and reaction time. The reaction is quenched by the addition of water to dilute the acid, which must thereafter be removed to avoid further cellulose degradation. Generally, centrifugation and extensive dialysis are used for this purpose. The result is an aqueous suspension of cellulose nanocrystals.

Araki and co-workers studied the effects of surface charge on the colloidal stability of cellulose nanocrystal suspensions.[45] They used sulfuric and hydrochloric acids to hydrolyze bleached softwood Kraft pulp and found that the higher surface charge density of the sulfuric acid-treated

samples (84 mmol of sulfate esters/kg of dry material and 26 mmol of carboxyl groups/kg of dry material) compared to the samples treated with hydrochloric acid (< 18 mmol of weak acid groups/kg of dry material) resulted in higher colloidal stability. In a subsequent study, Araki et al.[46] used a post-sulfation process with 55 wt % sulfuric acid to generate a negative surface charge on HCl-hydrolyzed cellulose whiskers and observed a colloidal stability for the post-sulfated suspensions close to that of suspensions prepared by H_2SO_4-hydrolysis.

Around the same time, Dong and co-workers studied the effects of hydrolysis conditions on the surface charge of cellulose nanocrystals.[47] They varied the parameters during the H_2SO_4-hydrolysis of cotton fibers and observed a reduction in length and increase in surface charge with increasing reaction time. Several years later, a similar study by Beck-Candanedo et al.[48] investigated the effects of hydrolysis time and acid-to-pulp ratio on the properties of nanocrystals from hardwood and softwood cellulose. In the case of softwood cellulose, a longer hydrolysis time (45 min.) produced shorter whiskers with lower polydispersity. For both cellulose types, a higher acid-to-pulp ratio (17.5 mL/g) generated whiskers with smaller dimensions. In addition, the hardwood and softwood nanocrystals were found to have similar characteristics and the sulfate groups attached to the surface of the nanocrystals were found to be thermally unstable.

More recently, Elazzouzi-Hafraoui et al.[49] analyzed cellulose nanocrystals from cotton cellulose, tunicate cellulose, and MCC (Avicel) by atomic force and transmission electron microscopy (AFM and TEM), as well as small- and wide-angle X-ray scattering (SAXS and WAXS) and found that the particles were flat with a broad length distribution but with uniform thickness. The differences in observed dimensions from those previously reported by Dong et al.[47] and Araki et al.[45] were attributed to the fact that the particles were aggregates of smaller crystallites and that this fact was not taken into consideration in the previous studies.

The use of statistically designed experiments for the optimization of the hydrolysis reaction parameters and isolation of cellulose nanocrystals was reported by Bondeson et al.[39] in 2006. The group employed response surface methodology (MODDE 7, Umetrics) with acid concentration (H_2SO_4), mass of cellulose starting material (MCC), hydrolysis temperature, hydrolysis time, and

time of ultrasonic treatment as factors, and yield and median particle size as responses. The reaction conditions that maximized the yield while producing a particle size close to 0.15 μm were an acid concentration of 63.5% sulfuric acid, a hydrolysis temperature of 44 °C, and a hydrolysis time of 130 min. Under these conditions, the mean particle size was 0.2 μm (as measured by laser granulometry) and the yield was 30 %. However, it was suggested that the optimum values for the reaction parameters would be different for different cellulose sources. Also, the effect of sonication on the two responses was not obvious and considered a potential topic for future research.[24, 39, 49]

2. 2. 3. Morphology

The morphological aspects of cellulose nanocrystals have inspired numerous studies involving diverse analytical techniques. For example, Heux et al.[50] reported the use of solid state ^{13}C nuclear magnetic resonance (NMR) spectroscopy to investigate the structure of sugar beet pulp microcrystals. NMR spectroscopy was useful to measure cellulose crystallinity under tightly controlled conditions, but it was difficult to extract information about the size of the microcrystals from the NMR results. Terech et al.[51] used SAXS to analyze the shape of cellulose whiskers obtained from tunicate cellulose. They performed measurements at six different concentrations of cellulose nanocrystals and found no particle aggregation within the concentration range used in their study. The cellulose whiskers exhibited rod-like shapes with high aspect ratios and had average dimensions of 5.9 nm (diameter) and 1 μm (length).

De Souza Lima and co-workers reported the use of polarized (DLS) and depolarized dynamic light scattering (DDLS) to analyze the translational and rotational dynamics of cellulose whiskers obtained from cotton and tunicate cellulose.[52] Their results for tunicate whiskers, which were based on the Broersma model,[53-55] were largely in agreement with those of Terech et al., except with respect to whisker diameter, which was more than double that reported by Terech et al. The measured dimensions were 15 and 16 nm in diameter and 255 and 1160 nm in length for cotton and tunicate whiskers, respectively.

AFM is the analytical technique that has probably provided the most detail on the morphology of cellulose nanocrystals. The use of AFM to analyze the structure of cellulose nanocrystals at the sub-nanometer scale was reported by Baker et al.[56-58] High resolution images of cellulose whiskers obtained from the cellulose of the marine alga Valonia ventricosa revealed that the whiskers were straight, cylinder-like particles with corrugations on their surface, and lengths on the order of thousands of nanometers with 20 nm (a few) to 100 nm (majority) diameters. By using real and simulated AFM images, the atomic arrangement on the whisker surface was found to be a mixture of triclinic and monoclinic domains. The AFM studies also revealed the presence of intra-chain periodicities of 0.52 nm, corresponding to the glucose units, and 1.04 nm for the cellobiose units.

Kvien and co-workers[59] used AFM, bright-field transmission electron microscopy (TEM), and field-emission scanning electron microscopy (FE-SEM) to analyze the size and shape of cellulose nanoparticles obtained from MCC and found that the particles had a needle-like shape with thinner diameters at the ends. The measured dimensions were a length of 210 ± 75 nm and a diameter of 5 ± 2 nm. Of the three methods, FE-SEM was found to have insufficient resolution and provided little information about the morphology of the cellulose whiskers.

Table 2.1. Dimensions of cellulose nanocrystals from various cellulose sources. (Adapted from ref 11; fair use; Copyright 2008 Koninklijke Brill NV).

Cellulose type	Length	Width
Tunicate	100 nm-several μm	15 nm
Bacterial	100 nm-several μm	5-10 nm by 30-50 nm
Algal (Valonia)	>1000 nm	10 to 20 nm
Wheat straw	220 nm	5 nm
Cotton	200-350 nm	5-15 nm
Wood	100-300 nm	3-5 nm
Sugar beet pulp	210 nm	15 nm

It is now commonly accepted that the morphology of cellulose nanoparticles depends on the source of cellulose used and the reaction conditions of the acid-catalyzed hydrolysis. In a recent review, Gardner et al.[11] published a collection of typical cellulose whisker dimensions for several cellulose sources, obtained from different literature reports (Table 2.1). As seen in Table 2.1, the length of cellulose nanocrystals ranges from hundreds of nanometers to several microns and the cross-sectional dimension from a few to several tens of nanometers. Nanoparticles obtained from cellulose produced by bacteria, algae, or tunicates exhibit the largest dimensions.

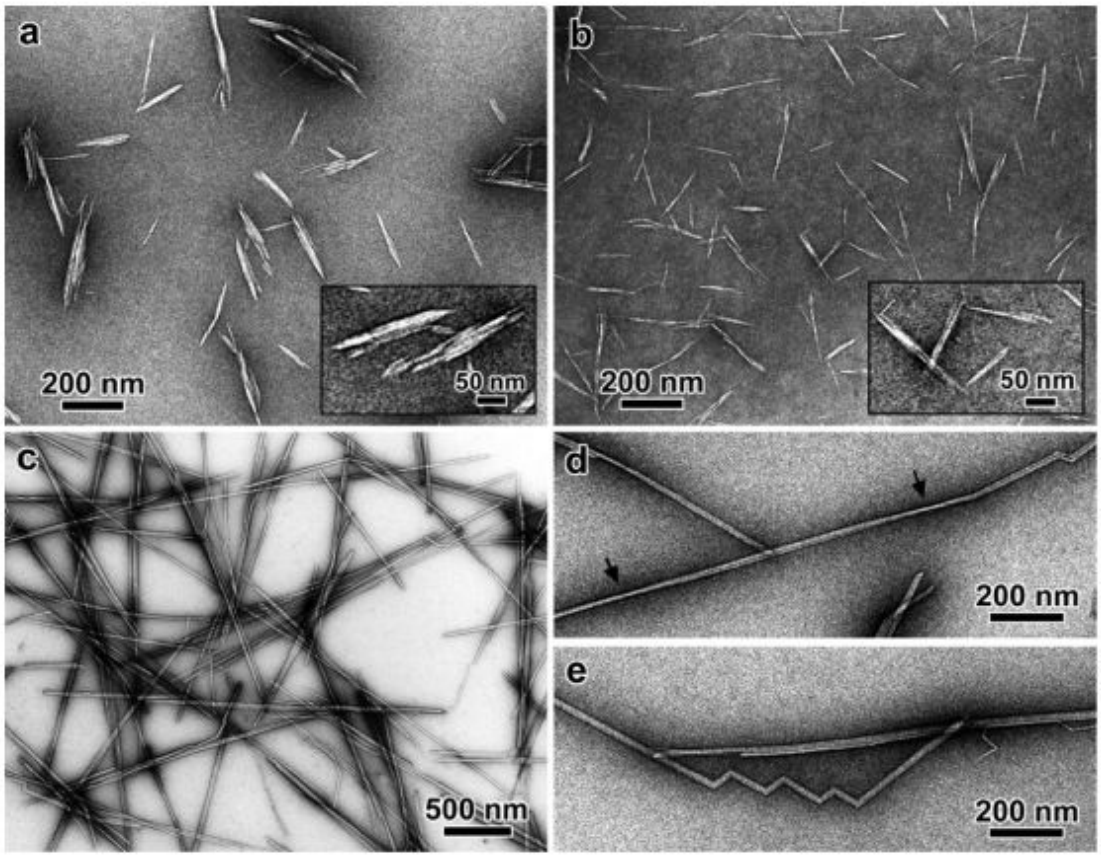

Figure 2. 8. TEM micrographs of negatively stained cellulose whiskers obtained by sulfuric acid hydrolysis of cotton (a), Avicel (b), and tunicate (c-e) cellulose. Insets: enlarged views of some characteristic particles. The arrows in (d) indicate zones where the whiskers are seen edge-on. (Reprinted from ref 49; fair use; Copyright 2008 American Chemical Society).

Figure 2.8 shows TEM images of nanocrystals obtained from various cellulose sources by sulfuric acid-catalyzed hydrolysis. The images clearly illustrate the difference in dimensions of whiskers from different cellulose sources. It is also evident that the shape of the particles varies from needle-like to cylindrical. However, the surface morphology of the nanocrystals is not apparent in these images.

2. 2. 4. Properties

2. 2. 4. 1. Chiral nematic behavior

Several studies have reported that suspensions of cellulose whiskers spontaneously form optically active, chiral nematic (or cholesteric) liquid crystalline phases when the whisker concentration rises above a critical value. Above this concentration, the previously randomly oriented cellulose nanoparticles orient themselves parallel to their neighbors and form a quasi-layered structure in which the direction of orientation rotates slightly from layer to layer in a helical fashion (Figure 2.9).

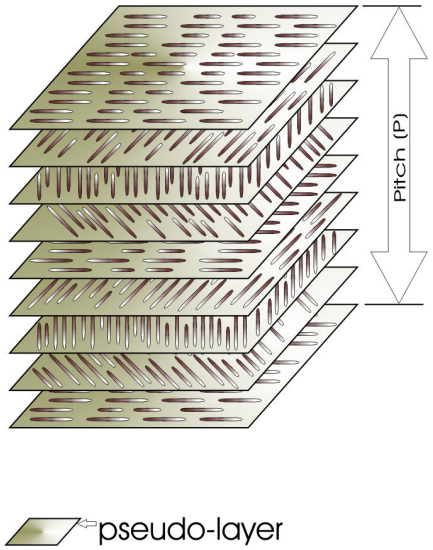

Figure 2. 9. Chiral nematic structure formed by rod-like particles. (Adapted from ref 60; fair use; Copyright 1995 Elsevier Science Limited).

An important property of cholesteric structures is the pitch (P), which is defined as the length, perpendicular to the layers, required for the particles to complete a 360° degree rotation. When the value of (P) from the cholesteric helix coincides with the wavelength of light passing through the material, the structure exhibits selective reflection properties. The pitch of a cholesteric structure is related to the wavelength of the reflected light by the equation proposed by de Vries[61]:

$$\lambda = nP\sin(\phi) \qquad [2.3]$$

where λ is the wavelength of the reflected light, n is the average refractive index, P is the pitch in nanometers, and ϕ is the angle of incidence. According to equation 2.3, as the angle of incidence changes, so does the reflected wavelength, i. e., the color for visible light. Thus, chiral nematic structures, such as those observed in concentrated cellulose nanocrystal suspensions, exhibit iridescent interference colors.[17, 60, 62]

Gray[60] observed that for suspensions of cellulose whiskers, obtained from bleached Kraft wood pulp, the critical concentration was 3 wt %, above which the suspensions form two phases: (a) an anisotropic, i. e. chiral nematic, one located at the bottom of the phase-separated suspension, and (b) an isotropic (randomly oriented) phase, located at the top.[60] Gray reported that these optical properties were also observed in some cellulose derivatives, and were sensitive to many factors, such as the nature of the side-groups, degree of substitution, molecular weight of the cellulose derivative, temperature, type of solvent, and the cellulose derivative concentration.

The chiral nematic order of liquid crystalline phases observed in cellulosic derivatives can be trapped in a solvent-swollen gel after partial removal of the solvent by a variety of techniques, including casting films from a mesophase solution and cross-linking the solvent of the cholesteric phase.[60]

2. 2. 4. 2. Rheological behavior

Due to their tendency to form ordered, liquid-crystalline phases, cellulose nanocrystal suspensions have interesting rheological properties. According to a pioneering study by

Marchessault and co-workers in 1961, the viscosity of H_2SO_4-hydrolyzed cellulose nanocrystal suspensions is independent of shear rate, that is, cellulose nanocrystal suspensions are Newtonian fluids, and the size and length distribution of the particles govern the hydrodynamic properties of their aqueous suspensions.[45]

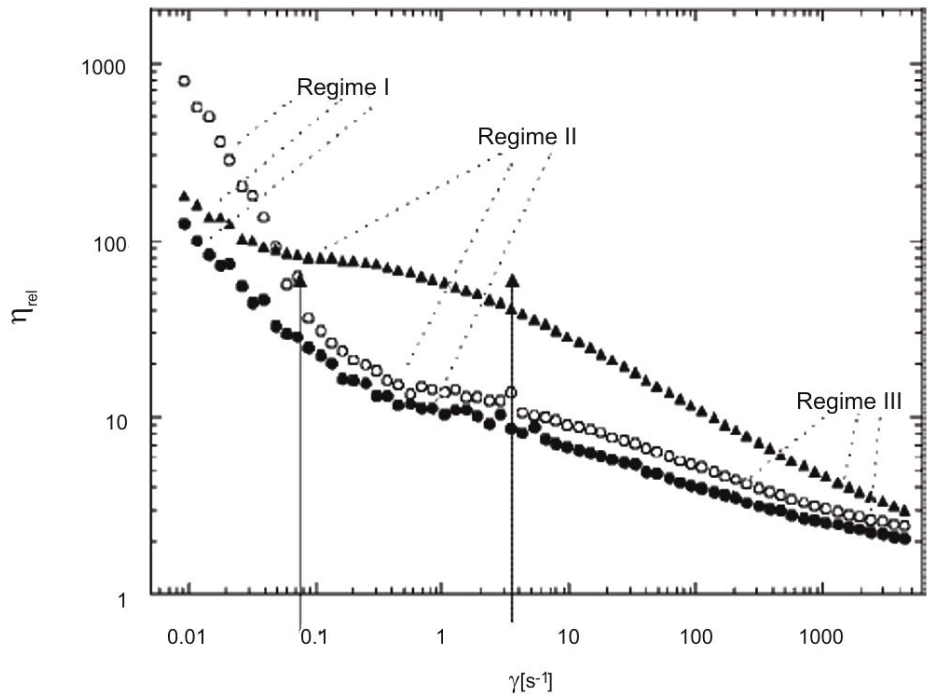

Figure 2. 10. Viscosity versus shear rate for cellulose whiskers from cotton linters at concentrations of (●) 1.2 wt %, (○) 1.7 wt %, and (Δ) 2.7 wt %, showing a shear thinning regime at low shear rates (Regime I), a plateau at intermediate shear rates (Regime II), and a second shear-thinning regime at high shear-rates (Regime III). (Reprinted from ref 17; fair use; Copyright 2004 WILEY-VCH Verlag GmbH & Co. KGaA).

More recent studies by Orts et al.[63] and de Souza-Lima et al.[17], using small angle neutron scattering (SANS) and rheometry, respectively, reported shear-thinning behavior for cellulose nanocrystal suspensions and three different viscosity regimes (Figure 2.10). In Figure 2.10, two shear-thinning regimes, one at low shear rates (Regime I) and one at high shear rates (Regime III), with a plateau at intermediate shear rates (Regime II) are clearly evident. The high

viscosity and shear-rate dependence of regime I were attributed to an initial alignment process of the cellulose whisker domains. The decreased shear-rate dependence of the viscosity in regime II was attributed to the fact that at these shear rates the cellulose whisker domains were largely aligned with the direction of flow. Finally, the increase in shear-rate dependence of the viscosity in Regime III was attributed to the break-up of the cellulose whisker domains and alignment of the individual whiskers.[17]

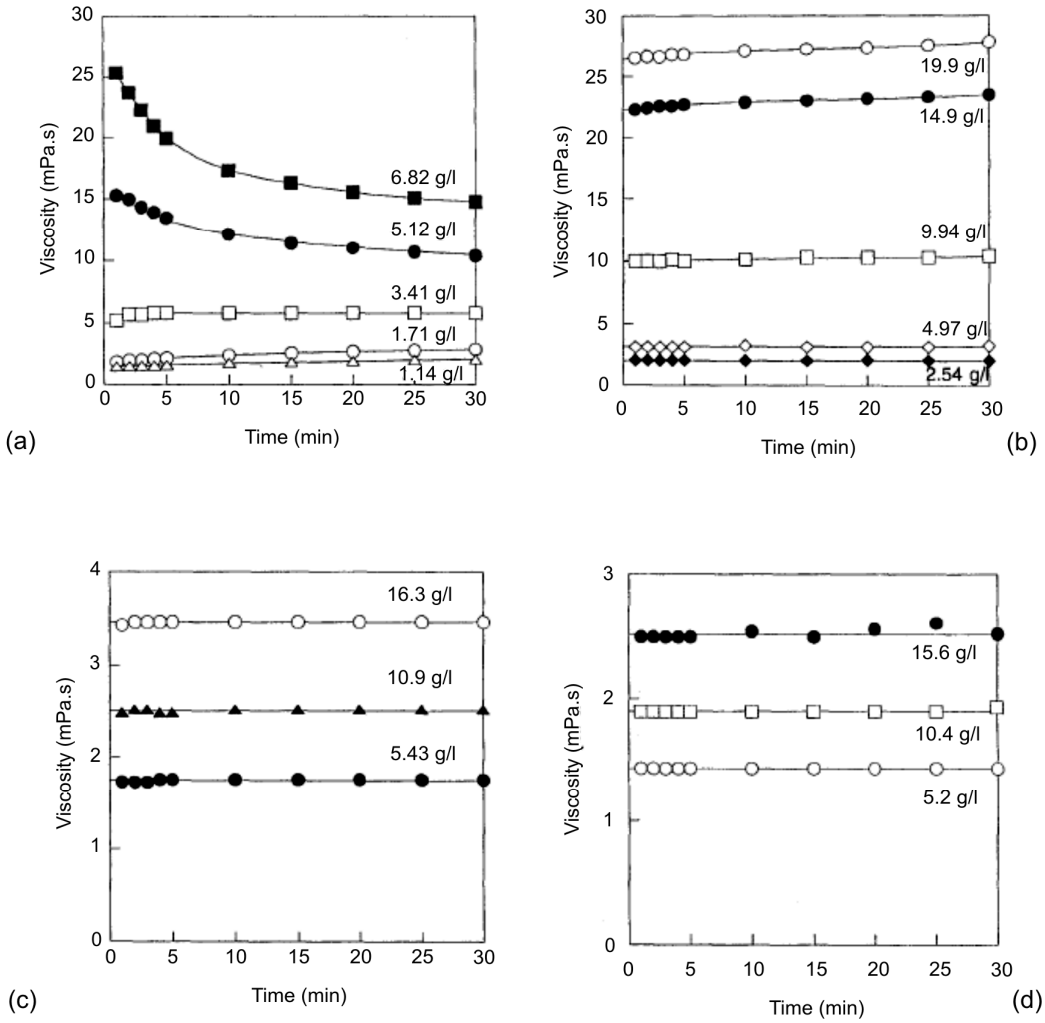

Figure 2. 11. Time dependence of the viscosity of cellulose nanocrystal suspensions: a) HCl-hydrolyzed suspensions, b) Suspensions sulfated at 40°C for 2h, c) Suspensions sulfated at 60°C for 2h, d) H_2SO_4-hydrolyzed suspensions. (Reprinted from ref 46; fair use; Copyright 1999 The Japan Research Society).

Bercea and co-workers[64] studied the rheological properties of the isotropic and anisotropic phases of a biphasic suspension of tunicate cellulose whiskers. The isotropic phase exhibited shear-thinning behavior at low shear rates and Newtonian behavior at high shear rates. The anisotropic phase showed a viscosity regime of low shear-rate dependence located between two shear thinning regimes. For both phases, the decrease in viscosity with increasing shear rate was attributed to shear-induced alignment of the cellulose whiskers.

The effects of surface charge on the rheological properties of cellulose nanocrystal suspensions were studied by Araki and co-workers.[45-46] Different surface charge densities of nanocrystals from bleached softwood Kraft pulp were obtained by hydrolysis with sulfuric and hydrochloric acid and subsequent esterification of the HCl derived nanocrystals with sulfuric acid. Suspensions of HCl-hydrolyzed nanocrystals were shear thickening at concentrations below 5 g/L and shear thinning at concentrations above 5 g/L (Figure 2.11-a). The introduction of sulfate groups via subsequent sulfation drastically reduced the shear rate dependence of the viscosity and produced Newtonian behavior (Figures 2.11-b and 2.11-c) equivalent to that observed for the H_2SO_4-hydrolyzed samples (Figure 2.11-d).

2. 3. Inkjet printing

2. 3. 1. Definition and historical development

Inkjet printing is a technique used to deposit picoliter volumes of ink trough small nozzles onto specific locations on a wide variety of substrates. Inkjet printing differs from other methods in that it is a non-contact, non-impact, versatile, high-speed, multicolor form of printing. By using digital signals from a computer, this technology can create alphanumeric characters, drawings, or images with a wide range of precision levels.[65-66]

The basic operational principle of inkjet printing was described in 1878 by Lord Rayleigh, who demonstrated that a jet of liquid of radius a breaks into small droplets when a disturbance of wavelength $\lambda > 2\pi a$ is introduced.[67] Nevertheless, it was not until 1948 that the Swedish

company Siemens Elema patented the first practical inkjet printer based on analog voltage signals.[66] In 1960, Dr. Richard Sweet from Stanford University developed a process for "continuous inkjet printing", which was adopted by IBM in the 1970s for the mass production of continuous inkjet printers.[68] The continuous inkjet process was also investigated by the Swedish professor Carl Hellmuth Hertz, who developed printing techniques that were able to produce gray scale images by modulating the flow of ink.[69]

An alternative inkjet printing method, the "drop-on-demand" (DOD) method, was developed in the 1970s and early 1980s following the pioneering works of Kyser and Sears,[70] and Zoltan.[71] The DOD method was developed because the continuous method was difficult to accurately control with the existing hardware. However, in the early stages of its development, the DOD method was very unreliable. DOD technology became more precise when Endo and Hara,[72] working for the Japanese company Canon Inc., and some researchers at Hewlett-Packard Inc.[73] developed in parallel the concepts of bubble and thermal inkjet printing, respectively. These technologies solved the problems of low accuracy, poor quality, and nozzle clogging associated with the early inkjet printers. In the mid 1980s, Epson Inc., another Japanese company, developed a DOD technology that used a piezoelectric mechanism. Epson's piezoelectric printers quickly captured a share of the market because of their good performance and reliability. Besides thermal and piezoelectric inkjet technologies, technologies based on electrostatic[74-75] and acoustic[76-77] mechanisms of ink expulsion have been investigated. However, the development of these technologies is still in progress and very few devices have been produced.[66]

Since its invention, DOD inkjet printing has found widespread use in private and commercial printing processes, for example every day reports, digital proofing before a print job on a press, printing on non-paper substrates (e. g., textiles, CD or DVDs), short-run wide format printing. In contrast, the continuous inkjet method has become an excellent industrial tool for high-throughput printing in manufacturing and packaging processes. The different technologies available for continuous and DOD inkjet printing are summarized in Figure 2.12. For each method, four technologies have emerged.[78] In the following sections, both methods will be described further. However, because the continuous method is outside the scope of this review, the corresponding technologies will not be covered in great detail.

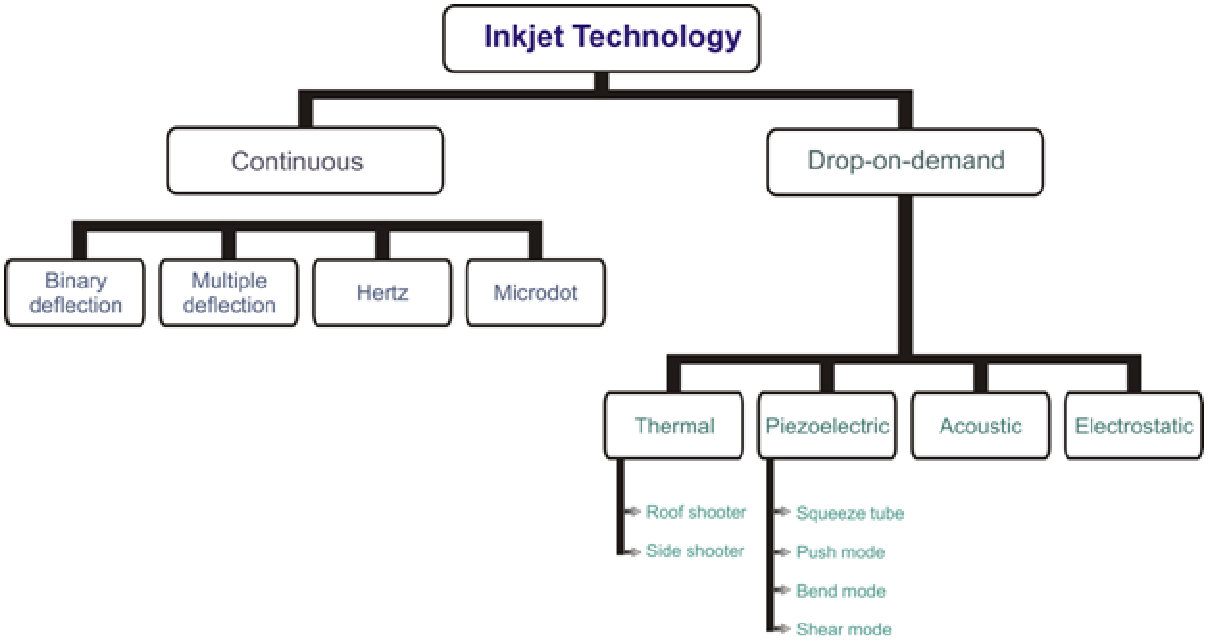

Figure 2. 12. Available inkjet technologies. (Adapted from ref 66; fair use; Copyright 1998 The Society for Imaging Science and Technology).

2. 3. 2. The continuous method

As mentioned previously, the continuous inkjet method is based on the pioneering work of Richard Sweet involving high-speed oscillography.[68, 79] In this process, a pulsed, piezoelectrically-driven ink gun with a small nozzle of 35-80 μm in diameter is used to generate a jet of ink, which breaks up into small droplets. The ink droplets are expelled into an electrical field, generated by applying a pulsed voltage to a pair of electrodes, and to induce a charge to the droplet. The charged droplets then pass between electrically charged deflection plates with a constant potential, commonly in the range of ± 2.5 kV. The charges on both, the droplets and deflection plates, are used to deflect the ink droplet to either the substrate or an ink recirculation system, known as a gutter. Depending on the deflection mechanism, continuous inkjet printing can be binary or involve multiple angles of deflection (Figure 2.13).[65, 78]

(a)

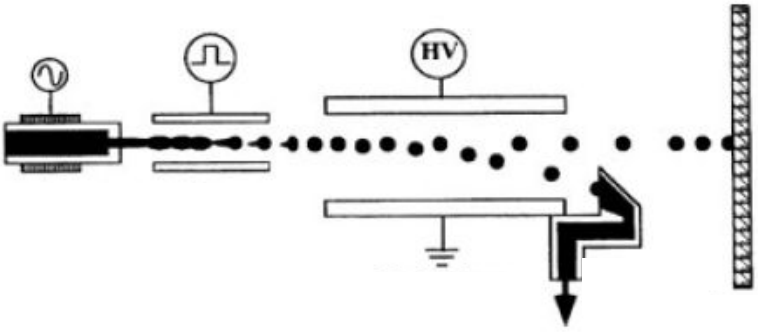

(b)

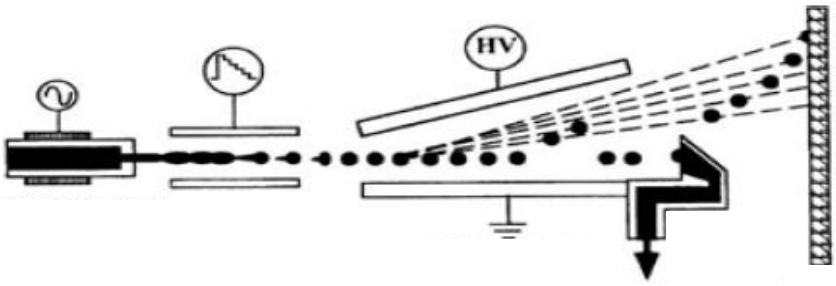

Figure 2. 13. Continuous inkjet systems: (a) Binary-deflection, (b) Multiple deflection. (Reprinted from ref 66; fair use; Copyright 1998 The Society for Imaging Science and Technology).

2. 3. 3. The drop-on-demand method

The DOD inkjet method uses a drop generator that ejects small volumes of ink when a short pressure pulse is applied to a small chamber filled with liquid. The expulsion of ink is discontinuous, occurs only when required, and is controlled through digital signals. DOD inkjet printing is being widely used today for the printing of documents, but is also being studied for novel applications, such as the fabrication of refractive micro lenses from 3D arrays of hybrid organic-inorganic materials,[80-82] conductive structures from metallic colloidal particles,[83-87] organic light-emitting devices from polymers,[88-91] and biochips,[92-96] among others.

As illustrated in Figure 2.12, four major technologies have been developed for DOD inkjet printing: electrostatic, acoustic, thermal, and piezoelectric. This literature review will focus on the thermal and piezoelectric technologies, since most inkjet printers today use one of these two methods.

2. 3. 4. Thermal inkjet technology

Thermal inkjet, also known as Bubble jet, is a DOD inkjet method that uses a thin metallic film mounted to the inside of a micro fabricated ink channel, in the vicinity of the nozzle. When microsecond pulses of electrical current are applied to the resistor, the temperature of the resistor and adjacent ink is raised until it reaches the critical temperature for bubble nucleation. Expansion of the growing bubble causes ink to be expelled trough the nozzle. When the electrical pulse is stopped, the bubble collapses causing retraction of the liquid and rupture of the ink column at the nozzle. The ink volume that gets separated in the process is ejected onto the substrate.

The heat-generating resistors are normally square shaped and have typical dimensions of 5-20 μm. For water based inks, the heating element can cause ink temperatures of up to 300 °C where bubble nucleation occurs. Moreover, expansion of the bubble can cause pressures inside the ink channel of up to 125 atm. In most thermal inkjet print heads, the process of bubble nucleation, expansion, collapse, and ink channel refill takes between 80 and 200 μs.[66, 97]

Two geometries are being used in thermal inkjet print heads, differing in the location of the heating element with respect to the nozzle (Figure 2.14). A configuration in which the heating element is positioned opposite the nozzle is known as “back shooter” and is used in Hewlett-Packard, Olivetti, and Lexmark printers. A configuration in which the heating element is located to the side of the nozzle is known as “side shooter” and is used in Canon and Xerox printers.[66]

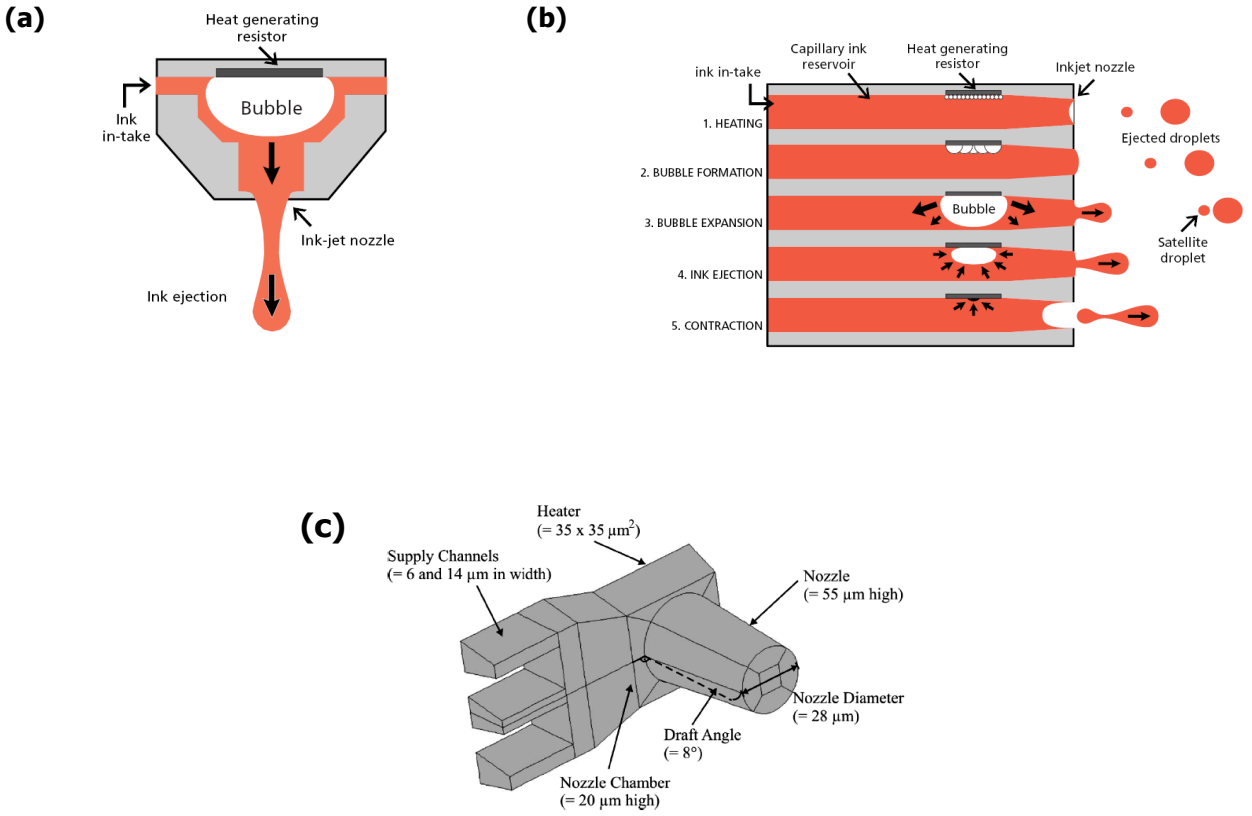

Figure 2. 14. Thermal inkjet print head configurations and specifications: (a) Back shooter, (b) Side shooter, (c) 3-D model of one nozzle with corresponding dimensions. (Adapted from ref 98; fair use; Copyright 2007 IEEE and ref 99; fair use; Copyright 2008 Textile/Clothing Technology Corporation).

Despite its widespread use, some aspects of thermal inkjet technology are still not completely understood whereas others, especially those related to ink formulation and ink head performance, are proprietary information.[100-101]

2. 3. 5. Piezoelectric technology

Piezoelectric inkjet print heads use a voltage-pulsed piezoelectric actuator, which functions as a high pressure generator, to cause the ejection of ink trough a nozzle. Generally, the actuator is made of ceramic material, such as lead zirconate titanate, which can be deformed by short

electrical pulses. Piezoelectric actuators can have different morphologies, with the most common being rods, which elongate, and bimorphs, which bend when an electrical field is applied.[102]

Based on the mode of deformation of the piezoelectric actuator upon application of an electric field, four print head technologies can be distinguished: squeeze, push, bend, and shear. In all cases, the size of the expelled droplet is a function of several parameters, including the mode of deformation of the piezoelectric actuator, the dimension and shape of the nozzle, the duration of the electric pulse, and the applied voltage.

A squeeze mode print head uses a ceramic tube of 1 mm in diameter as the actuator (Figure 2.15-a). The crystal is radially polarized and is connected to electrodes at both ends. The ink channel runs through the actuator. When an ink droplet is needed, an electrical pulse is applied causing the walls of the tube to cave in and "squeeze" ink out of the tube and through the nozzle. The squeeze mode technology is the oldest piezoelectric inkjet technology and was implemented by Siemens on their first printers.[103]

A bend mode print head uses a piezoelectric plate, mounted on top of a diaphragm along one of the side walls of the ink chamber (Figure 2.15-b). When voltage is applied to the crystal, an electric field (parallel to the polarization of the crystal) induces bending of the piezoelectric plate and with it the diaphragm, which in turn pressurizes the ink chamber and causes expulsion of ink through the nozzle. This technology is currently being used in Tektronix and Epson printers.

A push mode print head (Figure 2.15-c) is similar to a bend mode print head in that one of the side walls of the ink chamber consists of a diaphragm. Contrary to the bend mode print head, the actuator in a push mode print head is a rod-like piezoelectric crystal, mounted with one end onto a diaphragm. When voltage is applied to the crystal, the rod extends and pushes against the diaphragm. The incremented pressure in the chamber causes ink to be ejected trough the nozzle. This technology was used in older printers by Trident, DataProducts, and Epson.[103]

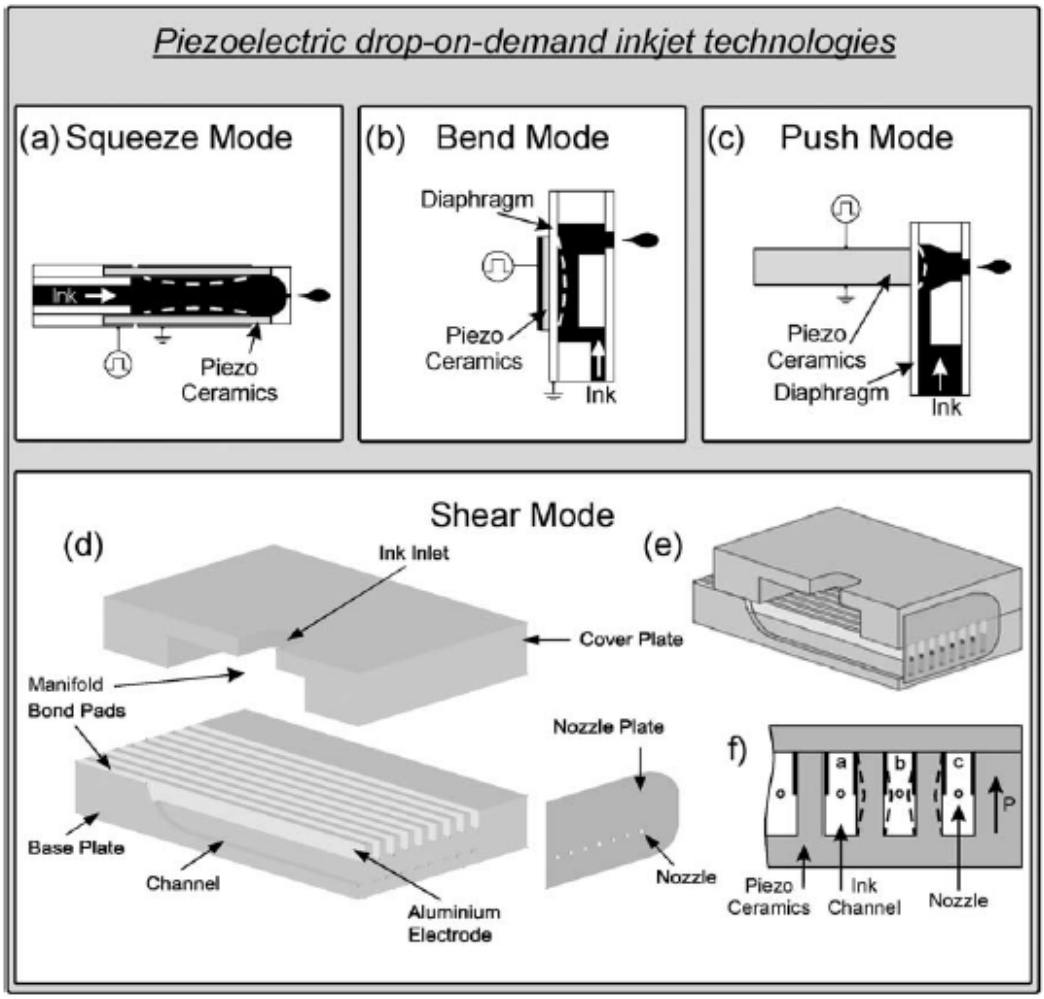

Figure 2. 15. The four main piezoelectric drop-on-demand inkjet technologies. (Reprinted from ref 103; fair use; Copyright 2002 Elsevier Science B. V.).

The most complex technology is the shear mode technology (Figure 2.15-d). This technology uses a piezoelectric base plate containing a series of micro-machined ink channels. The ink channels are generally spaced at ~100 μm intervals and have a rectangular shape, 360 μm deep and 75 μm wide. The upper half of the channels, to a depth of ~160 μm, is covered with a thin layer of metal serving as an electrode. A cover plate, also piezoelectric, containing micro-machined inlets and nozzles is glued onto the base plate. The walls of the ink channels are polarized pair-wise with opposite electrical connections and when an ink droplet is needed,

pulsed voltage signals are applied to the electrodes perpendicular to the direction of polarization of the piezoelectric actuator. The electrical pulse causes simultaneous shear deformation of the two walls of an ink channel toward each other, increasing the pressure in the channel and forcing the ejection of ink droplets. The shear-mode technology was pioneered by the companies Spectra and Xaar.[66, 103]

Regardless of mode of the print head, the expulsion of an ink droplet is the result of an acoustic pressure wave, originated by the actuator in the ink chamber. This acoustic pressure wave moves from its origin at the actuator through the nozzle, overcoming the viscous pressure loss in the small nozzle and the surface tension of the ink. The pressure requirements for ejection of an ink droplet are shown in Figure 2.16.

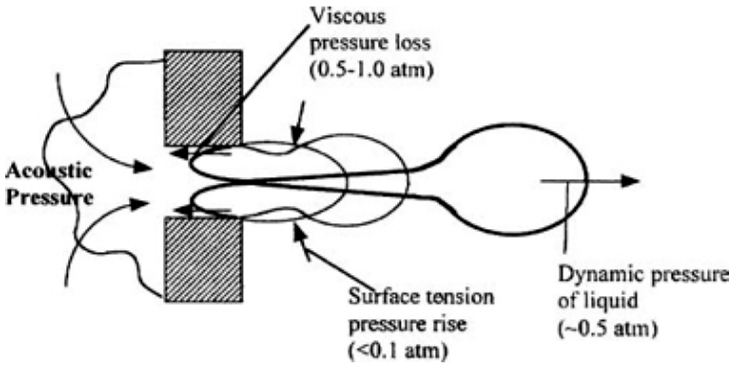

Figure 2. 16. Pressure requirements for the ejection of an ink droplet. (Reprinted from ref 66; fair use; Copyright 1998 The Society for Imaging Science and Technology).

A piezoelectric print head can expel droplets at a frequency of up to 30 kHz, known as the firing frequency. Piezoelectric inkjet printers can be used to print a wider range of materials than thermal inkjet systems because they do not involve the use of heat. Limitations can arise only from the rheological and chemical properties of the inks, as well as the surface tension of the involved solvents. Common piezoelectric print heads can tolerate ink viscosities in the range of 1.6 to 20 x 10^{-3} kg/m·s. The surface tension of the ink should not be less than 35 mN/m, because

lower values cause wetting of the bottom surface of the ink head by the liquid, resulting in fluctuations of droplet quality (shape and size) and problems with ink expulsion. The chemical compatibility of the ink solvent and the print head is another important factor to consider in the selection of a suitable inkjet system for a particular application.[66, 90, 99, 104]

2. 4. Characterization techniques

Various analytical techniques can be used to characterize the surface morphologies and properties of films and substrates, as well as the physico-chemical properties of cellulose nanocrystal suspensions. The research project that is the basis for this review will focus on the following techniques: AFM, SEM, contact angle goniometry, and polarized-light microscopy. However, during the course of the research project, additional characterization methods were used, either as complementary analysis tools or to characterize additional properties.

2. 4. 1. Atomic force microscopy (AFM)

Since its invention in the mid 1980s by Binning, Quate, and Gerber[105], AFM has become one of the most versatile methods for surface characterization. This technique uses special, micro machined, sharp probes to visualize microscopic surface features. Unlike other microscopy techniques (e.g. SEM and TEM), AFM does not require the sample to be under vacuum, and the sample preparation is much less complex. In addition to its ability to image a surface and provide information about the topography of a sample, AFM can measure the mechanical and electrical surface properties, among others.[106-107]

Figure 2.17 illustrates the experimental setup of an AFM. Typically, these systems consist of a micro machined cantilever, with (or without) a pointed tip mounted in a piezoelectric actuator, which allows the cantilever to move up and down (Z direction). The sample is mounted onto a scanner controlled by a pair of piezoelectric actuators, which allows the sample to move in the X and Y directions. AFM uses a deflection system to measure tip displacement and collect topographical data. In addition, there is a feedback control and specialized software that can

convert tip displacement data into an image. The concept of AFM is to bring a sharp probe very close to the sample surface, where it is affected by attractive or repulsive forces. These forces cause a deflection of the cantilever, which is detected normally using one of the following three methods: laser reflection, interferometric or piezoresistive.

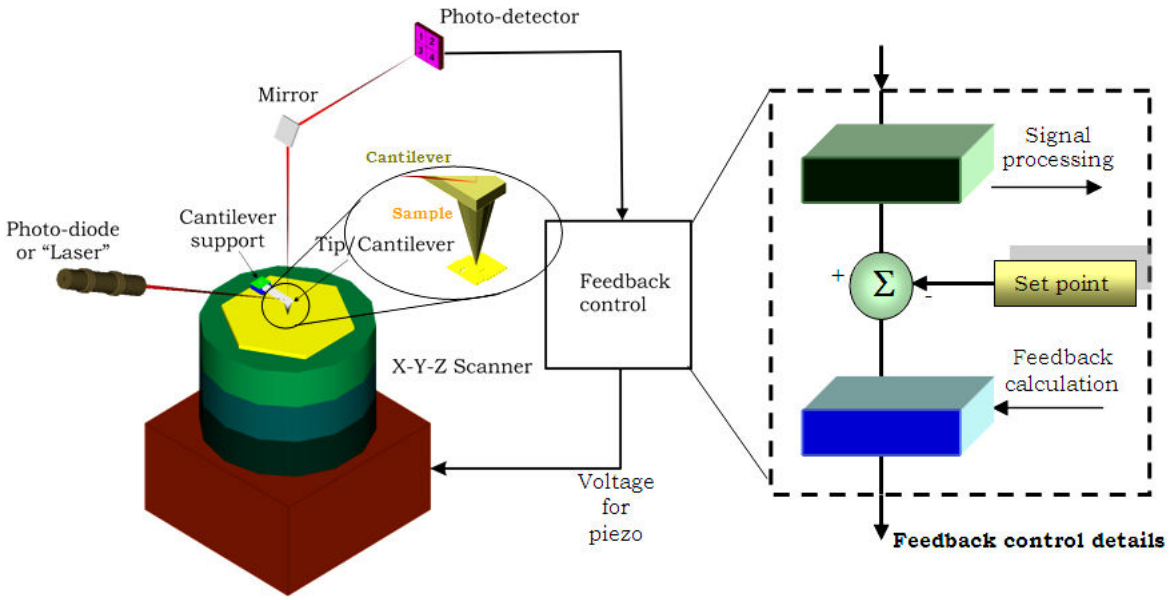

Figure 2. 17. Schematic of a typical AFM. (Adapted from ref 107; fair use; Copyright 2007 Springer Verlag and ref 108; fair use; Copyright 2007 IEEE).

Laser reflection method (used most commonly today): in this technique, a laser beam is focused onto the top surface of the cantilever (near the end that is holding the tip) and reflected into a two- or four-quadrant photo detector, which produces an electrical current. When the cantilever is deflected, the laser position on the photo detector changes. Subtraction of the current generated by the bottom quadrant(s) from that produced by the top quadrant(s) yields information about the cantilever deflection.

Interferometric method: This technique uses an optical fiber to direct horizontally-polarized He-Ne laser light onto the back of the cantilever. A small percentage (~4 %) of the light is reflected back into the fiber by the glass–air interface at the end of the fiber, positioned approximately 10 μm above the cantilever. A fraction of the light that exits the optical fiber is reflected back into the fiber by the cantilever. The deflection of the cantilever, and thus tip displacement, is deduced from the interference between the two reflected components.

Piezoresistive method: This technique employs cantilevers with a piezoresistive coating. This coating is connected to a Wheatstone bridge, which measures its resistance. The resistance of the cantilever coating upon deflection is used to calculate tip displacement.

Most AFMs involve the use of a feedback loop to regulate the distance between the sample and the tip. The feedback loop is a signal processing circuit, which generates a signal that is compared to set point values, and the difference between both values is called the "error signal". The error signal is used as input for the feedback calculation circuit (FCC) and as a representation of sample topography. The FCC controls the separation between the tip and the sample via a high-voltage amplifier and aims to maintain the error signal at a value close to zero.[106-109]

Table 2.2 compares the characteristics of various microscopy methods. According to this comparison, optical microscopy is by far the fastest and least costly method. However, it is also the most limited in terms of resolution (on the order of micrometers). SEM and TEM offer higher resolution (on the order of a few nanometers). However, in contrast to AFM, these methods are restricted by requiring an evacuated sample chamber and the fact that they do not provide three-dimensional information, nor any information about the mechanical, electrical, or magnetic properties of the sample. AFM offers a high resolution (on the order of nanometers to Ångströms), which is only restricted by the characteristics of the tip and configuration of the scanner. The imaging environment is not limited to vacuum, but includes gaseous (mainly air) and liquid sample environments.

Table 2.2. Characteristics of common microscopy techniques for imaging and measuring surface morphology. (Adapted from ref 109; fair use; Copyright 2007 IEEE and ref 110; fair use; Copyright 2004 Veeco Instruments Inc.).

	AFM	SEM	TEM	Optical
Typical Cost (thousands $)	100-200	200-400	≥ 500	10-50
Sample operating environment	Air, gas, vacuum, or liquid	Vacuum *	Vacuum	Air, liquid
Depth of field	Medium	Large	Large	Small
Depth of focus	Small	Large	Large	Medium
Resolution: X, Y	2-10 nm	5 nm	0.2 nm	1.0 μm
Resolution: Z	0.05 nm	N/A	N/A	N/A
Sample preparation requirement	Little or none	Little to substantial	Difficult	Little
Characteristics required for sample	Sample must not have local variations in surface > 10 μm	Surface must not build up charge and must be vacuum compatible *	Sample must be very thin and stained to absorb light, also must be vacuum compatible	Sample must not be completely transparent to light wavelength used

An AFM can be operated using several modes, of which the three most basic are:

Contact mode: The tip is moved across the surface in close contact and the strong repulsive forces between the sample and the tip are monitored to determine the attributes of the sample surface. Contact mode can be carried out by one of two methods. The constant force method maintains a constant cantilever deflection as the tip is moved across the surface, whereas the variable force method allows the cantilever to deflect to different degrees. Due to its potentially destructive nature, this scan mode should not be utilized to analyze soft samples, and small scanning areas should be used to minimize damage to the sample and cantilever. Contact mode requires the use of cantilevers with small spring constants (typically in the range of 0.02-0.2 N/m) and low bending frequencies (around 20 kHz).[107, 109]

Non-contact mode: The tip is positioned at a small distance above the surface, where only attractive van der Waals forces between the sample and the tip are in effect, unless the sample is charged or has magnetic properties. The tip scans across the surface at its natural resonant

frequency and the oscillation amplitude and phase are monitored to determine the sample's topography. Non-contact mode can be used for soft or hard samples because the tip does not touch the surface and therefore is not likely to damage it. However, this scanning mode is more difficult to operate due to the requirements of driving the cantilever in a controlled fashion and accurately measuring its oscillation amplitude, frequency, and phase.[106, 109]

Tapping mode or Alternate Current mode (AC mode): This technique combines features from both contact and non-contact modes. In AC mode, the tip is oscillated near its natural resonance frequency, while it is allowed to intermittently touch the surface. During sample scanning, the oscillation amplitude, phase, and frequency of the cantilever are influenced by the forces between the sample surface and the tip. By measuring the difference between the observed oscillation and a control signal, a topographical image as well as information about the samples surface chemistry can be obtained. AC mode can be used to scan soft or hard samples, and requires tips with large spring constants (commonly 40 to 50 N/m) and high resonant frequencies (on the order of hundred of kHz).[109]

In addition to the basic scanning modes described above, there are other scanning modes that can be used to measure different surface characteristics, such as mechanical, electrical, and chemical surface properties. Most of them will not be used in the research that is the basis for this literature review and will therefore not be described in detail. However, the two techniques electric force microscopy and scanning Kelvin probe microscopy may be used.

In these techniques, a conductive probe interacts with the sample surface through long-range Coulombic forces. Electric force microscopy measures the electric field gradient between the tip and the sample through changes in the amplitude or phase of the oscillating cantilever. On the other hand, scanning Kelvin probe microscopy measures the electrostatic potential of a sample's surface. In this method, a voltage is applied to the tip so that the force experienced by the tip due to differences between the surface potential of the tip and sample is nullified. A plot of this voltage against the in-plane coordinates yields a map of the sample's surface potential.[106]

Another important application of AFM is force-distance measurements. Force-distance measurements monitor the force between the tip and the sample surface as the tip approaches the surface. Figure 2.18 illustrates the characteristics of a typical force-distance curve showing attractive and repulsive regions. As the tip is lowered towards the surface, it first experiences attractive van der Waals forces, causing deflection of the cantilever towards the surface (attractive region in Figure 2.18). As the tip is lowered further the attractive van der Waals forces are opposed by repulsive forces between the electron clouds of the two approaching surfaces, eventually reaching a balance at which the net force is zero (zero cross point). When lowering the tip further towards the sample surface, the repulsive forces dominate the force profile and the cantilever is deflected away from the surface (repulsive region in Figure 2.18).[109]

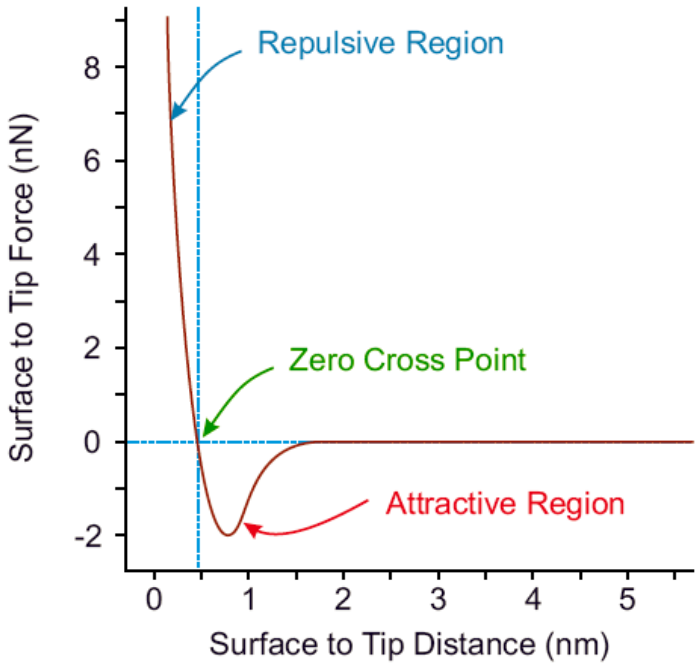

Figure 2. 18. Qualitative example of interaction force versus surface to tip distance. The shape of the curve is determined by the surface and tip properties. (Reprinted from ref 109; fair use; Copyright 2007 IEEE).

As mentioned above, AFM offers several advantages over other microscopy techniques. However, like most analytical techniques, it is susceptible to imaging artifacts, which, in the case of AFM, can arise from one or more of the following sources: the probe, the scanner, vibrations, and image processing. Figure 2.19 shows common AFM imaging artifacts related to the probe and the scanner. As is illustrated in Figure 2.19-a, when the surface features are much smaller than the dimensions of the probe, a broadening effect is seen. However, by using a sharper probe this effect can be minimized. Other artifacts originate from contamination or damage of the probe, causing deformation or duplication of the scanned objects. Moreover, incorrect mounting of the tip and scanner configuration can also cause artifacts, such as lateral broadening or background bow. The latter is due to the fact that the relationship between the measured and real position of the tip in the Z direction is assumed to be linear when, in fact, it is not. Another common artifact is "scanner drift", which is a slow change in scanner position upon a change in ambient temperature (generally an increase).

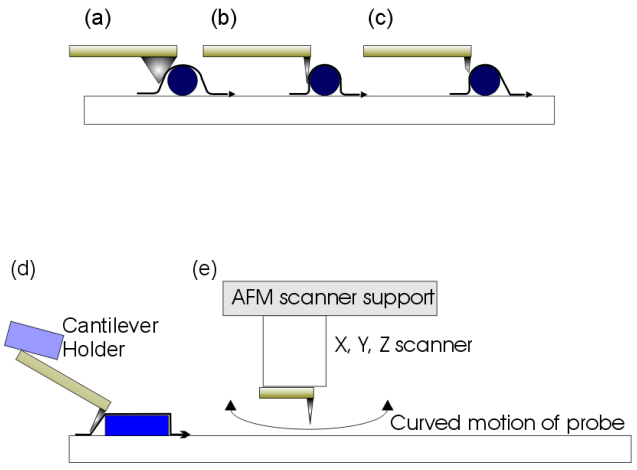

Figure 2. 19. Common artifacts of AFM imaging, a) objects may appear broader than they are when the probe width is large with respect to object dimensions, b) More accurate scanning can often be achieved by using a narrower probe, c) an object's shape may be distorted or objects may appear in duplicate when using a damaged probe, d) one-side broadening of objects may be observed when using an incorrect probe angle, e) the background may appear curved in large-area scans due to a non-linear Z response of the piezoelectric components of the scanner. (Adapted from ref 111 fair use; Copyright 2010 Agilent Technologies).

Vibrations can cause significant oscillations in AFM signals. These artifacts typically are manifested as noise in the image and their origins could be mechanical vibrations, acoustic vibrations, or electrical fluctuations. Yet other types of artifacts can be caused by incorrect off-line image processing, such as improper image flattening and inadequate or excessive application of filters to the image.[112]

2. 4. 2. Scanning electron microscopy (SEM)

The idea of using an electron beam to irradiate samples and obtain images with sub-micron scale resolution, well below the resolution of conventional light microscopy, was that of H. Stintzing and was developed into an electron beam scanner by Knoll in the 1930s. Since then, SEM has become a very popular technique for the characterization of sample surfaces and chemical composition. In SEM, a beam of electrons with a spot size of up to 2 nm is moved in a raster fashion across a sample in an evacuated sample chamber.

A diagram of the configuration of an SEM is shown in Figure 2.20. Electrons are emitted by an electron gun, consisting of a cathode, anode, and a Wehnelt cylinder. The emitted electrons are accelerated by applying a potential across the cathode and anode, on the order of 0.5 to 30 kV. Depending on the microscope, the electrons are emitted and accelerated in low, high, or ultrahigh vacuum. The applied voltage generates a stream of electrons with a spot size between 10 and 50 μm, which is too large to produce sharp images. The spot size is reduced from 10 to 1 nm, for high resolution images, through electromagnetic condenser lenses, which collimate the electron beam. Finally, the electron beam is focused onto the sample surface by one or two objective lenses. Movement of the electron beam in a raster across the sample surface is achieved through the use of one or two electromagnetic deflection coils.

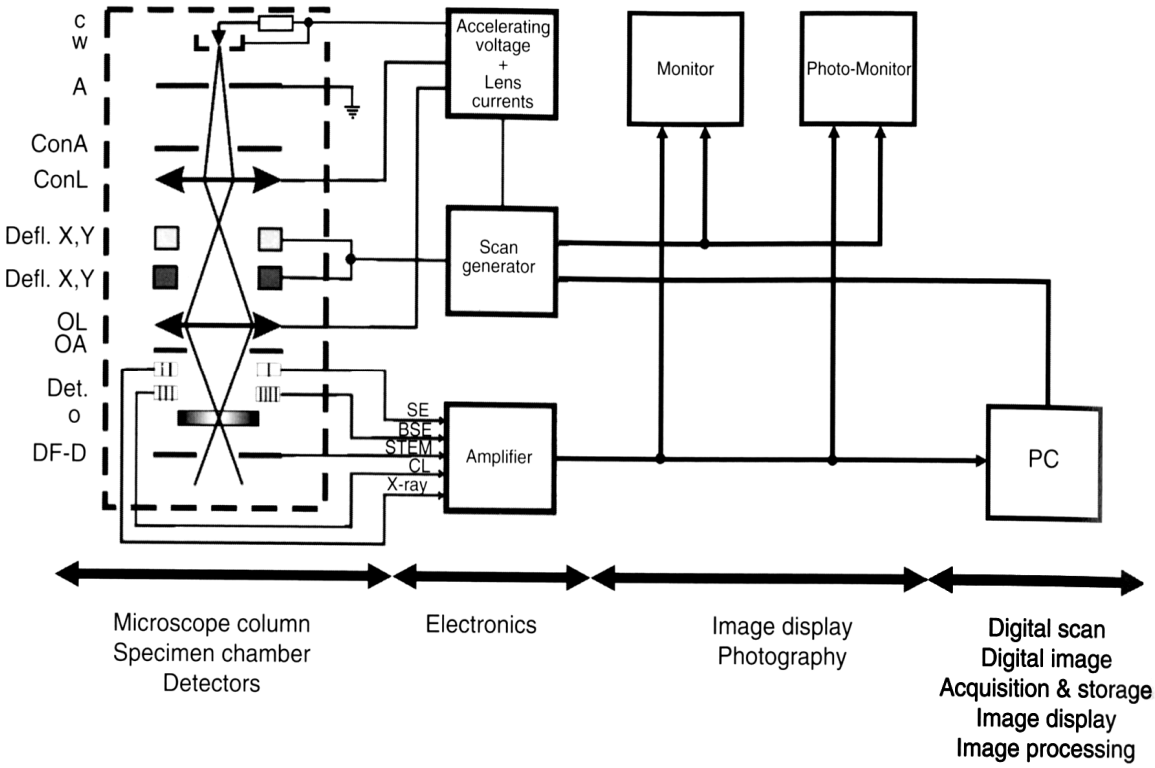

Figure 2. 20. Schematic drawing of a conventional scanning electron microscope. (Reprinted from ref 113; fair use; Copyright 2007 Springer Verlag).

In SEM, several signals are generated when the accelerated electrons hit the sample surface (Figure 2.21). These signals depend on the specimen-electron beam interactions and contain different types of information about the sample. As shown in the scheme in Figure 2.21, most of the primary electrons are elastically and inelastically scattered with deflection angles (θ) less than 90° ("forward" scattering), however, a small fraction of the primary electrons are scattered with θ>90°, or backscattered. The backscattered electrons (BSEs) are the result of several elastic collisions involving a very small energy exchange, thus their kinetic energy is very similar to the primary-electron energy when they escape from the specimen. The number of BSEs released from the sample has a strong relation with the atomic number of the chemical components of the sample, thus the BSE signal can be used as image contrast due to the sample chemical composition.

Besides the BSEs, the primary electrons can also interact with the sample atomic electrons (inelastic collisions), experiencing a repulsive force between the two particles. This repulsion force can release atomic electrons that are weakly bound (outer-shell electrons) to an atomic nucleus, allowing them to escape and travel through the sample as secondary electrons (SEs). The energy (E) gained by the SEs as a result of the inelastic collisions is far below the kinetic energy values of the primary electrons, for most SEs the value of E can fluctuate between 10 and 50 eV. The low levels of E reduce the possibility of a SE from reaching the vacuum environment because they interact with other particles along their path and lose energy until they recombine within the analyzed specimen. Only those SEs released near the surface and traveling toward the sample surface, may escape into the vacuum environment and be collected by the SEM detectors. SE signal is strongly related to the surface structure, therefore it provides a topographical contrast in the SEM image of the analyzed specimen. In addition to SEs and BSEs, Auger electrons, electromagnetic radiation (cathode luminescence), and X-rays are emitted by the sample.[114]

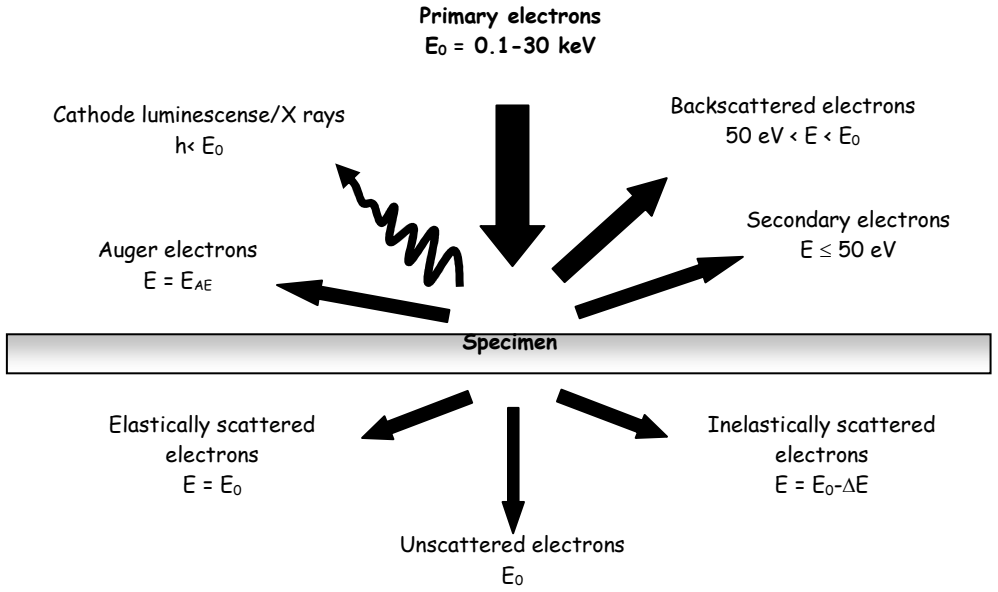

Figure 2. 21. Signals generated by an electron beam (primary electrons) hitting the surface of a thin sample. E_0: energy of beam electrons, E: energy of signal electrons, E_{AE}: energy of Auger electrons, ΔE: energy loss of inelastically scattered electrons, h_v: energy of radiation.(Reprinted from ref 115; fair use; Copyright 2005 Springer Verlag).

When acquiring a SEM image, three different methods are used to detect electrons reflected or emitted by the sample surface. The primary method collects secondary electrons, released by the sample, to build the image. This method uses a scintillation material to convert the electrons to photons and then transforms the photons to an electric signal by means of a photomultiplier tube. The photomultiplier tube signal is used to generate an image of the sample. The second method detects backscattered electrons. The backscattered electrons are converted to electron pairs by a semiconductor material, generating an electrical current. The third method uses the signals from charged particles or energetic photons to convert them into secondary electrons, by using a channel electron multiplier tube. After conversion, these electrons are transformed into electrical signals and may be incorporated as a special characteristics in the SEM image i.e., to build an elemental map of the analyzed sample.[113, 115]

Modern instruments are capable of magnifications of up to 1,500,000 X and resolutions of up to 3 nm. Nevertheless, the strongest attribute of SEM is its great depth of focus due to the small aperture of the condenser lens. However, like other microscopy techniques based on light or electron beams, SEM does not provide information about sample topography and is susceptible to image aberrations, including chromatic, defocus, and spherical aberrations. Another disadvantage of SEM is the fact that the electron beam can cause damage to the specimen, especially for thin specimens of non-conductive materials.

Sample preparation for SEM ranges from a simple task to a complex procedure (e. g., water removal from biological species). In general, it is relatively easy compared to the effort required for other electron microscopy techniques, such as TEM, which requires very thin specimens (30-100 nm) and complex specimen preparation often necessitating special equipment. For SEM, the sample must be conductive to avoid electrostatic charging. If the specimen is non-conductive, it must be coated with a thin layer of a conductive material (e. g., gold or chromium) to ground the surface and prevent the build-up of electrostatic charge. The most commonly used procedure of metal deposition for SEM analysis involves metal sublimation, which produces layers of 10-20 nm thickness. If the structure of a wet specimen needs to be preserved, the water has to be removed using techniques such as freeze-drying and critical point drying that avoid ice crystal formation, prior to SEM analysis.[115-116]

2. 4. 3. Polarized-light microscopy

Light microscopy is a widely used technique for the visualization of specimen details that can not be seen with the naked eye. Light microscopy can yield images of living organisms as well as information about certain optical properties of a material. One of the most important aspects of a microscope is the illumination of the specimen, which should be uniform across the field of view. A modern light microscope can use light generated by several sources, most commonly from a tungsten-halogen bulb, but also from arc-discharge lamps, light emitting diodes, and lasers.[117] The most common forms of illumination of a specimen to be analyzed in a light microscope are reflected and transmitted light. In a transmitted light microscope, the methods of Nelson and Köhler are the two methods of illumination most commonly used. Both methods provide the uniformly bright and glare-free illumination required for high quality analysis of a specimen by light microscopy. Nelson's method is the oldest procedure and was designed to enhance illumination provided by older sources such as oil lamps or bulbs with a ribbon filament. Köhler illumination was develop after the development of modern light bulbs with coil filaments and became the recommended procedure for illuminating specimens in modern microscopes.[116]

In a light microscope, image contrast is created by differences in light intensity between the image and the adjacent background, relative to the overall background intensity. The differences in light can be originated by light absorption or scattering, reflectance, birefringence, diffraction, fluorescence, brightness, or color variations of the analyzed specimen.[117] Samples that are translucent or transparent to visible light can appear featureless and have poor contrast when analyzed under a light microscope. However, there are several contrast enhancing techniques, such as darkfield microscopy, differential interference contrast, specimen staining methods, Hoffman modulation, phase contrast and polarized-light microscopy (PLM). PLM exploits the optical anisotropy of many specimens with crystalline and ordered structures to increase contrast and reveal greater detail about the structure and composition of such materials.[116-117]

Optically anisotropic materials are birefringent, i.e. they exhibit double refraction. Three different types of birefringence can be distinguished. The first type is intrinsic birefringence,

observed in crystalline structures (uniaxial and biaxial). The second type is textural birefringence, characterized by structures with oriented submicroscopic elongated particles. The third type is flow birefringence, which is observed in materials with flow-oriented substructures.

Modern PLMs generate polarized light through special filters made of thin polymer films, such as Polaroid films, which selectively transmit light that is linearly polarized in a specific direction. Figure 2.22 illustrates this method. The first filter, called the polarizer, eliminates any light waves with vibration planes different from the transmission plane of the polarizer. The second filter (named the analyzer) is normally oriented with its transmission plane perpendicular to that of the polarizer, so the light that passes through the polarizer is absorbed, or extinguished, by the analyzer. This arrangement of filters is commonly named cross polarization, and represents the basis of PLM.

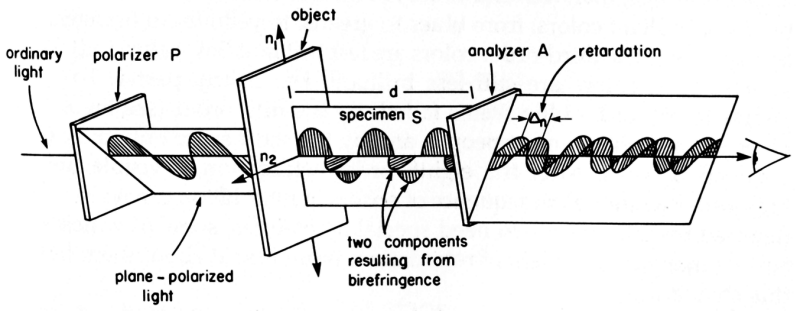

Figure 2. 22. Concept of polarized-light microscopy. (Reprinted from ref 116; fair use; Copyright 1994 Springer).

As is shown in Figure 2.22, when an optically active specimen (e. g. anisotropic materials, certain chemical derivatives, cholesteric materials, among others) is placed between the two filters, a rotation or phase retardation of the plane of polarized light occurs. This effect is detected by the analyzer providing image with a good contrast for those optically active materials, which normally appears transparent under non-polarized light. The resulting wave retardation caused by the interference phenomena of anisotropic materials placed between cross

polarizers, can be estimated by using the Michel-Lévy scale of birefringence (Figure 2.23). Such chart is a Newton series of color sequences where the interference color and retardation of the light (in nm) passing through the analyzer are graphically plotted. The chart is divided into six orders of magnitude, with each order ending in red (about every 565 nm). The contrast in PLM is the result of the combination of a dark background and the first-order gray or high-order white, or colors resulting from the light interference phenomena.[116]

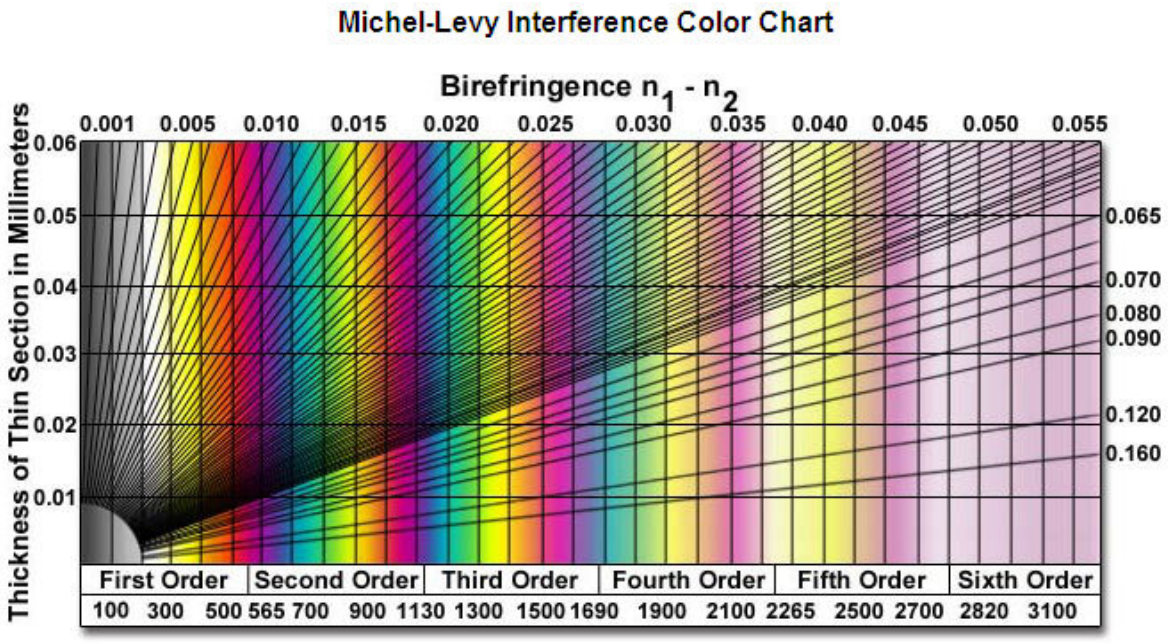

Figure 2. 23. Michel-Lévy scale of birefringence. (Reprinted from ref 118; fair use; Copyright 2010 Olympus America Inc).

Birefringent materials cause a split of the incident light into two perpendicular rays, one vibrating parallel to the axis of anisotropy (extraordinary ray), and the other perpendicular to this axis (ordinary ray). The two emerging light components can interfere positively (the crest of the two wavelengths coincide in the same point), creating a wavelength with a larger amplitude, or negatively (the crest of both wavelengths coincide in different points) resulting in a wavelength with a reduced or nullified amplitude. As a result of the interference phenomena, polarization colors and specific patterns can be seen. Such color and patterns depend on the nature of the

anisotropic material. Uniaxial and biaxial crystals, when analyzed under PLM, show different interference patterns. Figure 2.24 illustrates one common pattern, known as the "Maltese cross", characteristic of uniaxial crystals, but also observed in droplets of nematic liquid crystals. This pattern consists of two intersecting black bars, known as isogyres.[117, 119]

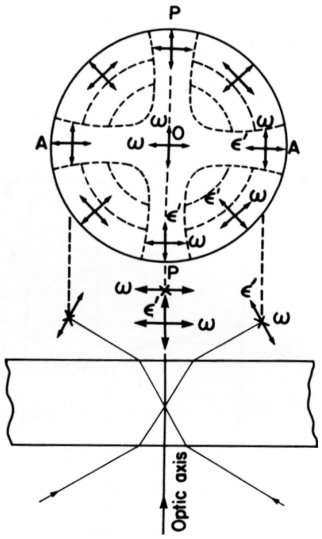

Figure 2. 24. Diagram of an interference pattern found in sample analysis by PLM. (Adapted from ref 116; fair use; Copyright 1994 Springer).

In addition to birefringence, other material characteristics, such as pleochroism, crystal textures, intergrowths, and polymorphic phases, can be studied by PLM. These properties are widely analyzed in geosciences, material science, and chemistry. PLM is a quick and cost effective analysis tool. However, compared to SEM, TEM, or AFM, it is limited by its low resolution and by the inability to provide topographic information for the analyzed specimens.[120]

2. 4. 4. Contact angle goniometry

The surface properties of solids and liquids are important characteristics that influence several phenomena which take place at interfaces between different phases. Whereas the surface tension

of liquids can be easily measured using several methods, evaluation of the surface energy of a solid is a more difficult task. In addition to the forces from the surrounding atoms, the immobile atoms of solid surfaces, relative to those of liquid surfaces, may experience mechanical stresses. In contrast to surface tension measurements, determination of the surface energy of solids requires the use of indirect methods, such as contact angle goniometry, the Wilhelmy plate method, or dynamic contact angle methods, among others.[120-121]

Contact angle goniometry is a widely used technique for determining the contact angle of a liquid drop placed on a solid surface. The contact angle is the angle formed between the surface of the solid and the tangent to the drop surface at the point of contact. The most commonly used technique for measuring a contact angle is the sessile drop method (Figure 2.25-a). Another, less frequently used, method is the pendant drop method (Figure 2.25-b). The pendant drop method is based on the profile of a drop of liquid hanging from the tip of a volumetric syringe. This method is a widely used procedure for the measurement of the surface tension of liquids. For surface energy characterizations of solids, the sessile drop method is used. The sessile drop method uses a micro volumetric syringe to deposit a small drop of liquid onto a solid surface. Both techniques use an eyepiece or video camera to analyze the drop profile. The shape of the droplet is determined by the balance between the forces of surface tension and gravity.

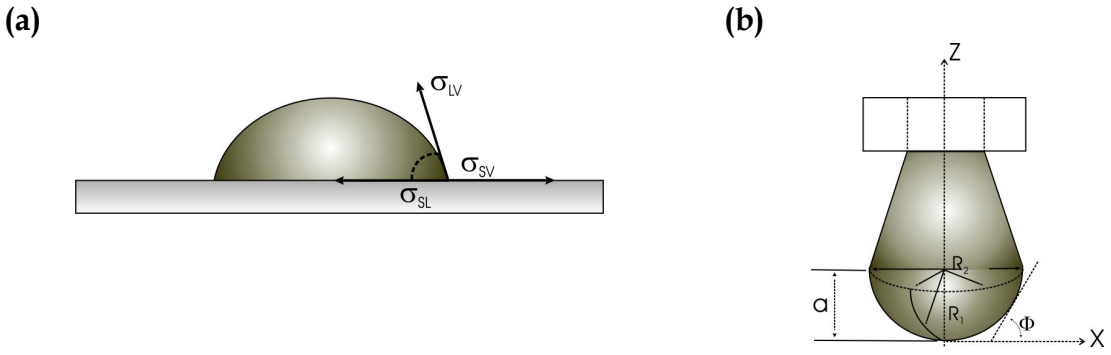

Figure 2. 25. Typical drop profiles used during contact angle analysis. (a) sessile drop, (b) pendant drop. (Adapted from ref 121; fair use; Copyright 2002 Springer Verlag and ref 122; fair use; Copyright 2007 Elsevier Ltd).

As was mentioned before, the sessile drop method is commonly used to obtain contact angle values. However, this method has some assumptions that must be considered in order to obtain accurate results. The sessile drop method assumes a flat and chemically homogenous surface, and the surface does not have appreciable property changes (e. g. swelling, chemical reactions, bending) due to interactions with the liquid or gas used in the determination of the contact angle. Some authors, such as Neumann et al.[123] and Prokop et al.[124] have reported more accurate and sophisticated techniques for the measurement of contact angles, such as the axisymmetric drop shape analysis (ADSA). ADSA is utilized for the measurement of contact angles of pendant and sessile drops, as well as for interfacial tension evaluations. This technique relies on the analysis of the drop's profile, obtained by capturing and processing a digital image of the droplet, along with further computer analysis (using non-linear regression) to find the best fit to theoretical Young-Laplacian curves, and finally calculate the desired values of contact angle, surface energy, or interfacial tension.[125]

Contact angle is an important parameter in several thermodynamic models for the determination of the surface energy of solids. These models were designed to interpret the origins of surface energy from a molecular point of view. Among these models are the Zisman[126] critical surface tension model, the van Oss-Chaudhury-Good[127] model, the Chang-Chen[128] model, and the Comyn[129] model.

One of the pioneering works in thermodynamics of wetting and adhesion of solids was published in 1964 by Zisman et al. This model was developed using the Young expression (equation 2.4) for the relationship between surface free energies of a liquid and a solid, and the contact angle between them, but also an equation for the determination of the work of adhesion (W_A) between two components. These two equations are:

$$\gamma_{SV} - \gamma_{SL} = \gamma_{LV} \cos(\theta) \qquad [2.4]$$

$$W_A = \gamma_A + \gamma_B - \gamma_{AB} \qquad [2.5]$$

In equation 2.4 the subscripts *LV*, *SL* and *SV* refer to liquid-vapor, solid-liquid and liquid-vapor interfaces respectively. Zisman termed the subscripts *S* as S^o to indicate the solid interface

without vapor or liquid, and V as V^o to indicate vapor saturation i. e., L-V^o indicates liquid-saturated vapor interface.

In the Zisman approach, equations 2.4 and 2.5 were combined to obtain the following expression:

$$W_A = \left(\gamma_{S^o} - \gamma_{SV^o}\right) + \gamma_{LV^o}\cos(\theta) \qquad [2.6]$$

Here the term $\left(\gamma_{S^o} - \gamma_{SV^0}\right)$ was defined as:

$$\left(\gamma_{S^o} - \gamma_{SV^o}\right) = RT\int_0^{P^o} \Gamma d\ln p = \pi_e \qquad [2.7]$$

Where π_e = the film pressure, Γ = surface excess of the liquid vapor and P^o = vapor pressure of saturation for the liquid phase. In this model, the vapor was assumed to be ideal and also that for low surface free energy solids, π_e approximates to zero. Empirically Zisman and co-workers found that, when plotted the cosine of the contact angle was plotted versus the free energy of the liquid, the relationship was almost linear. They assumed it as a linear behavior and proposed the following equation:

$$\cos(\theta) = 1 + \beta\left(\gamma_c - \gamma_{LV^o}\right) \qquad [2.8]$$

In equation 2.8, γ_c is referred to as the Zisman critical surface tension and its magnitude can be calculated by extrapolating the data to the intersection of cos(θ)=1, at this point $\gamma_c = \gamma_{LV}$ - γ_c was assumed to be equal to the surface energy of the solid according to equation 2.4, or $\left(\gamma_{S^o} - \gamma_{LV^o}\right) \approx \left(\gamma_{SV^o} - \gamma_{LV^o}\right) = \gamma_c$. For many practical applications the Zisman critical surface tension is considered as the solid surface energy, however, strictly speaking this value is not the solid surface energy. Also the Zisman approach does not provide any information between the relationship of the surface chemistry of the analyzed specimen and the measured contact angle. [126]

In the late 80's, van Oss, Chaudhury and Good proposed a more refined thermodynamic approach for the determination of the free energy of solids incorporating the effect of intermolecular forces between molecules to their model. The authors stated that the surface free energy can be calculated as the sum of two components, a polar component defined in terms of Lewis acid-base interactions (γ^{AB}), and an apolar component defined in terms of Lifshitz-van der Waals interactions (γ^{LW}). The van Oss-Chaudhury-Good model defined the Young equation as:

$$(1+\cos\theta)\gamma_L = W_A^{LW} + W_A^{AB} \qquad [2.9]$$

Where the work of adhesion due to the Lifshitz-van de Waals interactions was defined as:

$$W_A^{LW} = 2\sqrt{\left(\gamma_S^{LW}\gamma_L^{LW}\right)} \qquad [2.10]$$

While the Lewis acid-base parameter was defined as:

$$W_A^{AB} = 2\sqrt{\left(\gamma_s^+\gamma_L^-\right)} + 2\sqrt{\left(\gamma_S^-\gamma_L^+\right)} \qquad [2.11]$$

In equations 2.10 and 2.11 the subscripts *S* and *L* refer to the solid and liquid respectively, and the superscripts + and – in equation 2.11 refer to the electron-acceptor and electron-donor parameters of the surface tension. Van Oss et al. incorporated the terms defined in equations 2.10 and 2.11 into equation 2.9 to obtain:

$$(1+\cos\theta)\gamma_L = 2\left(\sqrt{\gamma_S^{LW}\cdot\gamma_L^{LW}} + \sqrt{\gamma_S^+\cdot\gamma_L^-} + \sqrt{\gamma_S^-\cdot\gamma_L^+}\right) \qquad [2.12]$$

Equation 2.12 contains 3 unknowns γ_S^{LW}, γ_S^+ and γ_S^-, thus requires the evaluation of the contact angle using at least three liquids with their polar and apolar components well defined.[127] The van Oss-Chaudhury-Good model is a very useful model for the determination of the free energy of solids, however, it is susceptible to produce artificial errors due to several factors. Gardner et al.[130] warned that this model may give different results if different calculation methods are used to solve the simultaneous equations. Dalal[131] reported that the calculated values for the van Oss-Chaudhury-Good model depended upon the liquids used, and he suggested that

many liquids should be used to minimize this effect. Other authors[121, 134] warned about the tendency of the van Oss-Chaudhury-Good model to produce exaggerated surface basicity results.

Another alternative for the determination of the surface free energy of solids was published by Rabel,[132] Kaelble,[133] Owens and Wendt[134]. Similar to the van Oss-Chaudhury-Good model, The Owens-Wendt-Rabel-Kaelble approach suggested the evaluation of contact angle using at least 3 well characterized liquids, however, in this model it was argued that for both, solid and liquid phases, the surface energy was the sum of a polar (γ^P) and non-polar or dispersive (γ^D) components:

$$\gamma_{LV} = \gamma_{\mathrm{L}}^{\mathrm{P}} + \gamma_L^D \qquad [2.13]$$

$$\gamma_{SV} = \gamma_S^P + \gamma_S^D \qquad [2.14]$$

The Owens-Wendt-Rabel-Kaelble approach used Fowkes equation to calculate the interfacial energy between the solid and liquid phase (γ_{SL}) obtaining the following expression:

$$\gamma_{SL} = \gamma_{SV} + \gamma_{SL} - 2\sqrt{\left(\gamma_S^D \gamma_L^D\right)} - 2\sqrt{\left(\gamma_S^P \gamma_L^P\right)} \qquad [2.15]$$

Then, equation 2.15 was combined with the Young equation to derive the following equation:

$$\frac{\gamma_{LV}\left(1+\cos\theta\right)}{2\sqrt{\gamma_L^D}} = \sqrt{\gamma_S^D} + \sqrt{\frac{\gamma_S^P \gamma_L^P}{\gamma_L^D}} \qquad [2.16]$$

According to the Owens-Wendt-Rabel-Kaelble approach, the later equation is a linear relationship when $\gamma_{LV}\left(1+\cos\theta\right) \Big/ 2\sqrt{\gamma_{\mathrm{L}}^{\mathrm{D}}}$ is plotted against $\sqrt{\gamma_L^P \Big/ \gamma_L^D}$, and the polar and dispersive components of the solid surface energy can be calculated from the slope and intercept respectively. Finally, the surface free energy of the solid can be calculated as the sum of these two components, as is expressed in equation 2.14.[129]

2. 5. Bibliography

1. Payen, A. Mémoire sur la composition du tissu propre des plantes et du ligneux. *Comtes Rendus Hebdomadaires des Seances de L'Académie des Sciences* **1838,** 7, 1052-1125.
2. Payen, A. Mémoire sur les applications théoriques et pratiques des propriétés du tissu élémentaire des végétaux. *Comtes Rendus Hebdomadaires des Seances de L'Académie des Sciences* **1839,** 8, 59-61.
3. Kamide, K. Cellulose and cellulose derivatives. Molecular characterization and it's applications. 1st ed.; Elsevier Science: 2005.
4. Klemm, D.; Heublein, B.; Fink, H.-P.; Bohn, A. Cellulose: Fascinating Biopolymer and Sustainable Raw Material. *Angewandte Chemie International Edition* **2005,** 44, 3358 - 3393.
5. Krässig, H. A. Cellulose: Structure, accessibility and reactivity 1st ed.; Gordon and Breach Science P.: 1993; Vol. Polymer monographs Vol. 11.
6. Montananari, S.; Roumani, M.; Heux, L.; Vignon, M. R. Topochemistry of Carboxylated Cellulose Nanocrystals Resulting from TEMPO-Mediated Oxidation. *Macromolecules* **2005,** 38, 1665-1671.
7. Kobayashi, S.; Uyama, H.; Kimura, S. Enzymatic polymerization. *Chemical Reviews* **2001,** 101, 3793-3818.
8. Putra, A.; Kakugo, A.; Furukawa, H.; Gong, J. P.; Osada, Y. Tubular bacterial cellulose gel with oriented fibrils on the curved surface. *Polymer* **2008,** 49, 1885-1891.
9. Charrier, B.; Coelho, S. M.; Le Bail, A.; Tonon, T.; Michel, G.; Potin, P.; Kloareg, B.; Boyen, C.; Peters, A. F.; Cock, J. M. Development and physiology of the brown alga Ectocarpus siliculosus: two centuries of research. *New Phytologist* **2008,** 177, 319-332.
10. Kobayashi, S.; Kashiwa, K.; Shimada, J.; Kawasaki, T.; Shoda, S. Enzymatic polymerization - The 1st invitro synthesis of cellulose via nonbiosynthetic path catalyzed by cellulase. *Makromolekulare Chemie-Macromolecular Symposia* **1992,** 54-5, 509-518.
11. Gardner, D. J.; Oporto, G. S.; Mills, R.; Samir, M. Adhesion and surface issues in cellulose and nanocellulose. *Journal of Adhesion Science and Technology* **2008,** 22, 545-567.

12. Haigler, C. H.; Weimer, P. J. Biosynthesis and biodegradation of cellulose CRC: 1990.
13. Klemm, D.; Heublein, B.; Fink, H. P.; Bohn, A. Cellulose: Fascinating biopolymer and sustainable raw material. *Angewandte Chemie-International Edition* **2005,** 44, 3358-3393.
14. Hengstenberg, J.; Mark, H. *Zeitschrift für Kristallographie* **1928,** 69, 271.
15. Mark, H. Intermicellar Hole and Tube System in Fiber Structure. *Journal of Physical Chemistry* **1940,** 44, 764-788.
16. Meyer, K. H.; van der Wyk, A. Propriétés de polymères en solution VIII. Formation de micelles dans les solutions de substances à molécules caténiformes *Helvetica Chimica Acta* **1937,** 20, 1321-1330.
17. Lima, M. M. D.; Borsali, R. Rodlike cellulose microcrystals: structure, properties, and applications. *Macromol. Rapid Commun.* **2004,** 25, 771–787.
18. Woodcock, C.; Sarko, A. Packing analysis of carbohydrates and polysaccharides .11. Molecular and crystal-structure of native ramie cellulose. *Macromolecules* **1980,** 13, 1183-1187.
19. Atalla, R. H.; Ellis, J. D.; Schroeder, L. R. Some effects of elevated-temperatures on the structure of cellulose and its transformation. *Journal of Wood Chemistry and Technology* **1984,** 4, 465-482.
20. Nishiyama, Y.; Sugiyama, J.; Chanzy, H.; Langan, P. Crystal structure and hydrogen bonding system in cellulose 1(alpha), from synchrotron X-ray and neutron fiber diffraction. *Journal of the American Chemical Society* **2003,** 125, 14300-14306.
21. Nishiyama, Y.; Langan, P.; Chanzy, H. Crystal structure and hydrogen-bonding system in cellulose 1 beta from synchrotron X-ray and neutron fiber diffraction. *Journal of the American Chemical Society* **2002,** 124, 9074-9082.
22. Langan, P.; Sukumar, N.; Nishiyama, Y.; Chanzy, H. Synchrotron X-ray structures of cellulose I-beta and regenerated cellulose II at ambient temperature and 100 K. *Cellulose* **2005,** 12, 551-562.
23. Nishiyama, Y.; Johnson, G. P.; French, A. D.; Forsyth, V. T.; Langan, P. Neutron Crystallography, Molecular Dynamics, and Quantum Mechanics Studies of the Nature of Hydrogen Bonding in Cellulose I-beta. *Biomacromolecules* **2008,** 9, 3133-3140.

24. Samir, M.; Alloin, F.; Dufresne, A. Review of recent research into cellulosic whiskers, their properties and their application in nanocomposite field. *Biomacromolecules* **2005,** 6, 612-626.

25. Zugenmaier, P. Conformation and packing of various crystalline cellulose fibers. *Progress in Polymer Science* **2001,** 26, 1341-1417.

26. Zugenmaier, P. Morphology. In: Crystalline Cellulose and Derivatives; Springer Berlin Heidelberg: Berlin, 2008; Chapter 7, pp 207-221.

27. Wada, M.; Chanzy, H.; Nishiyama, Y.; Langan, P. Cellulose IIII crystal structure and hydrogen bonding by synchrotron X-ray and neutron fiber diffraction. *Macromolecules* **2004,** 37, 8548-8555.

28. Wada, M.; Heux, L.; Sugiyama, J. Polymorphism of cellulose I family: Reinvestigation of cellulose IV. *Biomacromolecules* **2004,** 5, 1385-1391.

29. Girisuta, B.; Janssen, L.; Heeres, H. J. Kinetic study on the acid-catalyzed hydrolysis of cellulose to levulinic acid. *Industrial & Engineering Chemistry Research* **2007,** 46, 1696-1708.

30. Xiang, Q.; Kim, J. S.; Lee, Y. Y. A comprehensive kinetic model for dilute-acid hydrolysis of cellulose. *Applied Biochemistry and Biotechnology* **2003,** 105, 337-352.

31. Saeman, J. F. Kinetics of Wood Sacharification: hydrolysis of Cellulose and Decomposition of Sugars in Dilute Acid at High Temperature. *Industrial & Engineering Chemistry Research* **1945,** 37, 42-52.

32. Malester, I. A.; Green, M.; Shelef, G. Kinetics of dilute acid-hydrolysis of cellulose originating from municipal solid-wastes. *Industrial & Engineering Chemistry Research* **1992,** 31, 1998-2003.

33. Nickerson, R. F.; Harble, J. A. Cellulose intercrystalline structure. Study by hydrolytic methods. *Industrial & Engineering Chemistry Research* **1947,** 39, 1507–1512.

34. Battista, O. A. Hydrolysis and crystallization of cellulose. *Industrial & Engineering Chemistry Research* **1950,** 42, 502–507.

35. Millet, M. A.; Moore, W. E.; Saeman, J. F. Preparation and properties of hydrocellulose. *Industrial & Engineering Chemistry Research* **1954,** 46, 1493-1497.

36. Battista, O. A.; Smith, P. A. Microcrystalline cellulose: The oldest polymer finds new industrial uses. *Industrial and Engineering Chemistry*. **1962,** 54, 20-29.

37. Browning, B. L. Methods of Wood Chemistry, Vol. II Interscience Publishers,. Interscience: New york, 1967; Vol. II.

38. Xiang, Q.; Lee, Y. Y.; Pettersson, P. O.; Torget, R. Heterogeneous aspects of acid hydrolysis of alpha-cellulose. *Applied Biochemistry and Biotechnology* **2003,** 105, 505-514.

39. Bondenson, D.; Mathew, A.; Oksman, K. Optimisation of the isolation of nanocrystals from microcrystalline cellulose by acid hydrolysis. *Cellulose* **2006,** 13, 171-180.

40. Bondeson, D.; Kvien, I.; Oksman, K. Strategies for preparation of cellulose whiskers from microcrystalline cellulose as reinforcement in nanocomposites. *Cellulose Nanocomposites: Processing, Characterization, and Properties* **2006,** 938, 10-25.

41. Camacho, F.; Gonzalez Tello, P.; Jurado, E.; Robles, A. Microcrystalline-cellulose hydrolysis with concentrated sulphuric acid. *Journal of Chemical Technology and Biotechnology* **1996,** 67, 350-356.

42. Fleming, K.; Gray, D. G.; Matthews, S. Cellulose crystallites. *Chemistry-a European Journal* **2001,** 7, 1831-1835.

43. Rånby, B. G.; Ribi, E. Uber Den Feinbau Der Zellulose. *Experientia* **1950,** 6, 12-14.

44. Battista, O. A.; Smith, P. A. Level-off D.P. cellulose products. US Patent 2,978,446. 1961.

45. Araki, J.; Wada, M.; Kuga, S.; Okano, T. Flow properties of microcrystalline cellulose suspension prepared by acid treatment of native cellulose. *Colloids Surfaces A: Physicochem. Eng. Aspects* **1998,** 142 75–82.

46. Araki, J.; Wada, M.; Kuga, S.; Okana, T. Influence of surface charge on viscosity behavior of cellulose microcrystal suspension. *Journal of Wood Science* **1999,** 45, 258-261.

47. Dong, X. M.; Gray, D. G. Effect of Counterions on Ordered Phase Formation in Suspensions of Charged Rodlike Cellulose Crystallites. *Langmuir* **1997,** 13, 2404-2409.

48. Beck-Candanedo, S.; Roman, M.; Gray, D. G. Effect of reaction conditions on the properties and behavior of wood cellulose nanocrystal suspensions. *Biomacromolecules* **2005,** 6, 1048-1054.

49. Elazzouzi-Hafraoui, S.; Nishiyama, Y.; Putaux, J. L.; Heux, L.; Dubreuil, F.; Rochas, C. The shape and size distribution of crystalline nanoparticles prepared by acid hydrolysis of native cellulose. *Biomacromolecules* **2008,** 9, 57-65.

50. Heux, L.; Dinand, E.; Vignon, M. R. Structural aspects in ultrathin cellulose microfibrils followed by C-13 CP-MAS NMR. *Carbohydrate Polymers* **1999,** 40, 115-124.

51. Terech, P.; Chazeau, L.; Cavaille, J. Y. A small-angle scattering study of cellulose whiskers in aqueous suspensions. *Macromolecules* **1999,** 32, 1872-1875.

52. Lima, A. M. D.; Wong, J. T.; Paillet, M.; Borsali, R.; Pecora, R. Translational and rotational dynamics of rodlike cellulose whiskers. *Langmuir* **2003,** 19, 24-29.

53. Broersma, S. Viscous force and torque constants for a cylinder. *Journal of Chemical Physics* **1981,** 74, 6989.

54. Broersma, S. Rotational Diffusion Constant of a Cylindrical Particle *Journal of Chemical Physics* **1960,** 32, 1626-1631.

55. Broersma, S. Viscous Force Constant for a Closed Cylinder *Journal of Chemical Physics* **1960,** 32, 1632-1635.

56. Baker, A. A.; Helbert, W.; Sugiyama, J.; Miles, M. J. High-resolution atomic force microscopy of native Valonia cellulose I microcrystals. *Journal of Structural Biology* **1997,** 119, 129-138.

57. Baker, A. A.; Helbert, W.; Sugiyama, J.; Miles, M. J. High resolution atomic force microscopy of cellulose microcrystals. *Abstracts of Papers of the American Chemical Society* **1998,** 216, U344-U344.

58. Baker, A. A.; Helbert, W.; Sugiyama, J.; Miles, M. J. New insight into cellulose structure by atomic force microscopy shows the I-alpha crystal phase at near-atomic resolution. *Biophysical Journal* **2000,** 79, 1139-1145.

59. Kvien, I.; Tanem, B. S.; Oksman, K. Characterization of cellulose whiskers and their nanocomposites by atomic force and electron microscopy. *Biomacromolecules* **2005,** 6, 3160-3165.

60. Gray, D. G. Chiral nematic ordering of polysaccharides. *Carbohydrate Polymers* **1994,** 25, 277-284.

61. de Vries, H. Rotatory power and other optical properties of certain liquid crystals. *Acta Crystallographica* **1951,** 4, 219-226.

62. Edgar, C. D.; Gray, D. G. Induced circular dichroism of chiral nematic cellulose films. *Cellulose* **2001,** 8, 5–12.

63. Orts, W. J.; Godbout, L.; Marchessault, R. H.; Revol, J. F. Shear-induced alignment of liquid-cystalline suspensions of cellulose microfibrils. In: Flow-Induced Structure in Polymers; Acs Symposium Series; Amer Chemical Soc: Washington, 1995; Vol. 597, pp 335-348.

64. Bercea, M.; Navard, P. Shear dynamics of aqueous suspensions of cellulose whiskers. *Macromolecules* **2000,** 33, 6011-6016.

65. Keeling, M. R. Ink Jet Printing. *Physics in Technology* **1981,** 12, 196-203.

66. Le, H. P. Progress and trends in ink-jet printing technology. *Journal of Imaging Science and Technology* **1998,** 42, 49-62.

67. Rayleigh, F. R. S. On the Instability of Jets. *Proceedings of the London Mathematical Society* **1878,** 10, 4-13.

68. Sweet, R. G. High frequency recording with electrostatically deflected ink-jets.*,Rev. Sci. Instrum.* **1965,** 36, 131.

69. Hertz, C. H.; Mansson, A. Electronic Ink Jet Device. *Photographic Science and Engineering* **1974,** 18, 664-664.

70. Kyser, E. L.; Sears, S. B. Method and apparatus for recording with writing fluids and drop projection means therefore. 1976.

71. Zoltan, S. L. C. C. Pulse droplet ejection system. 1974.

72. Endo, I.; Sato, y.; Saito, s.; Nakagiri, t.; Ohno, s. C. Liquid jet recording process and apparatus there for. 1979.

73. Vaught, J. L.; Cloutier, F. L.; Donald, D. K.; Meyer, J. D.; Tacklind, C. A.; Taub, H. H. H.-P. Thermal ink-jet printer. 1984.

74. Agui, T.; Nakajima, M. Drop formation characteristics of electrostatic ink jet using water-based ink. *IEEE Transactions on Electron Devices* **1977,** 24, 262-266.

75. Fillmore, G. L.; Buehner, W. L.; West, D. L. Drop charging and deflection in an electrostatic ink jet printer. *Ibm Journal of Research and Development* **1977,** 21, 37-47.

76. Huang, D.; Kim, E. S. Micromachined acoustic-wave liquid ejector. *Journal of Microelectromechanical Systems* **2001,** 10, 442-449.

77. Tam, A. C.; Gill, W. D. Photo-acoustic ejection from a nozzle (pen) for drop-on-demand ink jet printing. *Applied Optics* **1982,** 21, 1891-1892.

78. Sirringhaus, H.; Shimoda, T. Inkjet printing of functional materials. *Mrs Bulletin* **2003,** 28, 802-803.

79. Sweet, R. G. "High-Frequency Oscillography with Electrostatically Deflected Ink Jets," Stanford Electronics Laboratories Technical Report No. 1722-1, Stanford University, CA; 1964.

80. Macfarlane, D. L.; Narayan, V.; Tatum, J. A.; Cox, W. R.; Chen, T.; Hayes, D. J. Microjet fabrication of microlens arrays. *IEEE Photonics Technology Letters* **1994,** 6, 1112-1114.

81. Biehl, S.; Danzebrink, R.; Oliveira, P.; Aegerter, M. A. Refractive microlens fabrication by ink-jet process. *Journal of Sol-Gel Science and Technology* **1998,** 13, 177-182.

82. Pericet-Camara, R.; Best, A.; Nett, S. K.; Gutmann, J. S.; Bonaccurso, E. Arrays of microlenses with variable focal lengths fabricated by restructuring polymer surfaces with an ink-jet device. *Optics Express* **2007,** 15, 9877-9882.

83. Lopez, F. V.; Diez, A.; Odriozola, A. Inkjet printing of conductive and resistive coatings. *International Polymer Processing* **2007,** 22, 27-32.

84. Nur, H. M.; Song, J. H.; Evans, J. R. G.; Edirisinghe, M. J. Ink-jet printing of gold conductive tracks. *Journal of Materials Science-Materials in Electronics* **2002,** 13, 213-219.

85. Karwa, A.; Xia, Y.; Clark, D. M.; Smith, T. W.; Kahn, B. E. Printable electronics: Patterning of conductive materials for novel applications. *Semiconductor Materials for Sensing* **2005,** 828, 293-297.

86. Mei, J. F.; Lovell, M. R.; Mickle, M. H. Formulation and processing of novel conductive solution inks in continuous inkjet printing of 3-D electric circuits. *IEEE Transactions on Electronics Packaging Manufacturing* **2005,** 28, 265-273.

87. Ramsey, B. J.; Evans, P. S. A.; Harrison, D. Conductive lithographic films. Proceedings of the 1997 IEEE International Symposium on Electronics and the Environment - Isee-1997 **1997**, 252-256.

88. Tekin, E.; Smith, P. J.; Schubert, U. S. Inkjet printing as a deposition and patterning tool for polymers and inorganic particles. *Soft Matter* **2008,** 4, 703-713.

89. Yoshioka, Y.; Jabbour, G. E. Desktop inkjet printer as a tool to print conducting polymers. *Synthetic Metals* **2006,** 156, 779-783.

90. Calvert, P. Inkjet printing for materials and devices. *Chemistry of Materials* **2001,** 13, 3299-3305.

91. Pan, P. C.; Chen, M.; Koo, H. S.; Wu, F. M.; Chang, S. J. Organic color films prepared by inkjet printing method and its properties. *Ieice Transactions on Electronics* **2006,** E89C, 1727-1731.

92. Zaugg, F. G.; Wagner, P. Drop-on-demand printing of protein biochip arrays. *Mrs Bulletin* **2003,** 28, 837-842.

93. Dong, H. M.; Carr, W. W. An experimental study of drop-on-demand drop formation. *Physics of fluids* **2006,** 18, 1-16.

94. Fisher, W.; Zhang, M. J. A biochip microarray fabrication system using inkjet technology. *IEEE Transactions on Automation Science and Engineering* **2007,** 4, 488-500.

95. Allain, L. R.; Askari, M.; Stokes, D. L.; Vo-Dinh, T. Microarray sampling-platform fabrication using bubble-jet technology for a biochip system. *Fresenius Journal of Analytical Chemistry* **2001,** 371, 146-150.

96. Cho, H. J.; Parameswaran, M.; Yu, H. Z. Fabrication of microsensors using unmodified office in inkjet printers. *Sensors and Actuators B-Chemical* **2007,** 123, 749-756.

97. http://www.lexmark.be/uncomplicate/sequentialem/home/0, 247172_2729_9409802_en,00.html

98. Lindemann, T.; Ashauer, H.; Yu, Y.; Sassano, D. S.; Zengerle, R.; Koltay, P. One inch thermal bubble jet printhead with laser structured integrated polyimide nozzle plate. *Journal of Microelectromechanical Systems* **2007,** 16, 420-428.

99. http://www.techexchange.com/thelibrary/tchnlgy.pdf

100. Chen, P. H.; Chen, W. C.; Ding, P. P.; Chang, S. H. Droplet formation of a thermal sideshooter inkjet printhead. *International Journal of Heat and Fluid Flow* **1998,** 19, 382-390.

101. Krause, P.; Obermeier, E.; Wehl, W. A micromachined single-chip inkjet printhead. *Sensors and Actuators a-Physical* **1996,** 53, 405-409.

102. Zhang, Z. G.; Grishini, A. Characterization of piezoelectric shear mode inkjet actuator. *Integrated Ferroelectrics* **2005,** 69, 401-+.

103. Brunahl, J.; Grishin, A. M. Piezoelectric shear mode drop-on-demand inkjet actuator. *Sensors and Actuators a-Physical* **2002,** 101, 371-382.

104. Beulen, B.; de Jong, J.; Reinten, H.; van den Berg, M.; Wijshoff, H.; van Dongen, R. Flows on the nozzle plate of an inkjet printhead. *Experiments in Fluids* **2007,** 42, 217-224.

105. Binnig, G.; Quate, C. F.; Gerber, C. Atomic Force Microscope. *Physical Review Letters* **1986,** 56, 930-933.

106. Jalili, N.; Laxminarayana, K. A review of atomic force microscopy imaging systems: application to molecular metrology and biological sciences. *Mechatronics* **2004,** 14, 907-945.

107. Zavala, G. Atomic force microscopy, a tool for characterization, synthesis and chemical processes. *Colloid and Polymer Science* **2008,** 286, 85-95.

108. Sebastian, A.; Gannepalli, A.; Salapaka, M. V. A review of the systems approach to the analysis of dynamic-mode atomic force microscopy. *IEEE Transactions on Control Systems Technology* **2007,** 15, 952-959.

109. Abramovitch, D. Y.; Andersson, S. B.; Pao, L. Y.; Georg, S. A Tutorial on the mechanisms, dynamics, and control of Atomic Force Microscopes. Proceedings of the 2007 American Control Conference, New York, 2007; pp 3488-3502.

110. http://www.veeco.com/pdfs/appnotes/AN48r2_SPM_AFM_278.pdf

111. http://www.afmuniversity.org/pdf/Chapter_6_.pdf

112. http://www.pacificnanotech.com/files/pdf_15_1076152090_0.pdf

113. Hawkes, P. W.; Spence, J. C. H. Science of microscopy. 2° ed.; Springer: New York, 2007; Vol. 1, pp. 140.

114. Egerton, R. F. Physical Principles of Electron Microscopy. Springer: New york, 2005; pp. 125-140.

115. Egerton, R. F. The scanning electron microscope. In: Physical principles of electron microscopy : an introduction to TEM, SEM, and AEM; Four ed.; Springer: New york, 2005; Chapter 5, pp 124-153.

116. Rochow, T.; Tucker, P. A. Introduction to microscopy by means of light, electrons, X rays, or acoustics. Second ed.; Plenum Press: New York, 1994.
117. http://www.olympusmicro.com/primer/index.html
118. http://www.olympusmicro.com/primer/java/polarizedlight/michellevylarge/index.html.
119. Ondriscrawford, R.; Boyko, E. P.; Wagner, B. G.; Erdmann, J. H.; Zumer, S.; Doane, J. W. Microscope Textures of Nematic Droplets in Polymer Dispersed Liquid-Crystals. *Journal of Applied Physics* **1991,** 69, 6380-6386.
120. Kile, D. Polarized light microscopy in geoscience education: Relevant or obsolete? *Elements* **2006,** 2, 197-198.
121. Morita, A. T.; Carastan, D. J.; Demarquette, N. R. Influence of drop volume on surface tension evaluated using the pendant drop method. *Colloid and Polymer Science* **2002,** 280, 857-864.
122. Schwarz, B.; Elsenmenger-Sittner, C.; Steiner, H. Construction of a high-temperature sessile drop device. *Vacuum* **2007,** 82, 186-188.
123. Neumann, A. W.; del Rio, O. I.; Kwok, D. Y.; Wu, R.; Alvarez, J. M. Contact angle measurements by axisymmetric drop shape analysis and an automated polynomial fit program. *Colloids and Surfaces a-Physicochemical and Engineering Aspects* **1998,** 143, 197-210.
124. Prokop, R. M.; Jyoti, A.; Eslamian, M.; Garg, A.; Mihaila, M.; del Rio, O. I.; Susnar, S. S.; Policova, Z.; Neumann, A. W. A study of captive bubbles with axisymmetric drop shape analysis. *Colloids and Surfaces a-Physicochemical and Engineering Aspects* **1998,** 131, 231-247.
125. Etzler, F. M. Characterization of free energies and surface chemistry of solids. In: Contact angle, wettability and adhesion. Volume 3; Mittal, K. L., Ed.; Utrecht: Boston, 2003; Vol. 3, pp 219-264.
126. Zisman, W. A. Relation of the equilibrium contact angle to liquid and solid constitution. *Contact Angle, Wettability and Adhesion, American Chemical Society* **1964**, 1-51.
127. VanOss, C. J.; Chaudhury, M. K.; Good, R. J. Interfacial Lifshitz-VanderWaals and polar interactions in macroscopic systems. *Chemical Reviews* **1988,** 88, 927-941.
128. Chen, F.; Chang, W. V. Applicability study of a new acid-base interaction-Model in polypeptides and polyamides. *Langmuir* **1991,** 7, 2401-2404.

129. Comyn, J. Contact Angles and Adhesive Bonding. *International Journal of Adhesion and Adhesives* **1992,** 12, 145-149.

130. Gardner, D. J.; Shi, S. Q.; Tze, W. T. Acid-base interactions: Relevance to adhesion science and technology. In: Mittal, K. L., Ed.; VSP, Utrecht: 2000; Vol. 2, p 363.

131. Dalal, E. N. Calculation of Solid Surface Tensions. *Langmuir* **1987,** 3, 1009-1015.

132. Rabel, W. Einige Aspekte der Benetzungstheorie und ihre Anwendung auf die Untersuchung und Veränderung der Oberflächeneigenschaften von Polymeren. *Farbe und Lack* **1971,** 77, 997-1006.

133. Kaelble, D. H. Dispersion-Polar Surface Tension Properties of Organic Solids. *Journal of Adhesion* **1970,** 2, 66-81.

134. Owens, D. K.; Wendt, R. C. Estimation of the surface free energy of polymers. *Journal of Applied Polymer Science* **1969,** 13, 1741-1747.

Chapter 3

Estimation of the Tip Broadening Effect in AFM Width Measurements of Cellulose Nanocrystals

Estimation of the Tip Broadening Effect in AFM Width Measurements of Cellulose Nanocrystals

Fernando Navarro and Maren Roman

Macromolecules and Interfaces Institute and Department of Wood Science and Forest Products, 230 Cheatam Hall, Virginia Polytechnic Institute and State University, Blacksburg, Virginia, 24061, United States of America.

3.1. Abstract

Dimensional measurements by atomic force microscopy (AFM) are impeded by tip broadening effects. The term tip broadening refers here to the difference between the apparent and actual width of an object or feature. In the present work, a method is proposed for the estimation of the tip broadening effect in AFM width measurements of cellulose nanocrystals (CNCs). The method is based on the first and second derivatives of the apparent transverse height profiles of the non-spherical nanoparticles. The method is explained for cylindrical and elliptic cylindrical nanoparticles on simulated AFM height profiles and experimentally demonstrated on gold nanorods of known dimensions. Application of the method to CNCs prepared from dissolving-grade softwood pulp by sulfuric acid hydrolysis gave an actual average width of about 11.8 nm and a width-to-height ratio of 2.7. The estimated actual width of the particles was independent of tip radius. The magnitude of tip broadening decreased with decreasing tip radius and was constant within a sample. The accuracy of the method depended on the spacing of the data points in the height profile. The fact that the magnitude of tip broadening was constant within a sample indicated that, once determined from a small number of particles, it could be used to correct the apparent width and length values of all particles within the sample for tip broadening.

Keywords: *cellulose nanocrystals, gold nanorods, width, AFM, tip broadening, height profiles.*

3.2. Introduction

Since its invention in the mid 1980s,[1-2] atomic force microscopy (AFM) has found a large number of applications, including imaging of surfaces,[3-4] molecules,[5-7] and cells,[6-8] measuring of surface forces,[9] determination of crystal growth mechanisms and kinetics,[10] and fabrication of nanostructures and patterns,[11] to name a few. Another important application of AFM is the measurement of nano- and microscale dimensions of particles and topographical features.[12] Such measurements are performed by scanning a fine tip across the sample and determining of the vertical and horizontal position of the tip at each step. Measurement of the height of objects and protruding features is generally straightforward and fairly accurate with errors in the sub-nanometer range.[13] Lateral AFM measurements, on the other hand, are affected by dilation, also known as tip broadening, of the topography or lateral dimensions due to the finite size of the tip. The tip broadening effect in AFM is related to the effects of finite stylus width on surface-contact profilometry.[14] Figure 3.1 illustrates the tip broadening effect for nanoparticles with a circular and elliptical cross section and a conical tip with a spherical vertex.

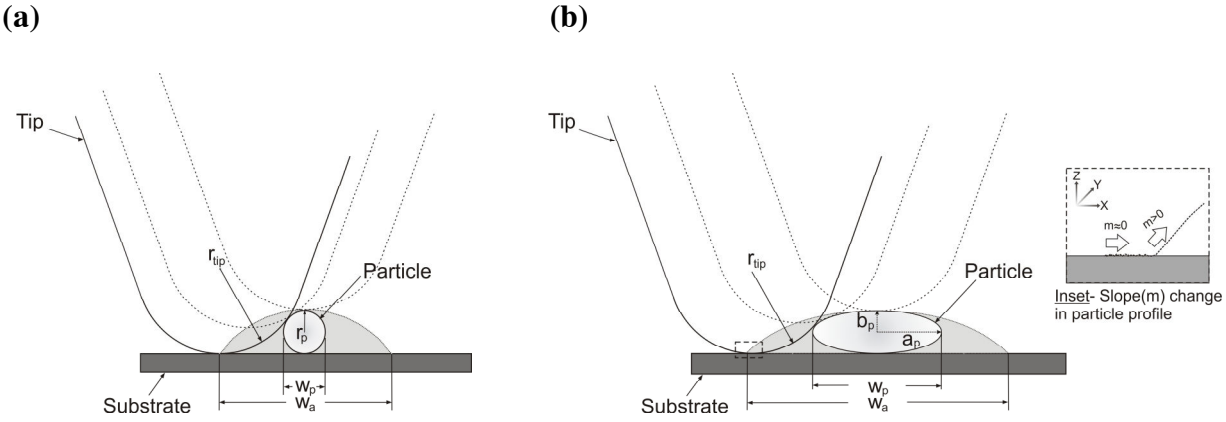

Figure 3.1. Apparent height profiles of nanoparticles with (a) a circular cross section of radius r_p or (b) an elliptical cross section with semi axes a_p and b_p obtained with a conical tip with spherical vertex of radius r_{tip} ($r_{tip} > r_p, b_p$). The magnitude of tip broadening is the difference between the apparent width, w_a, and the actual width, w_p, of the particle. The inset illustrates the sudden change in slope in the apparent height profile when the tip comes in contact with the particle upon scanning across the substrate.

The apparent height profiles shown in Figure 3.1 are specific to cases where the ratio of tip radius, r_{tip}, to particle radius, r_p, for the circular cross section or the semi-minor axis, b_p, for the elliptical cross section, is large enough that only the tip's spherical vertex comes in contact with the particle. If this is the case, the apparent width of an object with circular cross section is related to the tip and particle radii through the equation

$$w_a = 4\sqrt{r_{tip} r_p} \qquad [3.1]$$

which was first derived by Zenhausern *et al.*[15] The tip broadening effect is rooted in the fact that the instrument measures the position of the tip apex not that of the actual point of contact, which deviates from the tip apex in the case of high sample steepness. When the tip's point of contact is different from its apex, the height profile becomes distorted in a non-linear fashion and the form of distortion depends on the geometry of the tip.[16] Keller[17] has shown that the slope of the apparent height profile at the position of the tip apex is equal to the slope of the particle surface (and also that of the tip) at the point of contact. For a parabolic tip and a parabolic sample, he has also shown that the radius of curvature of the sample at the point of contact is equal to the sum of the radii of curvature of the apparent height profile at the tip apex and of the tip at the point of contact, with the radius of curvature of the tip being of opposite sign to the radii of curvature of the sample and the apparent height profile. Reconstruction of the true contour of the sample from a distorted height profile requires detailed knowledge of the tip geometry. Several methods have been developed to obtain information about the shape of the tip, including imaging of the tip by electron microscopy, scanning samples of known topography (tip characterizers), mathematical tip reconstruction methods, and blind tip estimation.[13]

Here, we propose a method for the estimation of the effect of tip broadening that is based on the first and second derivatives of the apparent height profile. The first derivative represents the slope of the height profile at any given tip position and the second derivative represents the curvature, which is the inverse of the radius of curvature of the height profile at that tip position. We will demonstrate the method on gold nanorods of known dimensions and on a polydisperse sample of cellulose nanocrystals (CNCs). CNCs, also referred to as cellulose whiskers, are elongated, crystalline cellulose particles with cross-sectional dimensions of less than 100 nm and

lengths of up to several micrometers. They are generally produced by acid hydrolysis of purified plant-, algae-, microbial-, or animal-based cellulose. The morphology of CNCs is frequently described as rod-like[18-22] although an early study of plant-derived CNCs reported them as being tabular with a width-to-thickness ratio of 4.5.[23] Later studies have provided further evidence of an anisodiametric cross-section.[24-25] The most commonly used techniques for the determination of the dimensions and size distributions of CNCs are transmission electron microscopy (TEM)[23, 25-29] and AFM.[25, 28-31] TEM is generally used to measure the length distributions of CNCs[25-29] whereas AFM is used to measure both length[28, 30-31] and height[25, 28-31] distributions. Very few studies have reported width distributions for CNCs.[25-26, 28] Our goal and, thus, motivation for developing this method is to determine the length, width, and thickness distributions of CNCs solely by AFM. Here, we use simulated transverse AFM height profiles to discuss the shape of the first and second derivatives of the height profiles for cylindrical and elliptic cylindrical nanoparticles and different tip radii and to explain the proposed method. The application of the method to gold nanorods and CNCs is discussed at the end of the chapter.

3.3. Experimental

3.3.1. Height profile simulation

The data for the simulated transverse height profiles of cylindrical nanoparticles were generated with the equation

$$y = 0.02 \cdot \sin x, \qquad \text{for } x < 40 - \sqrt{\left(r_{tip} + r_p\right)^2 - \left(r_{tip} - r_p\right)^2}$$

$$y = r_p - \left\{ r_{tip} - \left[\cos\left\langle \arcsin\left(\frac{\sqrt{4 r_{tip} r_p} - x}{r_{tip} + r_p} \right) \right\rangle \times \left(r_{tip} + r_p\right) \right] \right\}, \qquad [3.2]$$

$$\text{for } 40 - \sqrt{\left(r_{tip} + r_p\right)^2 - \left(r_{tip} - r_p\right)^2} < x < 40 + \sqrt{\left(r_{tip} + r_p\right)^2 - \left(r_{tip} - r_p\right)^2}$$

$$y = 0.02 \cdot \sin x, \qquad \text{for } x > 40 + \sqrt{\left(r_{tip} + r_p\right)^2 - \left(r_{tip} - r_p\right)^2}$$

where r_{tip} and r_p are the radii of the tip and particle, respectively, and x is the distance of the tip traveled from its original location. The sinusoidal components simulate a substrate with an undulating topography.

The data for the simulated transverse height profiles of elliptic cylindrical nanoparticles were generated manually with CorelDRAW (v14.0, Corel Corporation), a vector-based drawing program. In a series of drawings, a circle, representing the cross section of the AFM tip, with radius r_{tip} was moved horizontally from left to right in equal steps over an ellipse with semi-axes a_p and b_p ($b_p < r_{tip}$) having a ratio a_p:b_p of 3:1, representing the cross section of the elliptic cylindrical nanoparticle, in such a way that the two figures touched but did not intersect. At each step, the vertical position, i.e. the position in the direction perpendicular to the direction of motion, of the lowest point of the moving circle, corresponding to the tip apex, was recorded. A horizontal, slightly undulating line below the ellipse, described by the function $y(x) = 0.02 \cdot \sin x$, simulated the sample substrate and was "scanned" to the left and right of the "particle" for reference purposes.

The first and second derivatives of the simulated height profiles were calculated with the differentiation operation and the central differences algorithm of IGOR Pro (v6.12, WaveMetrics), a computer program for scientific graphing, data analysis, and image processing.

3.3.2. Preparation of CNCs

Lap sheets of dissolving-grade softwood sulfite pulp (Temalfa 93A-A), kindly provided by Tembec, Inc., were cut into small pieces and milled (Thomas Wiley mini mill) to pass a 60-mesh screen. The milled pulp was hydrolyzed for 60 min at 50 °C with sulfuric acid (Fisher Scientific, 97.1%, Certified ACS Plus), diluted to 64 wt % with deionized (DI) water (Millipore Direct-Q 5, 18.2 MΩ·cm), at an acid-to-pulp ratio of 10 mL/g. Hydrolysis was stopped by 10-fold dilution of the reaction mixture with cold (4 °C) DI water. The suspension was centrifuged (Thermo IEC

Centra-GP8R) for 10 min at 4500 rpm and 25 °C. The sediment was redispersed in DI water by shaking and the suspension was centrifuged again as described above. The sediment was again redispersed in DI water by shaking and the suspension was dialyzed (Spectra/Por 4 dialysis tubing) against DI water for several days until the pH of the dialysate remained constant. For the disruption of potential CNC aggregates, the CNC suspension was sonicated for 10 min at 40% output using a 500-Watt ultrasonic processor (Sonics Vibra-Cell VC-505). After sonication, the suspension was filtered through a polyvinylidene fluoride syringe filter, having a pore size of 0.45 μm (Whatman GD/XP).

3.3.3. AFM sample preparation

A mica disk of 11 mm in diameter, punched out from a mica sheet (Ted Pella, 1 in by 3 in, grade V1), was glued with common household epoxy adhesive onto a regular microscope slide. The top layers of the mica were removed with sticky tape until an even, fresh mica surface was achieved. The AFM substrate was then immersed at room temperature into an aqueous solution of poly(diallyl-dimethylammonium chloride) (PDDA, Sigma Aldrich, Avg. Mw < 100,000, 35 wt %) diluted to 0.5 wt %. After 15 min, the substrate was rinsed with DI water, and allowed to dry in a fume hood. CNCs were deposited onto the substrate by spin coating of a 0.005 wt % suspension for 30 s at 3000 rpm, with a common spin coater (Laurel Technologies WS-400B-6NPP/Lite). Gold nanorods (Strem Chemicals, axial diameter: 10.0 nm (±10%), length: 41 nm (±10%)) were deposited directly onto the freshly cleaved mica. The original suspension (36 μg/mL (±10%)) was diluted fivefold with DI water and sonicated for 5 min at 35% output. A 5 μL drop was deposited with a pipette onto the mica disk glued to a microscope slide and allowed to dry in a fume hood.

3.3.4. AFM data acquisition

AFM height data for the CNCs were acquired with an Asylum Research MFP-3D atomic force microscopy mounted onto an Olympus IX 71 inverted fluorescence microscope and three different types of tips. The properties of the different tips are listed in Table 3.1. The height data for the gold nanorods were recorded with OMCL-AC160TS tips.

Table 3.1. Properties of the AFM silicon tips used

Tip	Tip material	Nominal tip radius (nm)	Nominal spring constant (N/m)
Nanoworld SSS-NCH	Silicon	<5 nm	42
Olympus OMCL-AC160TS	Silicon	<10 nm	42
Olympus OMCL-AC240TM	Platinum coated silicon	<15 nm	2

Data were recorded in intermittent-contact mode in air with scan sizes of 1 or 5 μm, a scan frequency of 1 Hz, and 512 scans with 512 points/scan. The microscope's performance was assessed according to the manufacturer's diagnostic procedures. The sensor and deflection noise levels, XY scanner hysteresis, and XY sensor linear-variable-differential-transformer offsets were all within the manufacturer's specifications. The calibration of the Z piezo stage was verified with an Asylum Research CalibratAR 3D calibration grating. The error for a step height of 180 nm was less than 1.3%.

3.3.5. AFM data analysis

Analysis of AFM height images was performed with IGOR Pro. AFM height images were first flattened with a flatten order of zero, which was found to accelerate the succeeding operations. The zero-order flattening process fits each scan line with a zero-order polynomial ($P(x) = a_0$) which is subtracted that from the data. Then, the images were flattened with the "Magic Mask" procedure. This procedure performs a first-order flattening, then applies a mask, calculated with the iterative threshold calculation method, and then performs another first-order flattening on the masked image. The process is automatically repeated until the applied changes are smaller than a software-specified value. The first-order flattening process fits each scan line with a first-order polynomial ($P(x) = a_0 + a_1 x$) and subtracts that from the data. Because the first-order flattening was applied to the entire image before the mask was applied, the particle height relative to the background should only be minimally affected by the image flattening. The mean and median height of CNCs was determined from a grid of line profiles parallel to the x- and y-axis with a spacing of 10% of the axis range. For a larger sample size, images of 5 μm by 5 μm were used

instead of 1 μm by 1 μm images. The line profile data was analyzed in Microsoft Excel for height maxima and average background height. Particle thicknesses were calculated by subtraction of the average background height from the height maxima. The tip broadening was estimated as described below from transverse height profiles of individual CNCs taken from 1 μm by 1 μm images.

3.4. Results and discussion

3.4.1. Height profile simulation

Figure 3.2 shows a simulated transverse AFM height profile of a cylindrical nanoparticle of radius 2.125 nm, oriented perpendicular to the scan direction, and the corresponding first and second derivatives for a tip radius of 10 nm and a step size of 1.95 nm, corresponding to an image resolution of 512 scans at 512 points/scan and a scan size of 1 μm. The cross section of the nanoparticle is centered at a distance of 40.0 nm from the original position of the tip apex. The particle radius was chosen in light of the experimental results for CNCs, discussed below. As illustrated in Figure 3.2-a, the simulated height profile exhibits sudden changes in slope at the points P(0) and P(1). These two points represent the positions of the tip apex, in terms of distance from its original position, at the two instances when the tip touches both the substrate and the particle, i.e. when the tip touches the sample at two points simultaneously. To the left of P(0) and to the right of P(1), the tip touches only the substrate and the tip's point of contact coincides with the tip apex. Between P(0) and P(1) the tip touches only the particle but the point of contact of the tip does not coincide with the tip apex, except on the very top of the particle. It is initially on the side of the tip and moves through the tip apex to the other side of the tip as the tip moves across the particle. Whenever the point of contact of the tip does not coincide with the tip apex, the measured height profile is a composite of the profile of the tip and that of the sample. The larger the distance between the point of contact on the tip surface and the tip apex, the larger is the deviation of the apparent height profile from the actual height profile of the sample.

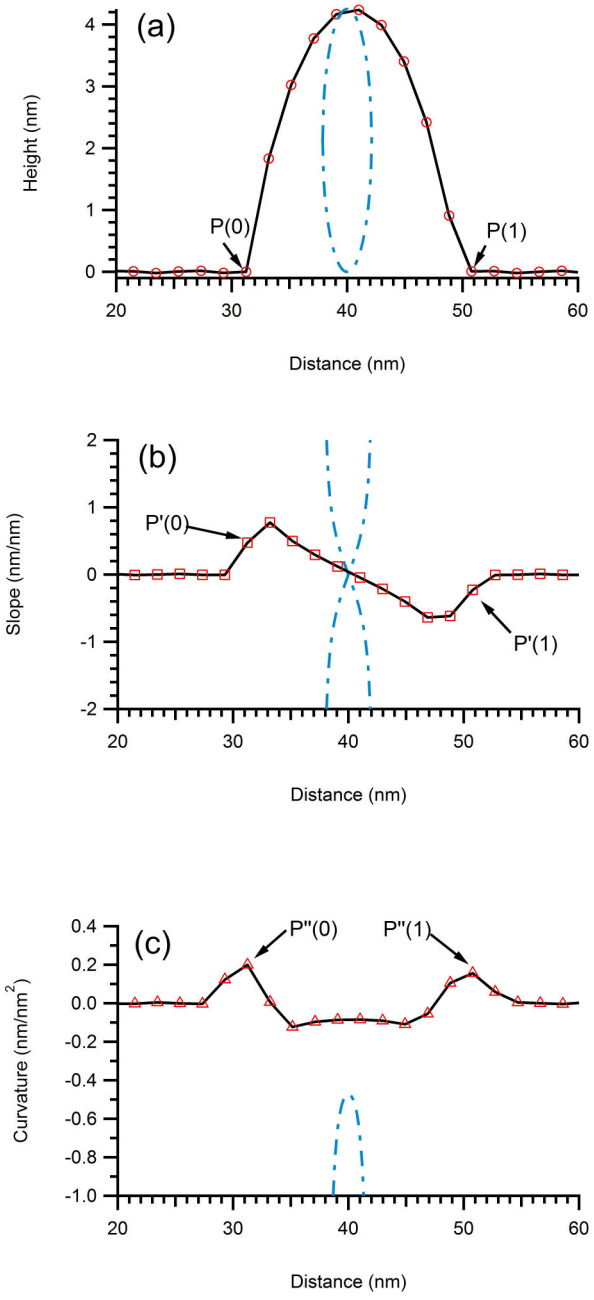

Figure 3.2. Simulated transverse AFM height profile (a) of a cylindrical nanoparticle of radius 2.125 nm and the corresponding first (b) and second (c) derivatives for a tip radius of 10.0 nm and a step size of 1.95 nm. The cross section of the nanoparticle is centered at x = 40.0 nm. The dash-dotted lines correspond to the circular circumference of the cross section.

To illustrate this concept, we have included the curves for the circular circumference of the cross-section of the particle in Figure 3.2 (dash-dotted lines). As can be seen, the simulated curves and the theoretical curves overlap only at and near the maximum height of the particle at x = 40.0 nm. When the tip is on top of the particle, its point of contact is close to or coincides with the tip apex. The distance Δx = P(1) – P(0) represents the apparent width of the particle. The data points corresponding to P(0) and P(1) in the first derivative of the height profile (Figure 3.2-b) are denoted P'(0) and P'(1), respectively. Analogously, the points corresponding to P(0) and P(1) in the second derivative (Figure 3.2-c) are denoted P"(0) and P"(1), respectively. As can be seen in Figure 3.2-c, the points of sudden slope changes in the height profile correspond to the maxima in the second derivative. Because the identification of P"(0) and P"(1) is generally less ambiguous than the identification of P(0) and P(1) in real height profiles, the apparent width of the particle is more easily determined from the second derivative of the height profile as Δx = P"(1) – P"(0).

The transverse height profile of an elliptic cylindrical nanoparticle and its first and second derivatives have the same characteristics as those for a cylindrical nanoparticle, as can be seen in the succeeding figures.

3.4.2. Effect of tip radius

Figure 3.3 shows simulated transverse AFM height profiles of an elliptic cylindrical nanoparticle with a semi minor axis of 2.125 nm and height-to-width proportions of 1:3, oriented perpendicular to the scan direction, and the corresponding first and second derivatives for tip radii of 10.00, 5.00 and 2.50 nm and a step size of 1.95 nm. The cross section of the nanoparticle is centered at a distance of 40.0 nm from the original position of the tip apex. The cross-sectional proportions were chosen in light of the experimental results for CNCs, discussed below. As expected, the curves for the tip with the smallest radius show the strongest overlap with the theoretical curves for the elliptical circumference of the particle's cross section. Moreover, the apparent particle width (distance between the two maxima of the second derivative) is smallest for the tip with the smallest radius.

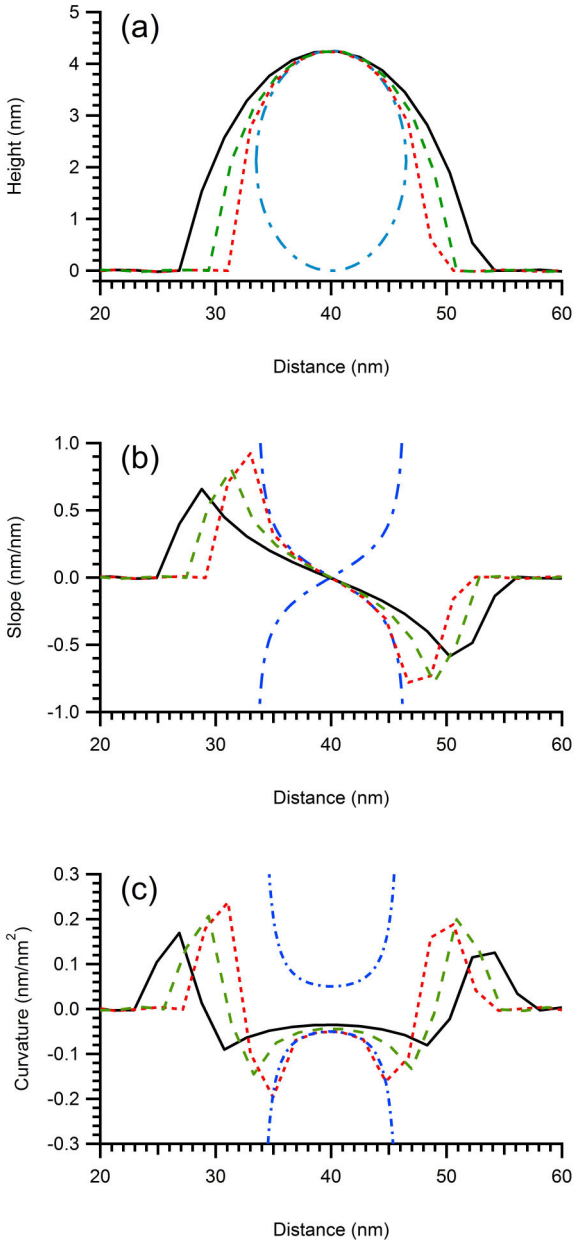

Figure 3.3. Simulated transverse AFM height profiles (a) of an elliptic cylindrical nanoparticle with a semi minor axis of 2.125 nm and height-to-width proportions of 1:3 and the corresponding first (b) and second (c) derivatives for tip radii of 10.00 nm (black solid line), 5.00 nm (green dashed line), and 2.50 nm (red dotted line) and a step size of 1.95 nm. The cross-section of the nanoparticle is centered at x = 40.0 nm. The blue dash-dotted lines correspond to the elliptical circumference of the cross-section.

3.4.3. Estimation of tip broadening

The tip broadening in AFM width measurements of nanoparticles is the difference between the apparent and actual particle width. As shown above, the apparent particle width can be determined from the second derivative of the transverse height profile of the particle. We propose that the actual width of the particle can be estimated from the curve obtained by dividing the first derivative of the height profile by the second derivative. Such curves are shown in Figure 3.4 for a cylindrical nanoparticle of radius 2.125 nm and an elliptic cylindrical nanoparticle with a semi-minor axis of 2.125 nm and a height-to-width ratio of 1:3, oriented perpendicular to the scan direction, for a tip radius of 10 nm and two different step sizes (0.2 and 1.95 nm) together with the apparent transverse height profiles and particle circumferences. The cross-sections of the nanoparticles are centered at a distance of 40.0 nm from the original position of the tip apex.

As seen in Figure 3.4, the curve obtained by dividing the first derivative of the height profile by the second derivative has a quasi-linear section at the center of the particle's cross-section and the beginning and end of the quasi-linear section correlate fairly well with the edges of the cross-section of the particle. Therefore, we propose that the points at which this curve deviates from a straight line can be used to estimate the actual width of the nanoparticle. The greater fluctuations in the data for the elliptic cylindrical particle were due to the manual method of simulation. For a step size of 0.2 nm (Figures 3.4-a and 3.4-d), the proposed method gave particle widths of 4.40 nm for the cylindrical and 12.60 nm for the elliptic cylindrical particle and for a step size of 1.95 nm (Figures 3.4-b and 3.4-c) it gave particle widths of 5.86 nm for the cylindrical and 11.72 nm for the elliptic cylindrical particle. All measured widths were within ± one step of the true width of the particle (4.25 nm for the cylindrical and 12.75 nm for the elliptical particle). An absolute error of ±1.95 nm represents a relative error of ±46% for the cylindrical and ±15% for the elliptic cylindrical particle. It is obvious that the accuracy of the method depends on the ratio of the step size to the actual width of the particle, i.e. accurate measurements of smaller particle widths require smaller step sizes.

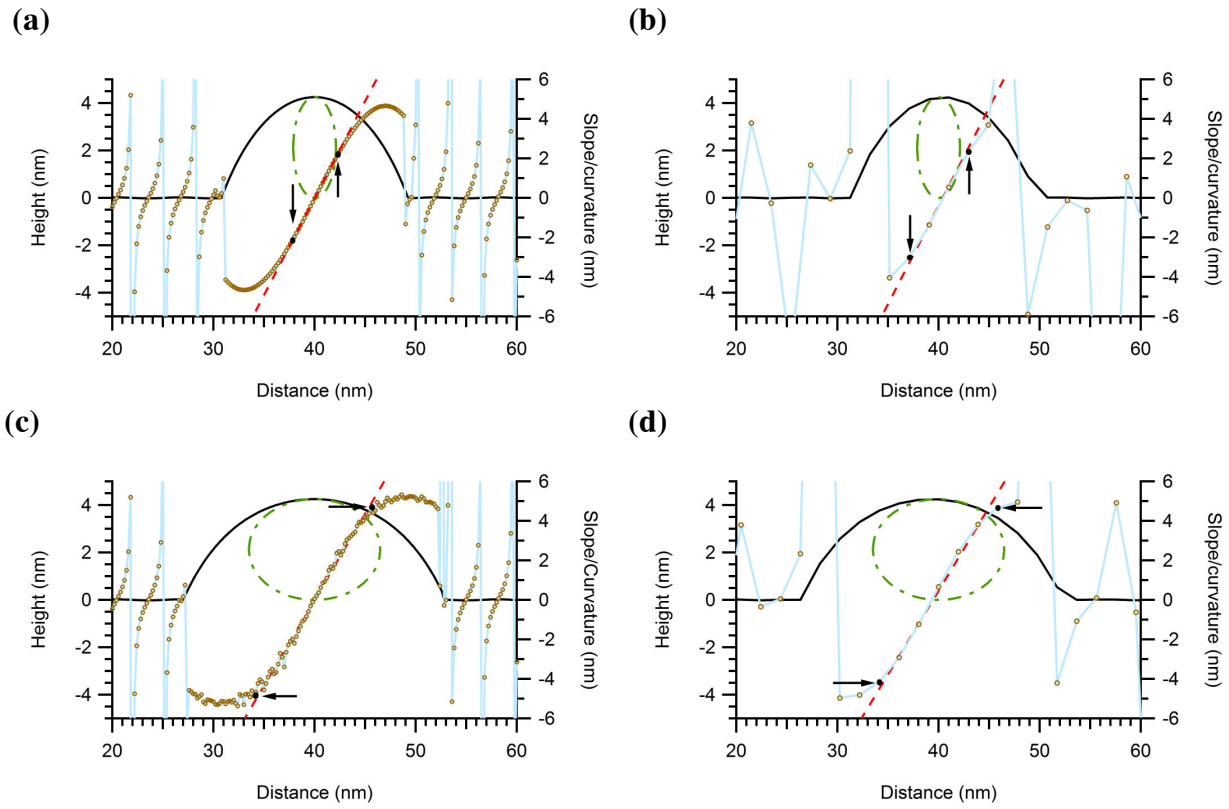

Figure 3.4. Proposed method for the estimation of the actual particle width for a cylindrical nanoparticle of radius 2.125 nm (a, b) and an elliptic cylindrical nanoparticle with a semi minor axis of 2.125 nm and height-to-width proportions of 1:3 (c, d) and for step sizes of 0.2 nm (a, c) and 1.95 nm (b, d). The cross section of the nanoparticle is centered at x = 40.0 nm. The particle width is estimated from the length in the x-direction of the quasi-linear section of the curves obtained by dividing the first derivative of the height profile by the second derivative (open circles). The solid lines are the apparent transverse height profiles and the dash-dotted lines are the circumferences of the particles. The dashed lines are linear fits of the quasi-linear section of the curves.

3.4.4. Experimental results

The root-mean-square (RMS) surface roughness of the freshly-cleaved mica for 1 μm by 1 μm areas was 0.075±0.01 nm. This value was in good agreement with values reported in the literature (e.g. 0.054 nm).[32] The RMS surface roughness of the PDDA-coated mica was with

0.082±0.02 nm only slightly higher than that of the freshly-cleaved mica but still sufficiently low for particle size analysis.

Figure 3.5 shows an AFM height image of two gold nanorods on mica and the apparent transverse height profile of one of the nanorods together with the curve obtained by dividing the first derivative of the height profile by the second derivative. The quasi-linear section of the curve can be easily identified. The estimated actual width of the nanorod was 10.07 nm, which was in excellent agreement with the diameter of 10.0 nm, specified by the manufacturer. The height of the nanorod was measured as 9.36 nm. The apparent width, determined from the second derivative of the apparent height profile, was 26.17 nm. Thus, the magnitude of tip broadening, calculated from the difference between the apparent and actual width, was 16.1 nm.

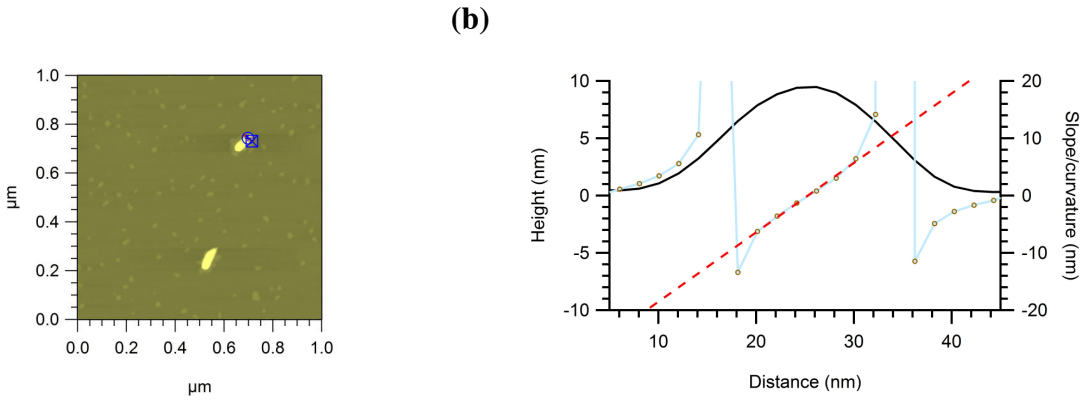

Figure 3.5. Estimation of the actual width of a gold nanorod of 10 nm nominal diameter. (a) AFM height image, z-scale = 10.00 nm and (b) apparent transverse height profile (solid line) and curve obtained by dividing the first derivative of the height profile by the second derivative (open circles). The dashed line is a linear fit of the quasi-linear section of the curve. The arrows indicate the beginnig and end of the quasi-linear section of the curve and, thus, the actual width of the nanorod (10.07 nm).

Figure 3.6 shows AFM height images of a group of CNCs on PDDA-coated mica imaged with three different AFM tips and the apparent transverse height profiles of one of the CNCs together with the curves obtained by dividing the first derivative of the height profile by the second derivative.

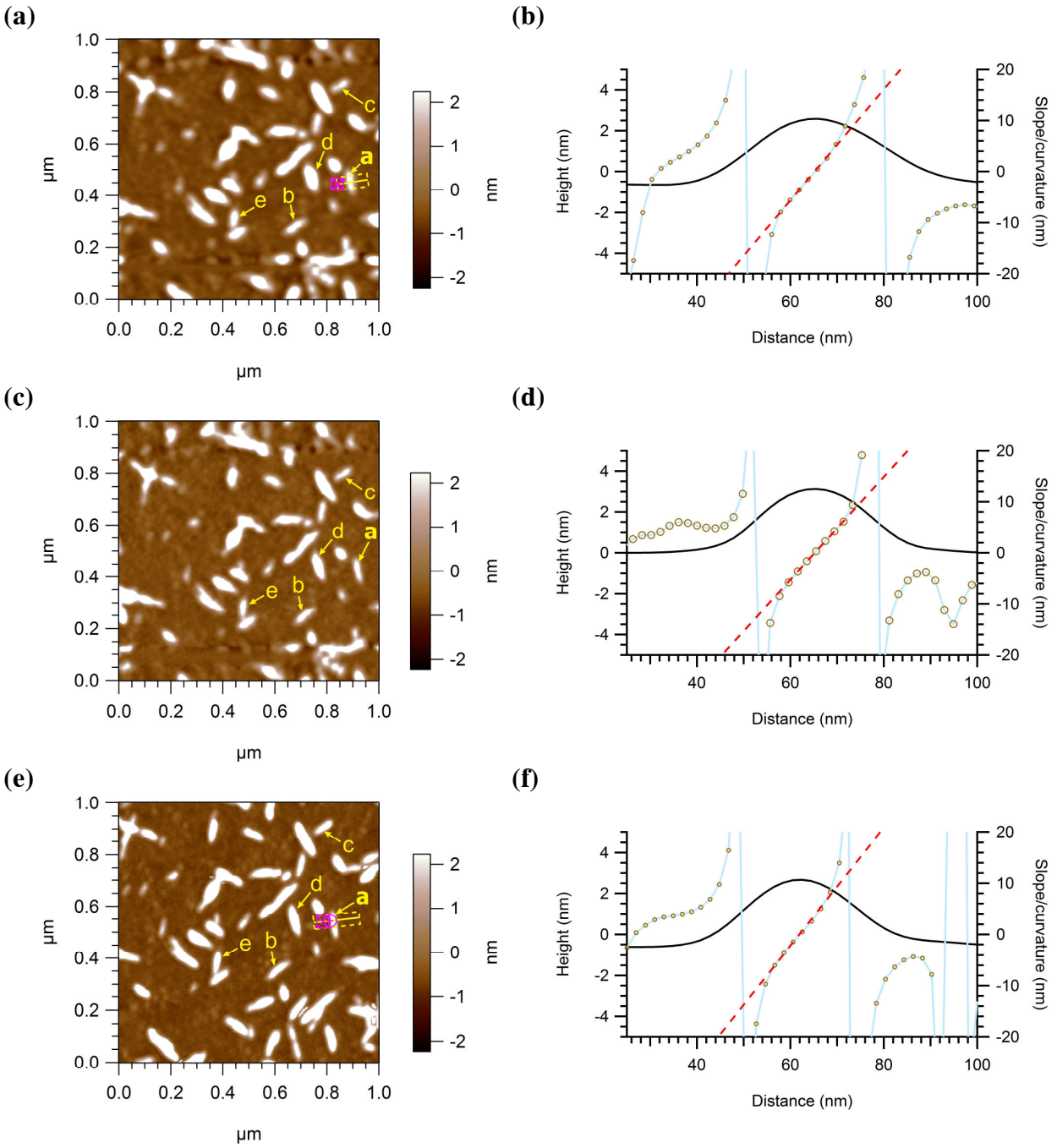

Figure 3.6. AFM height images of a group of CNCs (*a*–*e*) acquired with different AFM tips, having nominal radii of r_{tip} < 15 nm (a), < 10 nm (c), and < 5 nm (e), and the apparent transverse height profiles (solid lines) of particle *a* and curves obtained by dividing the first derivative of the height profile by the second derivative (open circles). The dashed lines are linear fits of the quasi-linear sections of the curve.

The effect of the tip radius on the magnitude of tip broadening was clearly apparent in the AFM height images of the CNCs. The CNCs appeared broader and less anisometric in the image acquired with the tip with the largest nominal radius (Figure 3.6-a) than in the image acquired with the tip with the smallest nominal radius (Figure 3.6-c). Because the height and width of CNCs were less uniform along the length of the particles than those of the gold nanorods, we used a line width of 50 nm to generate the height profile. It means that the height values are average values for 50 nm long longitudinal sections of the CNC. For all tips, the quasi-linear section of the curve obtained by dividing the first derivative of the height profile of particle *a* by the second derivative can be easily identified (Figures 3.6-b, 3.6-d, and 3.6-f).

Table 3.2 lists the apparent widths, w_a, and estimated actual widths, w_p, of the CNCs labeled *a–e* in Figure 3.6 and the calculated magnitudes of tip broadening, $w_a–w_p$.

Table 3.2. Apparent width, w_a, estimated actual width, w_p, and magnitude of tip broadening, $w_a – w_p$, for five different particles and three different AFM tips.

	Olympus OMCL-AC240TM			Olympus OMCL-AC160TS			Nanoworld SSS-NCH		
Particle	w_a (nm)	w_p (nm)	$w_a – w_p$ (nm)	w_a (nm)	w_p (nm)	$w_a – w_p$ (nm)	w_a (nm)	w_p (nm)	$w_a – w_p$ (nm)
A	43.34	11.82	31.52	35.29	11.76	23.53	25.56	11.81	15.00
B	45.39	11.83	33.56	35.47	11.82	23.65	25.53	11.76	13.77
C	45.63	11.90	33.73	33.36	11.77	21.59	25.52	11.81	13.71
D	56.87	21.57	35.30	41.67	19.84	21.83	33.45	21.64	11.81
E	47.27	15.75	31.52	39.16	15.66	23.50	27.42	15.70	11.72
		Mean:	**33.13±1.60**		**Mean:**	**22.82±1.02**		**Mean:**	**12.95±1.08**

The estimated actual widths obtained for each particle with the different tips were in good agreement with each other. Particles *a–c* had an estimated actual average width of about 11.8 nm. For the height of CNCs we obtained a mean value of 4.27±0.22 nm and a median of 4.32±0.30 nm in good agreement with AFM-based height values reported in the literature for wood pulp-derived CNCs (4.5-5.0 nm).[30] The similarity and low standard deviations of the mean

and median height values indicated that CNC height was fairly uniform. The estimated width of 11.8 nm and measured height of 4.3 nm support the hypothesis of a non-circular cross section, formed originally by Mukherjee and Woods[23] and supported later by others.[24-25] The width-to-height ratio of 2.7 was smaller than that reported by Mukherjee and Woods of 4.5.[23] The difference could be due to the difference in analysis methods used. Mukherjee and Woods measured the heights and widths of CNCs from TEM images of shadowed samples and might have underestimated the height. Their height values were much smaller than those measured by us and reported by others.[25, 30] The large estimated actual width of particle *d* of nearly twice the average width of particles *a–c* suggested that particle *d* was a lateral aggregate of two CNCs. The estimated actual width of particle *e* was 1.25 times the average width of particles *a–c*. Particle *e* might be an aggregate of two particles with both of the particles not lying flat on the substrate.

The calculated magnitudes of tip broadening, $w_a - w_p$, obtained for the different particles with each tip were in good agreement with each other as shown by the low standard deviation of the mean value of the tip broadening. As expected, the mean values obtained for the different tips decreased with decreasing tip radius. The limited variation in the observed tip broadening magnitude between the different particles suggests that tip broadening can be considered constant for a given sample and tip as long as the tip is not damaged or contaminated. It should therefore be acceptable to determine the magnitude of the tip broadening effect for a given sample and tip from a small number of particles and use the determined value to correct the apparent lengths and widths of all particles within the sample.

3.5. Conclusions

We have proposed a method for the estimation of the tip broadening effect in AFM width measurements of CNCs. The method is based on the first and second derivatives of the apparent transverse height profiles of the non-spherical nanoparticles. The magnitude of tip broadening is calculated from the difference between the apparent width and the actual width of the particle. The apparent width is most easily determined from the two maxima in the second derivative of the apparent transverse height profile. The actual width is determined from the quasi-linear

section of the curve obtained by dividing the first derivative of the apparent transverse height profile by the second derivative. The thus estimated actual width is independent of tip radius. CNCs prepared from dissolving-grade softwood pulp by sulfuric acid hydrolysis have an actual average width of about 11.8 nm and a width-to-height ratio of about 2.7, *i.e.* a non-circular cross section. The magnitude of tip broadening decreases with decreasing tip radius and is constant within a sample. The accuracy of the method depends on the spacing of the data points in the height profile. The fact that the magnitude of tip broadening is constant within a sample indicates that, once determined from a small number of particles, it can be used to correct the apparent width and length values of all particles within the sample for tip broadening.

3.6. Acknowledgements

This material is based upon work supported by the National Research Initiative of the USDA Cooperative State Research, Education and Extension Service, grant number 2005-35504-16088, and by the National Science Foundation under grant numbers CHE-0724126 and DMR-0907567. The authors also gratefully acknowledge the generous scholarship support for F. N. by the Mexican Secretariat of Public Education (SEP) through its Professional Development for Teachers Program (PROMEP). Furthermore, additional support from OMNOVA, Inc. and Tembec, Inc. are also acknowledged.

3.7. References

1. Binnig, G.; Quate, C. F.; Gerber, C. Atomic Force Microscope. *Physical Review Letters* **1986,** 56, 930-933.
2. Martin, Y.; Williams, C. C.; Wickramasinghe, H. K. Atomic Force Microscope Force Mapping and Profiling on a Sub 100-A Scale. *Journal of Applied Physics* **1987,** 61, 4723-4729.
3. Magonov, S. N.; Reneker, D. H. Characterization of polymer surfaces with atomic force microscopy. *Annual Review of Materials Science* **1997,** 27, 175-222.

4. Giessibl, F. J. Advances in atomic force microscopy. *Reviews of Modern Physics* **2003,** 75, 949-983.
5. Frommer, J. Scanning Tunneling Microscopy and Atomic Force Microscopy in Organic-Chemistry. *Angewandte Chemie-International Edition in English* **1992,** 31, 1298-1328.
6. Lal, R.; John, S. A. Biological Applications of Atomic-Force Microscopy. *American Journal of Physiology* **1994,** 266, C1-&.
7. Shao, Z. F.; Mou, J.; Czajkowsky, D. M.; Yang, J.; Yuan, J. Y. Biological atomic force microscopy: What is achieved and what is needed. *Advances in Physics* **1996,** 45, 1-86.
8. Henderson, E. Imaging of Living Cells by Atomic-Force Microscopy. *Progress in Surface Science* **1994,** 46, 39-60.
9. Cappella, B.; Dietler, G. Force-distance curves by atomic force microscopy. *Surface Science Reports* **1999,** 34, 1–103.
10. McPherson, A.; Malkin, A. J.; Kuznetsov, Y. G. Atomic force microscopy in the study of macromolecular crystal growth. *Annual Review of Biophysics and Biomolecular Structure* **2000,** 29, 361-410.
11. Ginger, D. S.; Zhang, H.; Mirkin, C. A. The evolution of dip-pen nanolithography. *Angewandte Chemie-International Edition* **2004,** 43, 30-45.
12. Griffith, J. E.; Grigg, D. A. Dimensional Metrology with Scanning Probe Microscopes. *Journal of Applied Physics* **1993,** 74, R83-R109.
13. Yacoot, A.; Koenders, L. Aspects of scanning force microscope probes and their effects on dimensional measurement. *Journal of Physics D-Applied Physics* **2008,** 41.
14. O'Donnell, K. A. Effects of finite stylus width in surface contact profilometry. *Applied Optics* **1993,** 32, 4922-4928.
15. Zenhausern, F.; Adrian, M.; Tenheggelerbordier, B.; Eng, L. M.; Descouts, P. DNA and RNA Polymerase/DNA Complex Imaged by Scanning Force Microscopy - Influence of Molecular-Scale Friction. *Scanning* **1992,** 14, 212-217.
16. Hahlweg, C.; Gruhlke, M.; Rothe, H. Nonlinear distortion in atomic force microscopy (AFM) measurements. *Measurement Science & Technology* **2009,** 20.
17. Keller, D. Reconstruction of STM and AFM images distorted by finite-size tips. *Surface Science* **1991,** 253, 353–364.

18. Dong, X. M.; Gray, D. G. Effect of counterions on ordered phase formation in suspensions of charged rodlike cellulose crystallites. *Langmuir* **1997,** 13, 2404–2409.
19. Bonini, C.; Heux, L.; Cavaillé, J. Y.; Lindner, P.; Dewhurst, C.; Terech, P. Rodlike cellulose whiskers coated with surfactant: A small-angle neutron scattering characterization. *Langmuir* **2002,** 18, 3311–3314.
20. De Souza Lima, M. M.; Wong, J. T.; Paillet, M.; Borsali, R.; Pecora, R. Translational and rotational dynamics of rodlike cellulose whiskers. *Langmuir* **2003,** 19, 24–29.
21. De Souza Lima, M. M.; Borsali, R. Rodlike cellulose microcrystals: Structure, properties, and applications. *Macromolecular Rapid Communications* **2004,** 25, 771–787.
22. Yi, J.; Xu, Q. X.; Zhang, X. F.; Zhang, H. L. Chiral-nematic self-ordering of rodlike cellulose nanocrystals grafted with poly(styrene) in both thermotropic and lyotropic states. *Polymer* **2008,** 49, 4406–4412.
23. Mukherjee, S. M.; Woods, H. J. X-ray and electron microscope studies of the degradation of cellulose by sulphuric acid. *Biochimica et biophysica acta* **1953,** 10, 499–511.
24. Terech, P.; Chazeau, L.; Cavaillé, J. Y. A Small-Angle Scattering Study of Cellulose Whiskers in Aqueous Suspensions. *Macromolecules* **1999,** 32, 1872–1875.
25. Elazzouzi-Hafraoui, S.; Nishiyama, Y.; Putaux, J. L.; Heux, L.; Dubreuil, F.; Rochas, C. The shape and size distribution of crystalline nanoparticles prepared by acid hydrolysis of native cellulose. *Biomacromolecules* **2008,** 9, 57–65.
26. Araki, J.; Wada, M.; Kuga, S.; Okano, T. Flow properties of microcrystalline cellulose suspension prepared by acid treatment of native cellulose. *Colloids and Surfaces, A: Physicochemical and Engineering Aspects* **1998,** 142, 75–82.
27. Dong, X. M.; Revol, J.-F.; Gray, D. G. Effect of microcrystallite preparation conditions on the formation of colloid crystals of cellulose. *Cellulose* **1998,** 5, 19–32.
28. Kvien, I.; Tanem, B. S.; Oksman, K. Characterization of cellulose whiskers and their nanocomposites by atomic force and electron microscopy. *Biomacromolecules* **2005,** 6, 3160–3165.
29. Hirai, A.; Inui, O.; Horii, F.; Tsuji, M. Phase Separation Behavior in Aqueous Suspensions of Bacterial Cellulose Nanocrystals Prepared by Sulfuric Acid Treatment. *Langmuir* **2009,** 25, 497–502.

30. Beck-Candanedo, S.; Roman, M.; Gray, D. G. Effect of reaction conditions on the properties and behavior of wood cellulose nanocrystal suspensions. *Biomacromolecules* **2005,** 6, 1048–1054.
31. Hasani, M.; Cranston, E. D.; Westman, G.; Gray, D. G. Cationic surface functionalization of cellulose nanocrystals. *Soft Matter* **2008,** 4, 2238–2244.
32. Simpson, G. J.; Sedin, D. L.; Rowlen, K. L. Surface roughness by contact versus tapping mode atomic force microscopy. *Langmuir* **1999,** 15, 1429–1434.

Chapter 4

Comparison of AFM and DLS for Particle Size Determination of Cellulose Nanocrystals

Comparison of AFM and DLS for Particle Size Determination of Cellulose Nanocrystals

Fernando Navarro and Maren Roman

Macromolecules and Interfaces Institute and Department of Wood Science and Forest Products, 230 Cheatam Hall, Virginia Polytechnic Institute and State University, Blacksburg, Virginia, 24061, United States of America.

4. 1. Abstract

The size characterization of non-spherical nanoparticles by atomic force microscopy (AFM) is hampered by the tip broadening effect. We have recently reported a method for the estimation of the tip broadening effect in AFM width measurements of cellulose nanocrystals (CNCs) (Chapter 3). On the basis of this method, the objectives of this study were to determine the distributions of CNC length, width, and thickness from AFM data and to correlate the obtained mean dimensions with the length, diameter, and equivalent spherical hydrodynamic diameter obtained from dynamic light scattering (DLS) and depolarized dynamic light scattering (DDLS) measurements. CNCs were prepared from softwood sulfite pulp by H_2SO_4 hydrolysis. Four different AFM sample preparation methods were evaluated. The best samples were obtained by spin coating of CNCs onto polycation-treated mica. AFM image analysis gave positively skewed, log normal-type length, width, and thickness distributions and a mean length of 115.6±82.0 nm, mean width of 13.3±7.0 nm, and mean thickness of 4.3±1.2 nm. The median values for length, width, and thickness were 89.5, 12.1, and 4.3 nm, respectively. DLS and DDLS gave length and diameter values of 136.9 and 18.8 nm, respectively. The equivalent spherical hydrodynamic diameter obtained with a DLS-based particle size analyzer was 142.1 nm. DLS-based methods gave larger dimensions for the CNCs, compared with data from the AFM analysis of the CNCs.

Keywords: *cellulose nanocrystals, AFM, image analysis, dynamic light scattering, particle size analysis.*

4. 2. Introduction

Cellulose nanocrystals (CNCs), also referred to as cellulose whiskers, are elongated, crystalline cellulose particles with cross-sectional dimensions of less than 100 nm and lengths of up to several micrometers. They are generally produced by acid hydrolysis of purified plant-, algae-, microbial-, or animal-based cellulose. CNCs are rapidly gaining attention as sustainable nanoparticles on account of the renewability and environmental degradability of their starting materials. They have been extensively studied for their ability to form colloidal liquid crystalline phases[1-8] and their potential application in polymer nanocomposites.[9-12]

The morphology of CNCs is frequently described as rod-like[6, 13-16] although an early study of plant-derived CNCs reported them as being tabular with a width-to-thickness ratio of 4.5.[17] Later studies have provided further evidence of an anisodiametric cross section.[18-19] Various methods have been used to analyze the dimensions of CNCs, including transmission electron microscopy (TEM),[4, 7, 17, 19-21] scanning electron microscopy (SEM),[21] atomic force microscopy (AFM),[7, 19, 21-23] small angle neutron scattering (SANS),[18] small angle x-ray scattering (SAXS),[18] conventional dynamic light scattering (DLS),[4] and a combination of conventional DLS and depolarized DLS (DDLS).[14] The reported dimensions are summarized in Table 4.1.

As shown in Table 4.1, the most frequently used methods for CNC size analysis are TEM and AFM, either alone or in combination. Microscopy-based methods have the advantage that they provide information about the morphology of the particles in addition to their size and that each particle contributes equally to the distribution. To give accurate results, microscopy-based methods require careful specimen preparation so that specimens contain a representative sample of the particle population and the particles are well separated on the substrate. TEM has the drawback that it is relatively expensive, time consuming, and that it does not allow determination of the particle thickness. In addition, obtaining the necessary image contrast is a challenge when analyzing CNCs by TEM because of their low electron density. AFM is less costly than TEM and provides accurate thickness values but has the drawback that particle length and width values are affected by tip broadening effects.

Table 4.1. Previously reported mean dimensions of CNCs determined by different methods.

Source	Method	Mean Length (nm)[a]	Mean Width (nm)[a]	Mean Thickness (nm)[a]	Ref
Ramie	TEM[b]	< 250	15.5	3.5	17
Cotton	TEM[b]	< 250	13	2.5	17
Cotton	TEM	75, 107	-	-	4
Cotton	DLS	177-390[c]	-	-	4
Cotton	DLS-DDLS	255	15[d]	-	14
Cotton	TEM, AFM	105-141 (TEM)	18-34 (TEM)	7.3 (AFM)	19
Cotton	AFM	176	-	13	23
Tunicin	TEM, AFM	1073 (TEM)	28 (TEM)	10.6 (AFM)	19
Tunicin	SANS, SAXS	-	18.2	8.8	18
Tunicin	DLS-DDLS	1160	16[d]	-	14
Bacterial cellulose	TEM, AFM	800, 1670 (TEM)	40, 54 (TEM)	8.5, 9.8 (AFM)	7
Wood pulp (MCC)	TEM	210	5	-	21
Wood pulp (MCC)	SEM	475	-	-	21
Wood pulp (MCC)	AFM	420	-	-	21
Wood pulp (Avicel)	TEM	105	12	-	19
Softwood pulp	TEM	180	3.5	-	20
Softwood pulp	AFM	105-145	-	4.5-5.0	22
Hardwood pulp	AFM	147	-	4.8	22

[a] multiple values and ranges indicate different experimental conditions, [b] chromium-shadowed specimens, [c] assumes a particle diameter of 7 nm, [d] cross-sectional diameter

Light scattering-based methods (DLS and DDLS) have the advantage that they are less time consuming than microscopy-based methods and that particles are analyzed in liquid suspension. As a result, sample preparation is less challenging and light scattering-based methods are less prone to drying-induced artifacts. The drawbacks of light scattering-based methods are that their accuracy is limited to narrow, monomodal distributions and that DLS-based particle size distributions are weighted toward larger particles because larger particles scatter light more strongly than smaller ones. An additional drawback of conventional DLS is that it only provides an equivalent spherical diameter, which does not correlate well with the dimensions of non-spherical particles, unless some dimensions of the non-spherical particles are known, in which case the unknown dimension can be calculated.

We have recently presented a method for the estimation of the tip broadening effect in particle size measurements by AFM.[24] Based on this method, the objectives of this study were to determine from AFM data the distributions of particle length, width, and thickness in a CNC sample and to correlate the obtained mean dimensions with the length, diameter, and equivalent spherical hydrodynamic diameter obtained from DLS and DDLS measurements.

4. 3. Experimental section

4. 3. 1. CNC preparation

The starting material for the CNCs was dissolving-grade softwood sulfite pulp (Temalfa 93A-A), kindly provided by Tembec, Inc. Lap sheets of the pulp were cut and milled using a Wiley mill (Thomas Wiley mini-mill) to pass a 60-mesh screen. The milled pulp was hydrolyzed with concentrated sulfuric acid (Fisher Scientific, 97.1%) diluted to 64.0 wt %, at a temperature of 50 ºC, an acid-to-pulp ratio of 10 mL/g, and a hydrolysis time of 60 min. Hydrolysis was stopped by 10-fold dilution of the reaction mixture with cold (4 ºC) deionized (DI) water (Millipore Direct-Q5, 18.2 MΩ·cm). The CNC suspensions were centrifuged (Thermo IEC Centra-GP8R) for 10 min at 25 ºC and 4500 RPM, then washed once with DI water and centrifuged again. The collected sediment was dialyzed (Spectra/Por dialysis tubing, MWCO=12-14 kDa) against DI water for several days until the pH of the dialysis medium remained constant. For disruption of possible aggregates, the suspension of CNCs in DI water was sonicated (Vibra-Cell VC-505, 500 Watt, Sonics & Materials, Inc.) for 10 min at 40 % amplitude in an ice bath, preventing overheating of the suspension. After sonication, the suspension was filtered through a 0.45 μm polyvinylidene fluoride syringe filter (Whatman GD/XP). The concentration of the CNC suspension was measured by gravimetric analysis. Aliquots of 5 mL were dried in oven-dried aluminum pans in a regular convection oven for 2 h at 100 ºC. The suspension concentration was calculated from the weights of the aluminum pans before and after water removal. Measurements were carried out in triplicate.

4. 3. 2. AFM sample preparation

Four different sample preparation methods were evaluated. In all cases, the substrate was a mica disk of 11 mm in diameter, punched out from a mica sheet (Ted Pella, 1 in x 3 in, grade V1) and glued with common household epoxy adhesive onto a regular microscope slide. The top layers of the mica were removed with sticky tape until an even, fresh mica surface was achieved. In the first method, a 5 μL drop of a 0.001 wt % CNC suspension was placed onto the freshly cleaved mica surface and allowed to dry at room temperature in a fume hood. In the second method, a 0.005 wt % CNC suspension was spin coated (Laurell Technologies Corporation, WS-400B-6NPP/Lite) for 60 s at 3000 RPM onto the freshly cleaved mica surface. In the third method, the freshly-cleaved mica surface was immersed for 30 min at room temperature into an aqueous solution of poly(sodium 4-styrene sulfonate) (PSS, MW 70K, 30 wt % in water, Sigma-Aldrich) that had been diluted to 0.5 wt %. The substrate was rinsed with DI water, dried in a stream of nitrogen, and stored in a closed container until sample deposition. Deposition of CNCs onto the PSS-treated mica was done by spin coating as described above. In the fourth method, the freshly cleaved mica surface was immersed for 30 min at room temperature into an aqueous solution of poly (diallyldimethyl ammonium chloride) (PDDA, MW<100K, 35 wt % in water, Sigma-Aldrich) that had been diluted to 0.5 wt %. The substrate was rinsed with DI water, dried in a stream of nitrogen, and stored in a closed container until sample deposition. Deposition of CNCs onto the PDDA-treated mica was done by spin coating as described above.

4. 3. 3. AFM data acquisition

AFM data acquisition was done with an Asylum Research MFP-3D-Bio atomic force microscope mounted onto an Olympus IX 71 inverted fluorescence microscope. Height images of the samples were recorded in air in intermittent contact mode (1 Hz, 512 scans, and 512 points/scan) at random locations with Olympus OMCL-AC160TS silicon tips (nominal tip radius <10 nm, spring constant 42 N/m).

The microscope's accuracy was assessed according to the manufacturer's diagnostic procedures. The sensor and deflection noise levels, XY scanner hysteresis, and XY sensor linear-variable-

differential-transformer offsets were all within the manufacturer's specifications. The calibration of the Z piezo stage was verified with an Asylum Research CalibratAR 3D calibration grating. The error for a step height of 180 nm was less than 1.3%.

4. 3. 4. AFM data analysis

Analysis of AFM height images was performed with the Igor Pro scientific graphing and data analysis program (v6.04). Several images per sample were analyzed so that the number of measured particles per sample exceeded 500. Before being analyzed, AFM height images were first flattened with a flatten order of zero, which was found to accelerate the succeeding operations. The zero-order flattening process fits each scan line with a zero-order polynomial $(P(x) = a_0)$ and subtracts that from the data. Then, the images were flattened with the "Magic Mask" procedure. This procedure performs a first-order flattening, then applies a mask, calculated with the iterative threshold calculation method, and then performs another first-order flattening on the masked image. The process is repeated until the applied changes are smaller than a software-specified value. The first-order flattening process fits each scan line with a first-order polynomial $(P(x) = a_0 + a_1 x)$ and subtracts that from the data. Because the first-order flattening was applied to the entire image before the mask was applied, the measured height relative to the background should only be minimally affected by the image flattening.

CNC thickness distributions were obtained from a grid of line profiles parallel to the x- and y-axis with a spacing of 10 % of the axis range. The line profile data was analyzed in Microsoft Excel for height maxima and average background height. Particle thicknesses were calculated by subtraction of the average background height from the height maxima. For determination of the length and width distributions, the flattened height images needed to be converted to binary images. To this end, a user-defined image threshold operation was performed. The threshold was set manually to a value of 0.5 nm above the average background height. The threshold calculation method (manual) and threshold value (0.5 nm) had been optimized by comparison of calculated length and width values, obtained with different threshold calculation methods, such as iterative, adaptive, or fuzzy entropy, and manual threshold values, with values determined manually from height profiles.

Analysis of the binary image with the image-processing package of the software gave the areas and perimeters in pixels of the individual particles. Under the assumption of a rectangular top profile, the length, L, and width, w, of each particle could be calculated from its area and perimeter with the two equations

$$Area = L \cdot w \qquad [4.1]$$

$$Perimeter = 2L + 2w \qquad [4.2]$$

The calculated lengths and widths were corrected for tip broadening by subtraction of the magnitude of tip broadening from the measured length and width values. The magnitude of tip broadening was estimated, as described elsewhere,[24] from height profiles of individual CNCs, taken perpendicular to the long axis of the particles in 1 μm x 1 μm AFM height images. Briefly, for each particle the measured width of the particle was determined from the distance between the two maxima in the second derivative of the height profile. The actual width was estimated from beginning and end of the linear section of the curve obtained by dividing the first derivative of the height profile by the second derivative. The magnitude of tip broadening was calculated for each particle from the difference between the measured and actual width and averaged over all particles.

4. 3. 5. DLS length and diameter measurement

The DLS-based length and diameter of CNCs were determined by a combination of DLS and DDLS measurements. The measurements were performed with an ALV/CGS-3 Compact Goniometer (ALV-GmbH), equipped with a He-Ne laser source (633 nm, 22 mW), a photodiode detector mounted onto a variable angular system (range: 12-152°, resolution: 0.025°), and a Multiple Tau Digital Realtime Correlator, model ALV-5000. Dilute CNC suspensions with four different concentrations, ranging from 0.01 to 0.08 wt %, were analyzed at seven different scattering angles between 30 and 120°. Diffusion coefficients were obtained from the autocorrelation functions with the CONTIN algorithm. Immediately before being analyzed, samples were sonicated for 10 min in an ultrasonic bath (Cole Palmer 8890, 42 kHz). Experiments were carried out in triplicate for error estimation.

4. 3. 6. Measurement of the equivalent spherical hydrodynamic diameter

The equivalent spherical hydrodynamic diameter of CNCs was measured with a Malvern Instruments Zetasizer Nano ZS particle analyzer equipped with a He-Ne laser light (633 nm, 4.0 mW) and a photodiode detector located at 173°. CNC suspensions with different concentrations were prepared from a 1 wt % suspension by sequential two-fold dilution to ~ 0.001 wt %. Immediately before being analyzed, samples were sonicated for 10 min in an ultrasonic bath (Cole Palmer 8890, 42 kHz, 70 W) and then transferred to Malvern Instruments DTS0012 sizing disposable cuvettes. The intensity average hydrodynamic diameter was calculated from the autocorrelation function with Malvern Instrument's DTS^{TM} v4.10 software using the CONTIN algorithm. Measurements were carried out in quintuplicate for error calculation.

4. 4. Results and discussion

4. 4. 1. Evaluation of AFM sample preparation methods

Size analysis of nanoparticles by AFM requires a smooth substrate and good dispersion of the particles on the substrate to the extent of individual particle separation. Four different AFM sample preparation methods were evaluated for their ability to provide individual separation of CNCs and low substrate roughness. The preparation methods were air drying of a small droplet of CNC suspension on untreated, freshly cleaved mica, spin coating of CNCs onto untreated, freshly cleaved mica, spin coating of CNCs onto PSS-treated mica, and spin coating of CNCs onto PDDA-treated mica. The RMS surface roughness values of the three different substrates for 1 μm by 1 μm areas were 0.075±0.01 nm, 0.067±0.01 nm, and 0.082±0.02 nm for the untreated, PSS-treated, and PDDA-treated mica, respectively. Our value for the untreated mica (0.075 nm) was in good agreement with values reported in the literature (e.g. 0.054 nm).[25] In terms of surface roughness, all three substrates were comparable. In other words, treatment of the freshly cleaved mica with PSS or PDDA had no significant effect on the substrate's surface roughness.

Figure 4.1 compares AFM amplitude images of samples prepared by the different sample preparation methods. The air-dried sample (Figure 4.1-a) showed a uniform particle distribution but also many clusters and CNC aggregates. A muscovite mica surface in contact with aqueous media is known to have negatively charged groups.[26] These groups will exert repulsive electrostatic forces upon CNCs, because CNCs prepared with sulfuric acid carry negatively charged sulfate groups.[4, 27-28] As a result, CNCs on freshly cleaved mica will remain in suspension until the liquid evaporates rather than adsorb from suspension onto the substrate. Drying of the sample was done in a fume hood and, thus, probably occurred fairly rapidly. The rapid evaporation of water may have resulted in an uncontrolled deposition of CNCs onto the substrate, which may be the reason for the observed piles and clusters.

The spin-coated sample on untreated mica (Figure 4.1-b) exhibited large, isolated CNC agglomerates. The agglomerates were probably the remainders after drying of separate small droplets possibly formed by substrate dewetting. The spin-coated sample on PSS-treated mica (Figure 4.1-c) showed a mixture of individual CNCs and small CNC aggregates. The sample contained fewer particles per unit area than the air-dried sample. PSS is a negatively charged polyelectrolyte. The aggregates found in this sample are probably a result of similar unfavorable particle–substrate interactions as present in the samples on untreated mica. The spin-coated sample on PDDA-treated mica (Figure 4.1-d) exhibited in a uniform distribution of individual CNCs and very few aggregates. PDDA is a positively charged polyelectrolyte. The PDDA-treated mica surface will exert attractive electrostatic forces upon the CNCs and, thus, cause adsorption of individual CNCs from suspension onto the mica substrate. Comparison of the AFM images for the different sample preparation methods made evident that a positive substrate surface charge is advantageous for individual separation of H_2SO_4-hydrolyzed CNCs on the substrate.

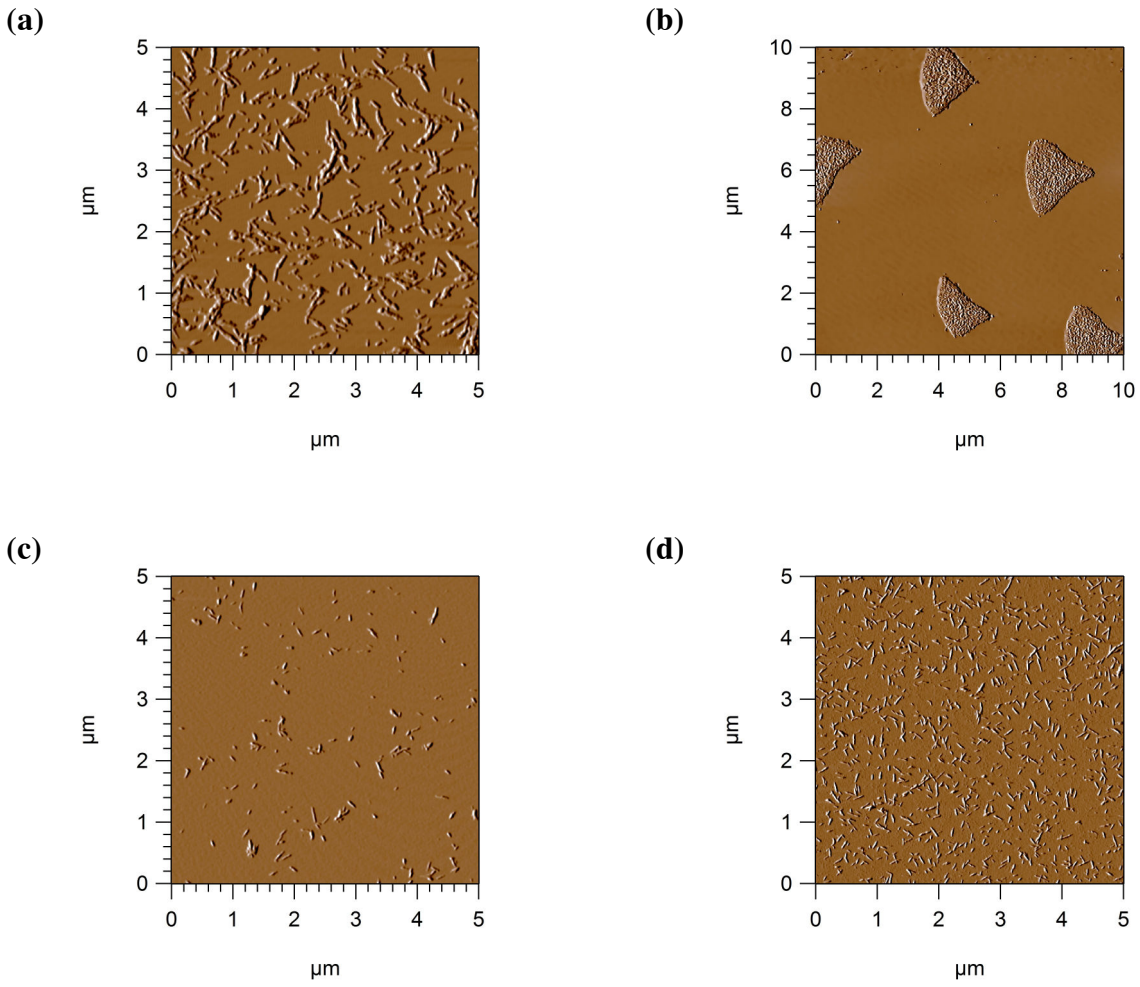

Figure 4.1. AFM amplitude images of CNCs deposited by different methods: (a) air drying on freshly cleaved mica, (b) spin coating onto freshly cleaved mica, (c) spin coating onto PSS-treated mica, (d) spin coating onto PDDA-treated mica.

This finding is in agreement with the findings of Kontturi et al.,[29] who investigated dispersions of spin coated CNCs on silica, titania, and amorphous cellulose substrates. The authors observed that the titania substrate, being positively charged, produced superior CNC dispersion compared with the other two substrates. The RMS surface roughness of the titania substrate was reported as 0.226 nm for a 5 µm × 5 µm area. Even after taking into account the larger scan area used, the value is much larger than the roughness of the PDDA-treated mica (0.082 nm) used here. Thus,

polycation-treated mica may be a better substrate for AFM size measurements of H_2SO_4-hydrolyzed CNCs than titania.

4. 4. 2. AFM-based length, width, and thickness distributions

AFM height images from three of the four sample preparation methods, namely air drying on untreated mica, spin coating onto PSS-treated mica, and spin coating onto PDDA-treated mica, were analyzed in terms of particle length, width, and thickness distributions. Although they gave inferior particle separation, we included the former two methods in the analysis to assess the effect of particle aggregation on the measured dimensions. The images from the fourth method, spin coating onto untreated mica, did not exhibit sufficient particle separation for particle size analysis. Figure 4.2 shows AFM length histograms of CNCs for the three examined AFM sample preparation methods before and after correction of the data for tip broadening. All sample preparation methods gave broad, positively skewed length distributions in accordance with previous TEM- and AFM-based literature reports.[4, 19, 22] Both the uncorrected and tip broadening-corrected data were well described by log normal distribution functions (dashed lines in Figure 4.2).

Table 4.2 lists the means, medians, and standard deviations of both the uncorrected and tip broadening-corrected length data for each sample preparation method. A comparison of the statistical measures for the three sample preparation methods revealed that both the mean and median length values and the widths of the distributions, as indicated by the magnitudes of the standard deviations, were strongly affected by the sample's degree of dispersion of the particles. The corrected mean particle length of the air-dried sample on untreated mica, exhibiting the lowest degree of dispersion, was nearly 60% and the standard deviation nearly 40% larger than that of the spin-coated sample on PDDA-treated mica. The spin coated sample on PSS-treated mica, having an intermediate degree of particle dispersion, showed only slightly larger mean and median length values than the spin-coated sample on PDDA-treated mica, indicating that particle aggregation in this sample was mostly lateral.

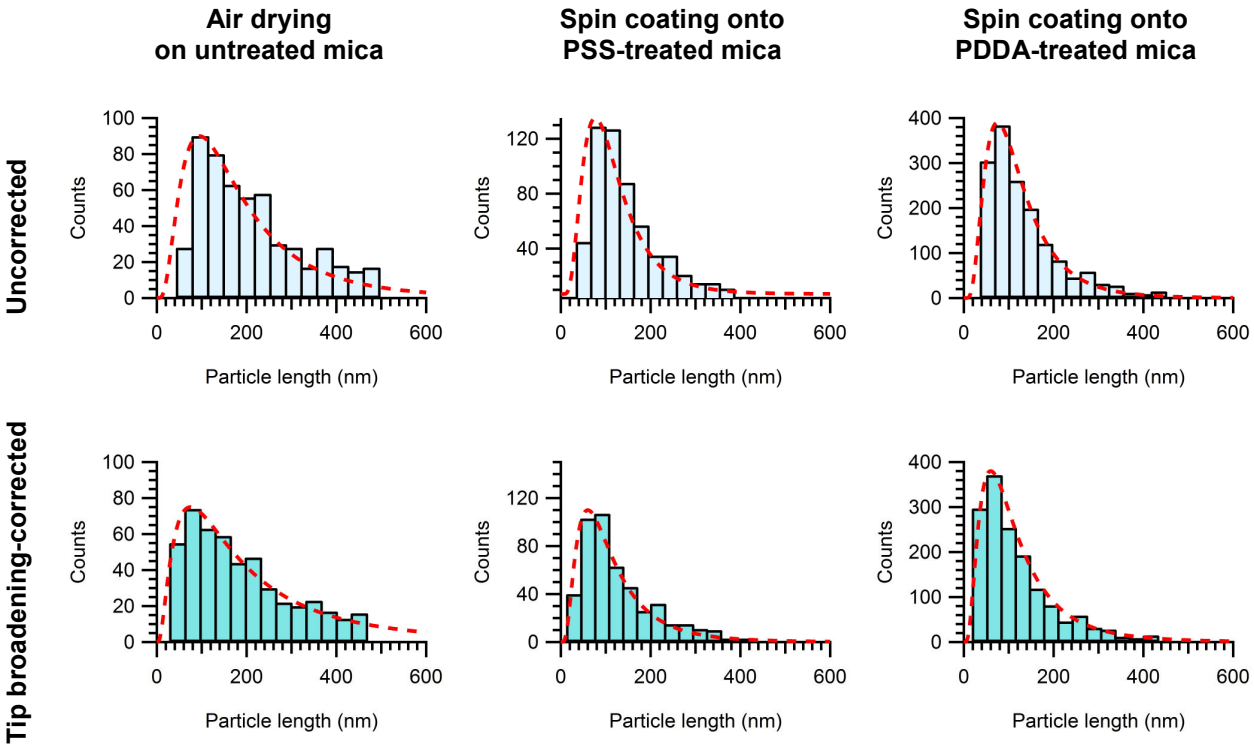

Figure 4.2. Uncorrected and tip broadening-corrected AFM length histograms of CNCs for three AFM sample preparation methods. The dashed lines represent fits of the data to a log normal distribution function.

Table 4.2. Statistical measures of both the uncorrected and tip broadening-corrected CNC length data from AFM image analysis for three different AFM sample preparation methods.

AFM sample preparation method	Uncorrected length (nm)			Corrected length (nm)		
	Mean ± SE	Median ± SE	SD	Mean ± SE	Median ± SE	SD
Air-drying on untreated mica	208.4±4.9	181.9±6.1	111.5	183.5±5.1	157.2±6.4	112.1
Spin coating onto PSS-treated mica	149.6±3.4	123.5±4.2	81.7	125.7±3.7	100.0±4.7	81.6
Spin coating onto PDDA-treated mica	132.6±2.1	106.7±2.6	81.4	115.6±2.1	89.5±2.6	82.0

Considering that the spin-coated sample on PDDA-treated mica exhibited the best particle dispersion and fewest particle aggregates, the CNC length values for this sample should be considered the most accurate. The corrected mean particle length of the spin-coated sample on PDDA-treated mica (115.6 nm) was within the range of TEM- and AFM-based length values reported in the literature for similar kinds of materials (105-147 nm).[19, 22] However, given the skewness of the length distribution, the median length (89.5 nm) is a better indicator for the central tendency of the distribution because it is less affected by the length extremes than the mean length.

Figure 4.3 shows the width histograms of CNCs for the three examined AFM sample preparation methods before and after correction of the data for tip broadening. Except for one case, both the uncorrected and tip broadening-corrected width distributions were positively skewed and well described by log normal distribution functions (dashed lines in Figure 4.3). The uncorrected width distribution for the spin-coated sample on PSS-treated mica exhibited a slight negative skewness (-0.33). As could be expected, the particle width data were more strongly affected by tip broadening than the length data. Correction of the width data for tip broadening resulted in an increase in skewness of the width distributions for all three sample preparation methods, which was most apparent in the spin-coated sample on PSS-treated mica, showing a change from negative to positive distribution skewness.

Table 4.3 lists the means, medians, and standard deviations of both the uncorrected and tip broadening-corrected width data for each sample preparation method. The corrected mean and median widths were on average 53% smaller than the uncorrected ones whereas the corrected mean and median lengths were on average only 15% smaller than the uncorrected ones. The particle width data were also more strongly affected by the degree of dispersion of the particles than the length data. The corrected mean particle width of the air-dried sample on untreated mica was more than twice that and the standard deviation was three times as large as that of the spin-coated sample on PDDA-treated mica. The corrected mean particle width of the spin-coated sample on PDDA-treated mica (13.3 nm) was within the range of TEM-based width values reported in the literature for similar kinds of materials (8.5-27 nm).[17, 19]

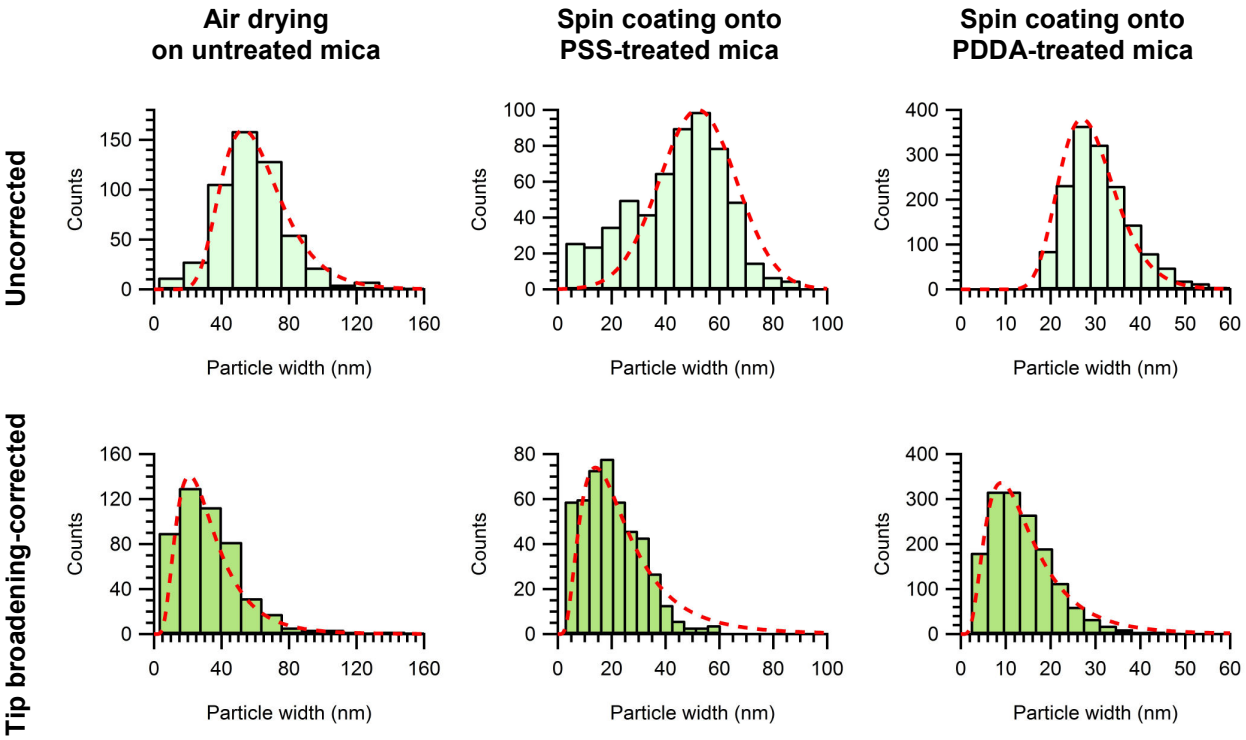

Figure 4.3. Uncorrected and tip broadening-corrected AFM width histograms of CNCs for three AFM sample preparation methods. The dashed lines represent fits of the data to a log normal distribution function.

Table 4.3. Statistical measures of both the uncorrected and tip broadening-corrected CNC width data from AFM image analysis for three different AFM sample preparation methods.

AFM sample preparation method	Uncorrected width (nm)			Corrected width (nm)		
	Mean ± SE	Median ± SE	SD	Mean ± SE	Median ± SE	SD
Air-drying on untreated mica	58.3±1.0	56.3±1.2	22.4	32.3±1.0	29.0±1.2	21.1
Spin coating onto PSS-treated mica	43.9±0.7	46.8±0.9	17.7	19.7±0.5	18.1±0.6	11.1
Spin coating onto PDDA-treated mica	30.7±0.2	29.6±0.2	7.2	13.3±0.2	12.1±0.2	7.0

Figure 4.4 shows the thickness histograms of CNCs for the three examined AFM sample preparation methods. AFM thickness measurements are not affected by tip broadening and therefore do not require correction of the data. The fact that the thickness distributions were much less skewed (0.6 on average) than the length and width distributions (1.1 on average) indicated that the thickness data were more normally distributed. The thickness distribution of the air-dried sample exhibited a higher skewness (0.84) than the thickness distributions of the other two samples (0.49 on average). The higher skewness of the air-dried sample was likely due to the presence of particle stacks with a greater height than individual particles.

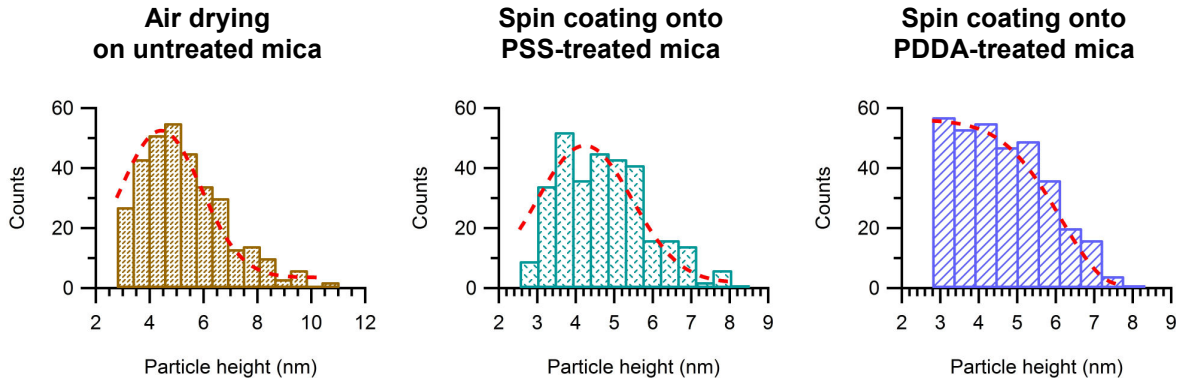

Figure 4.4. AFM thickness histograms of CNCs for three AFM sample preparation methods. The dashed lines represent fits of the data to a normal distribution function.

The means, medians, and standard deviations of thickness data for each sample preparation method are listed in Table 4.4. The thickness data showed much less variability than the length and width data as evident from the lower coefficients of variation for these data (Table 4.5). The larger mean and median particle thickness of the air-dried sample compared to the spin-coated sample on PDDA-treated mica was probably due to the particle stacking observed in the AFM image (Figure 4.1-a). The fact that the mean and median particle thickness of the spin coated sample on PSS-treated mica was lower than that of the air-dried sample indicated that the extent of particle stacking in this sample was smaller than in the air-dried sample. The mean particle thickness of the spin-coated sample on PDDA-treated mica (4.27 nm) was in good agreement

with AFM-based thickness values reported in the literature for wood pulp-derived CNCs (4.5-5.0 nm).[22] A comparison of the median particle width (12.1 nm) and thickness (4.3 nm) of the spin coated sample on PDDA-treated mica confirmed an anisodiametric cross section for the CNCs. Our width-to-thickness ratios of about 2.8 for the medians and 3.1 for the means were smaller than that reported by Mukherjee and Woods of 4.5 for plant-based CNCs.[17]

Table 4.4. Mean values and standard deviations of CNC thickness data from AFM image analysis for three different AFM sample preparation methods.

AFM sample preparation method	Thickness (nm)		
	Mean ± SE	Median ± SE	SD
Air drying on untreated mica	5.97±0.09	4.71±0.11	1.55
Spin coating onto PSS-treated mica	4.49±0.25	4.43±0.32	1.16
Spin coating onto PDDA-treated mica	4.33±0.06	4.27±0.08	1.18

Table 4.5. Coefficient of variance values for the corrected length, width, and the thickness data.

AFM sample preparation method	Coefficient of Variance		
	Corrected Length	Corrected Width	Thickness
Air drying on untreated mica	0.61	0.65	0.26
Spin coating onto PSS-treated mica	0.65	0.56	0.26
Spin coating onto PDDA-treated mica	0.71	0.53	0.27

4. 4. 3. DLS-based length and diameter

For comparison, the mean particle length and diameter of the CNCs were also determined by a combination of DLS and DDLS with a multi-angle DLS instrument. DLS measures the translational diffusion coefficient, D_T, of the particles and DDLS measures the rotational diffusion coefficient, D_R and also D_T. Several equations are available that relate D_T and D_R to the length, L, and diameter, d, of cylindrical particles. The equations by Broersma[30-32] for rigid, non-interacting cylinders at infinite dilution are valid for rods with an aspect ratio (L/d) greater than 4.6, which applies to CNCs. According to Broersma, D_T is related to L and d by

$$D_T = \frac{k_b T}{3\pi\eta L} \times \left(\ln\left(\frac{2L}{d}\right) - \frac{1}{2}\left(\gamma_{\parallel} + \gamma_{\perp}\right) \right) \qquad [4.3]$$

where

$$\gamma_{\parallel} = 0.807 + \frac{0.15}{\left[\ln\left(\frac{2L}{d}\right)\right]} + \frac{13.5}{\left[\ln\left(\frac{2L}{d}\right)\right]^2} - \frac{37}{\left[\ln\left(\frac{2L}{d}\right)\right]^3} + \frac{22}{\left[\ln\left(\frac{2L}{d}\right)\right]^4}$$

and

$$\gamma_{\perp} = -0.193 + \frac{0.15}{\left[\ln\left(\frac{2L}{d}\right)\right]} + \frac{8.1}{\left[\ln\left(\frac{2L}{d}\right)\right]^2} - \frac{18}{\left[\ln\left(\frac{2L}{d}\right)\right]^3} + \frac{9}{\left[\ln\left(\frac{2L}{d}\right)\right]^4}$$

and D_R by

$$D_R = \frac{3k_b T}{\pi\eta L^3} \times \left(\ln\left(\frac{2L}{d}\right) - \delta_{\perp} \right) \qquad [4.4]$$

where

$$\delta_{\perp} = 1.14 + \frac{0.20}{\left[\ln\left(\frac{2L}{d}\right)\right]} + \frac{16}{\left[\ln\left(\frac{2L}{d}\right)\right]^2} - \frac{63}{\left[\ln\left(\frac{2L}{d}\right)\right]^3} + \frac{62}{\left[\ln\left(\frac{2L}{d}\right)\right]^4}$$

In equations 4.3 and 4.4, k_b is the Boltzmann constant, T is the absolute temperature, and η is the solvent viscosity.

D_T and D_R were measured at different CNC concentrations. Figure 4.5 shows D_T and D_R as functions of CNC concentration. The D_T and D_R values were determined from the slopes and the intercept, respectively, of linear fits of decay rate vs. scattering vector plots (data not shown) from the DLS and the DDLS data.

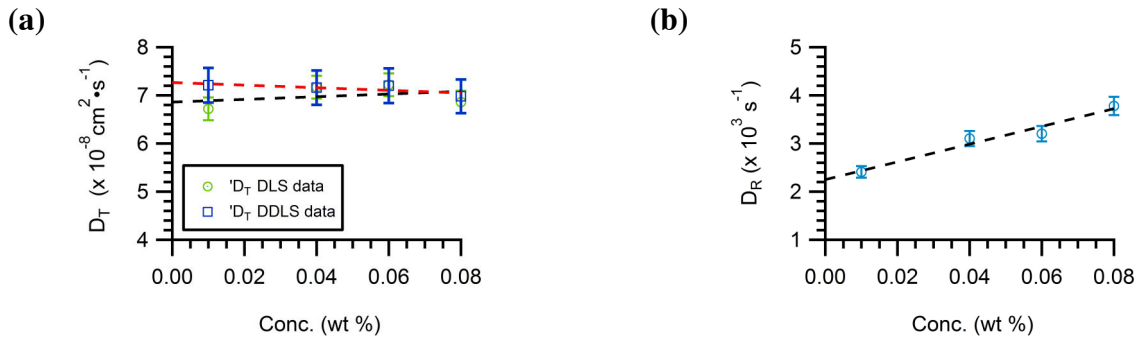

Figure 4.5. (a) Translational (D_T) and (b) rotational (D_R) diffusion coefficients, determined by DLS and DDLS, respectively, as functions of CNC concentration.

The infinite dilution D_T and D_R for CNCs, determined by extrapolation of the DLS and DDLS data in Figure 4.5 to 0 wt %, were 6.95×10^{-8} cm^2/s and 2250 s^{-1}, respectively. These values are slightly larger than the values reported in the literature for cotton-derived CNCs (5.5×10^{-8} cm^2/s and 552 s^{-1}).[14] The values for L and d calculated from the infinite dilution D_T and D_R with equations 4.3 and 4.4 were 136.9 and 18.8 nm, respectively. The values of D_T, D_R, L and d were also calculated by using only DDLS data, for comparison purposes. The value of D_T (at infinite dilution) based on the DDLS data was estimated as 7.26×10^{-8} cm^2/s and 2250 s^{-1} for D_R, within these values L and d were estimated as 141.0 and 16.8 nm, respectively. The DLS-based length value was 18% larger and the diameter 41% larger than the AFM-based mean length (115.6 nm) and width (13.3 nm), respectively. In previous studies, DLS has been shown to give larger particle dimensions than AFM.[33-34] The discrepancies between DLS and AFM-based particle dimensions may have several reasons. In some cases, they may be due to swelling or aggregation of the particles in suspension. Furthermore, as mentioned in the introduction, the scattering intensity-based size distributions measured by DLS are weighted toward larger particles. AFM-based size distributions are number distributions, which weigh each particle equally and

therefore have smaller mean and median values. In addition, DLS-based dimensions include in part or in whole the hydration shell of the particle. DLS size measurements are based on the relation between the particle's dimensions, diffusion coefficient, and scattered intensity. For charged particles, such as CNCs, diffusion is slowed and the diffusion coefficient lowered by the electric double layer, the thickness of which depends on the ionic strength.[35] Thus, DLS overestimates the true particle dimensions and the magnitude of this overestimation depends on the particle surface charge and ionic strength of the suspension.

In the present case, particle swelling or aggregation are unlikely reasons for the discrepancies between the AFM- and DLS-based dimensions because only the topmost layer of crystalline cellulose is structurally affected by surrounding water molecules[36] and because the DLS samples had been sonicated immediately prior to the measurements. Therefore, the discrepancies were attributed to the difference in the nature of the size distributions (number vs. intensity) and the electric double layer and solvation shell of the CNCs.

4. 4. 4. Equivalent spherical hydrodynamic diameter

The equivalent spherical hydrodynamic diameter of a particle is the diameter of a sphere that has the same translational diffusion coefficient as the analyzed particle. Because CNCs are non-spherical in shape, the equivalent spherical hydrodynamic diameter does not directly relate to the true particle dimensions. However, because equivalent spherical hydrodynamic diameters are more readily determined than AFM- or TEM-based dimensions, it is desirable to establish a correlation between them. The equivalent spherical hydrodynamic diameter of CNCs was measured with a DLS-based particle size analyzer. For determination of the concentration range in which the measured values were independent of concentration, experiments were performed at different particle concentrations.

Figure 4.6-a shows the mean intensity diameter as a function of CNC concentration. The mean intensity diameter was independent of concentration between 0.002 and 0.08 wt %. Figure 4.6-b shows a typical intensity distribution. Like the number distributions obtained by AFM, the intensity distributions were positively skewed and well described by log normal distribution

functions. The measured mean intensity diameter was 142.7±0.3 nm , which was slightly larger than the length obtained with the Broersma equations on the multi-angle DLS instrument (136.9 nm). According to the calculations of Jennings and Parslow,[37] the translational diffusion-based equivalent spherical diameter of a prolate particle with an axial ratio greater than ~ 4 should be less than half the true length of the particle. The fact that the equivalent spherical diameter measured with the particle size analyzer was larger even than the overestimated length obtained with the multi-angle DLS instrument indicated that the two instruments gave inconsistent results. The measured equivalent spherical diameter was much larger than the mean (115.6 nm) and median (89.5 nm) length determined by AFM.

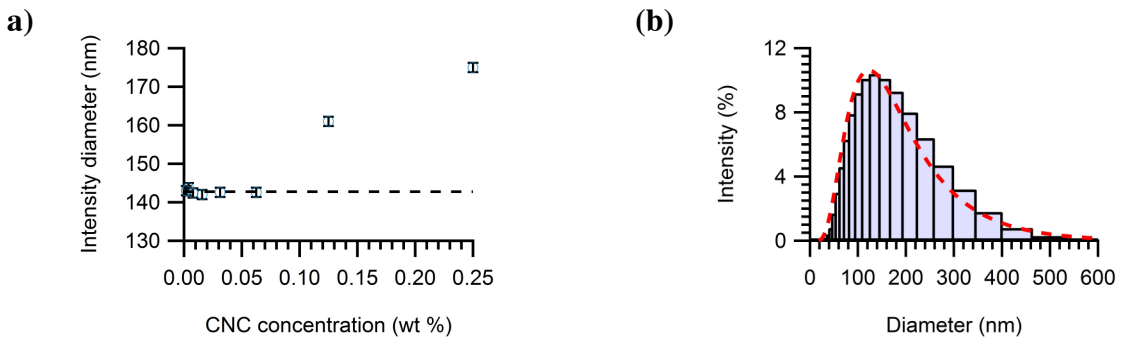

Figure 4.6. Characterization of CNCs with a DLS-based particle size analyzer: (a) mean intensity diameter as a function of CNC concentration, (b) typical intensity distribution.

4. 5. Conclusions

The objectives of this study were to determine from AFM data the distributions of particle length, width, and thickness in a CNC sample and to correlate the obtained mean dimensions with the length, diameter, and equivalent spherical hydrodynamic diameter obtained from DLS and DDLS measurements. In light of the above results, the following conclusions can be drawn for CNCs derived from wood pulp by H_2SO_4 hydrolysis. AFM-based length, width, and thickness values depend strongly on the sample preparation method and the extent of particle separation on the substrate. Sample preparation by spin coating onto PDDA-treated mica produces samples

with individual separation of the particles and a low substrate roughness, well suited for AFM particle analysis. Untreated, freshly cleaved mica is an unfavorable substrate because it induces particle aggregation. CNCs have positively skewed, log normal-type length, width, and thickness distributions and an anisodiametric shape with a mean length of 115.6 nm, mean width of 13.3 nm, and mean thickness of 4.3 nm. DLS-based methods overestimate the length and diameter of CNCs. The equivalent spherical hydrodynamic diameter does not correspond to the sample's mean particle length but may serve as an upper estimate.

4. 6. Acknowledgements

This project was supported by the National Research Initiative of the USDA Cooperative State Research, Education and Extension Service, grant number 2005-35504-16088, and by the National Science Foundation under grant numbers CHE-0724126 and DMR-0907567. The authors also gratefully acknowledge the generous scholarship support for F. N. by the Mexican Secretariat of Public Education (SEP) through its Professional Development for Teachers Program (PROMEP). Furthermore, additional support from OMNOVA, Inc. and Tembec, Inc. are also acknowledged.

4. 7. References

1. Revol, J. F.; Bradford, H.; Giasson, J.; Marchessault, R. H.; Gray, D. G. Helicoidal self-ordering of cellulose microfibrils in aqueous suspension. *International Journal of Biological Macromolecules* **1992,** 14, 170–172.
2. Gray, D. G. Chiral nematic ordering of polysaccharides. *Carbohydrate Polymers* **1994,** 25, 277–284.
3. Revol, J. F.; Godbout, L.; Dong, X. M.; Gray, D. G.; Chanzy, H.; Maret, G. Chiral nematic suspensions of cellulose crystallites; phase separation and magnetic field orientation. *Liquid Crystals* **1994,** 16, 127–134.
4. Dong, X. M.; Revol, J.-F.; Gray, D. G. Effect of microcrystallite preparation conditions on the formation of colloid crystals of cellulose. *Cellulose* **1998,** 5, 19–32.

5. Araki, J.; Wada, M.; Kuga, S.; Okano, T. Birefringent glassy phase of a cellulose microcrystal suspension. *Langmuir* **2000,** 16, 2413–2415.
6. Yi, J.; Xu, Q. X.; Zhang, X. F.; Zhang, H. L. Chiral-nematic self-ordering of rodlike cellulose nanocrystals grafted with poly(styrene) in both thermotropic and lyotropic states. *Polymer* **2008,** 49, 4406–4412.
7. Hirai, A.; Inui, O.; Horii, F.; Tsuji, M. Phase Separation Behavior in Aqueous Suspensions of Bacterial Cellulose Nanocrystals Prepared by Sulfuric Acid Treatment. *Langmuir* **2009,** 25, 497–502.
8. Elazzouzi-Hafraoui, S.; Putaux, J. L.; Heux, L. Self-assembling and Chiral Nematic Properties of Organophilic Cellulose Nanocrystals. *Journal of Physical Chemistry B* **2009,** 113, 11069–11075.
9. Favier, V.; Chanzy, H.; Cavaillé, J. Y. Polymer Nanocomposites Reinforced by Cellulose Whiskers. *Macromolecules* **1995,** 28, 6365–6367.
10. Grunert, M.; Winter, W. T. Nanocomposites of cellulose acetate butyrate reinforced with cellulose nanocrystals. *Journal of Polymers and the Environment* **2002,** 10, 27–30.
11. Azizi Samir, M. A. S.; Alloin, F.; Dufresne, A. Review of recent research into cellulosic whiskers, their properties and their application in nanocomposite field. *Biomacromolecules* **2005,** 6, 612–626.
12. Elmabrouk, A.; Wim, T.; Dufresne, A.; Boufi, S. Preparation of Poly(styrene-co-hexylacrylate)/Cellulose Whiskers Nanocomposites via Miniemulsion Polymerization. *Journal of Applied Polymer Science* **2009,** 114, 2946–2955.
13. De Souza Lima, M. M.; Borsali, R. Rodlike cellulose microcrystals: Structure, properties, and applications. *Macromolecular Rapid Communications* **2004,** 25, 771–787.
14. De Souza Lima, M. M.; Wong, J. T.; Paillet, M.; Borsali, R.; Pecora, R. Translational and rotational dynamics of rodlike cellulose whiskers. *Langmuir* **2003,** 19, 24–29.
15. Dong, X. M.; Gray, D. G. Effect of counterions on ordered phase formation in suspensions of charged rodlike cellulose crystallites. *Langmuir* **1997,** 13, 2404–2409.
16. Bonini, C.; Heux, L.; Cavaillé, J. Y.; Lindner, P.; Dewhurst, C.; Terech, P. Rodlike cellulose whiskers coated with surfactant: A small-angle neutron scattering characterization. *Langmuir* **2002,** 18, 3311–3314.

17. Mukherjee, S. M.; Woods, H. J. X-ray and electron microscope studies of the degradation of cellulose by sulphuric acid. *Biochimica et biophysica acta* **1953,** 10, 499–511.
18. Terech, P.; Chazeau, L.; Cavaillé, J. Y. A Small-Angle Scattering Study of Cellulose Whiskers in Aqueous Suspensions. *Macromolecules* **1999,** 32, 1872–1875.
19. Elazzouzi-Hafraoui, S.; Nishiyama, Y.; Putaux, J. L.; Heux, L.; Dubreuil, F.; Rochas, C. The shape and size distribution of crystalline nanoparticles prepared by acid hydrolysis of native cellulose. *Biomacromolecules* **2008,** 9, 57–65.
20. Araki, J.; Wada, M.; Kuga, S.; Okano, T. Flow properties of microcrystalline cellulose suspension prepared by acid treatment of native cellulose. *Colloids and Surfaces, A: Physicochemical and Engineering Aspects* **1998,** 142, 75–82.
21. Kvien, I.; Tanem, B. S.; Oksman, K. Characterization of cellulose whiskers and their nanocomposites by atomic force and electron microscopy. *Biomacromolecules* **2005,** 6, 3160–3165.
22. Beck-Candanedo, S.; Roman, M.; Gray, D. G. Effect of reaction conditions on the properties and behavior of wood cellulose nanocrystal suspensions. *Biomacromolecules* **2005,** 6, 1048–1054.
23. Hasani, M.; Cranston, E. D.; Westman, G.; Gray, D. G. Cationic surface functionalization of cellulose nanocrystals. *Soft Matter* **2008,** 4, 2238–2244.
24. Chapter 3.
25. Simpson, G. J.; Sedin, D. L.; Rowlen, K. L. Surface roughness by contact versus tapping mode atomic force microscopy. *Langmuir* **1999,** 15, 1429–1434.
26. Scales, P. J.; Grieser, F.; Healy, T. W. Electrokinetics of the Muscovite Mica Aqueous-Solution Interface. *Langmuir* **1990,** 6, 582–589.
27. Rånby, B. G. Aqueous colloidal solutions of cellulose micelles. *Acta Chemica Scandinavica* **1949,** 3, 649–650.
28. Marchessault, R. H.; Morehead, F. F.; Koch, M. J. Hydrodynamic properties of neutral suspensions of cellulose crystallites as related to size and shape. *Journal of Colloid Science* **1961,** 16, 327–344.
29. Kontturi, E.; Johansson, L. S.; Kontturi, K. S.; Ahonen, P.; Thüne, P. C.; Laine, J. Cellulose nanocrystal submonolayers by spin coating. *Langmuir* **2007,** 23, 9674–9680.

30. Broersma, S. Rotational diffusion constant of a cylindrical particle. *Journal of Chemical Physics* **1960,** 32, 1626–31.
31. Broersma, S. Viscous force constant for a closed cylinder. *Journal of Chemical Physics* **1960,** 32, 1632–5.
32. Broersma, S. Viscous force and torque constants for a cylinder. *Journal of Chemical Physics* **1981,** 74, 6989–6990.
33. Hoo, C. M.; Starostin, N.; West, P.; Mecartney, M. L. A comparison of atomic force microscopy (AFM) and dynamic light scattering (DLS) methods to characterize nanoparticle size distributions. *Journal of Nanoparticle Research* **2008,** 10, 89-96.
34. Zanetti-Ramos, B. G.; Fritzen-Garcia, M. B.; Cristian, S.; Andr, A. P. B.; Soldi, V.; Borsali, R.; Creczynski-Pasa, T. B. Dynamic light scattering and atomic force microscopy techniques for size determination of polyurethane nanoparticles. *Materials Science & Engineering C-Biomimetic and Supramolecular Systems* **2009,** 29, 638-640.
35. Schumacher, G. A.; Vandeven, T. G. M. Brownian-Motion of Charged Colloidal Particles Surrounded by Electric Double-Layers. *Faraday Discussions* **1987,** 83, 75-+.
36. Heiner, A. P.; Teleman, O. Interface between monoclinic crystalline cellulose and water: Breakdown of the odd/even duplicity. *Langmuir* **1997,** 13, 511-518.
37. Jennings, B. R.; Parslow, K. Particle Size Measurement - The Equivalent Spherical Diameter. *Proceedings of the Royal Society of London, Series A: Mathematical and Physical Sciences* **1988,** 419, 137-149.

Chapter 5

Effects of Cleaning Procedures on the Surface Properties of Glass Substrates

Effects of cleaning procedures on the surface properties of glass substrates

Fernando Navarro and Maren Roman

Macromolecules and Interfaces Institute and Department of Wood Science and Forest Products, 230 Cheatam Hall, Virginia Polytechnic Institute and State University, Blacksburg, Virginia, 24061, United States of America.

5.1. Abstract

The purpose of this study was to determine the effects of cleaning procedures on the surface properties of glass substrates. Soda–lime–silica glass slides were cleaned by one of three methods and the properties of the cleaned glass slides were analyzed by X-ray photoelectron spectroscopy, contact angle measurements, atomic force microscopy, streaming potential measurements, and scanning Kelvin probe microscopy. Cleaning with a detergent solution (Alconox) resulted in an aluminum-enriched surface layer with reduced modifier content, a strongly increased negative ζ-potential, an increased surface polarity and surface free energy, and patches of positive surface charge in the dry state. Cleaning with aqua regia resulted in a glass surface layer completely devoid of modifiers and aluminum, an altered adventitious carbon composition (no carbonyl or acetal groups), a reduced surface polarity and surface roughness, an increased negative ζ-potential, and a honeycomb pattern of positive surface charge in the dry state. Cleaning with an organic solvent mixture (ethanol/chloroform) resulted in an aluminum-enriched surface layer with reduced modifier content, a reduced surface polarity and surface free energy, an increased surface roughness, and a slightly increased negative ζ-potential. The study shows that cleaning procedures for glass slides need to be chosen on the basis of the desired surface properties.

Keywords: *cleaning solutions, soda–lime–silica glass, surface properties, AFM, XPS.*

5.2. Introduction

Glass is a fascinating material with a long history of human use. It is mainly composed of silica with minor amounts of alkali, alkaline earth, and other metal oxides. On the basis of the nature and proportions of the oxides used in the glass formulation, several types of glasses can be distinguished. Common glass types include borosilicate, aluminosilicate, and soda–lime–silica (SLS) glasses.[1] SLS glasses are extensively used materials with typical compositions of 71–73% SiO_2, 13–15.5% Na_2O, 0–1% K_2O, 6.5–12% CaO, 2–4.5% MgO, and 0–2% Al_2O_3.[1] Because of their low cost and availability, SLS glasses are widely used not only in the construction and automobile industries, but also in many scientific and technological applications, such as optoelectronic devices,[2-4] display devices,[5-6] high performance glazing,[7-9] and bioactive materials for bone formation.[10]

Glasses have very complex surface chemistries. Chemical processes at glass–water interfaces involve ion exchange reactions, dissolution processes, and chemical conversion processes. The successful application and performance of glass-based devices depend strongly on the chemistry of the glass surface.[11-13] The surface chemistry and structure of SLS glasses have been a topic of interest in many scientific studies. X-ray photoelectron spectroscopy (XPS) has been one of the techniques that have provided the most insight into the chemical structure of glass surfaces.[8, 10, 14-16] SLS glass-based substrates are commonly used substrates in many scientific disciplines. Most scientific applications require clean glass surfaces. Typical cleaning methods include the use of strong alkaline or acid reagents, organic solvents, or strong oxidizing agents. The cleaning chemicals can alter the surface properties of the glass substrates through processes, such as etching and adsorption.

The objective of this study was to determine the effects of different cleaning procedures on the surface properties of glass substrates. The study focuses on SLS glass and examines three different cleaned procedures, namely a detergent-based, an acid-based, and an organic solvent-based procedure. “As received” and cleaned microscope glass slides were characterized in terms of surface chemical composition, surface free energy, surface roughness, ζ-potential, and charge

distribution in the dry state. Each cleaning procedure had different effects on the different surface properties analyzed.

5.3. Experimental section

5.3.1. Materials and cleaning procedures

The glass slides used in this study were 3 in. x 1 in. SLS glass microscope slides (T & Q Industries, Pearl Brand, "pre-cleaned"). The glass slides were subjected to one of the following cleaning procedures:

"As received" cleaning procedure. The glass slides were briefly placed in a stream of nitrogen for removal of any loose particles from their surface and stored in a slide storage box until use.

Soap cleaning procedure. A 4 wt % solution (pH > 9.5) of Alconox in deionized (DI) water (Millipore Direct-Q5, 18.2 MΩ·cm) was degassed for 30 min at 45 ºC in an ultrasonic cleaner (Bransonic, model B3510-DTH) and then poured into a glass staining dish loaded with glass slides. The staining dish was placed into the ultrasonic cleaner and subjected to ultrasound for 10 min at 45 °C. Next, the soap solution in the staining dish was replaced with DI water and the ultrasound treatment was repeated. The slides were washed twice more with DI water and an ultrasound treatment of 5 and 2 min, respectively. Finally, the slides were dried in a stream of nitrogen and stored in a slide storage box until use.

Aqua regia cleaning procedure. A 3:1 mixture by volume of hydrochloric acid (Fisher, 37.4% purity) and nitric acid (Fisher, 69.5% purity) was poured into a glass staining dish loaded with glass slides. The staining dish was covered and left undisturbed for 30 min. Then, the acid mixture was replaced with DI water and the slides were washed three times in an ultrasonic cleaner as described above. Finally, the slides were dried in a stream of nitrogen and stored in a slide storage box until use.

Solvent cleaning procedure. Four glass slides at a time were carefully placed with minimal contact into the extraction tube of a Soxhlet apparatus. A 1:1 mixture by volume of ethanol (Sigma-Aldrich, anhydrous, 200 proof, 99.5+% purity) and chloroform (Fisher, ≥ 99.8% purity) was brought to a boil in the still pot. After four reflux cycles, the glass slides were placed into a glass staining dish and rinsed three times with DI water in an ultrasonic cleaner as described above. Finally, the slides were dried in a stream of nitrogen and stored in a slide storage box.

5.3.2. X-ray photoelectroscopy (XPS)

For XPS analysis, glass slides were cut into 1 cm x 1 cm pieces prior to cleaning. The cleaned and dried glass pieces were stored in polystyrene Petri dishes with their top surfaces marked. Care was taken to analyze the glass surface that was not in contact with the Petri dish. Photoelectron spectra were recorded with a PHI Quantera XPS Scanning X-ray Microprobe (Physical Electronics, Inc.) with an Al-Kα (1486.6 eV) X-ray source and a beam size of 100 μm diameter. Survey spectra were recorded with a pass energy of 280.0 eV, work function of 3.5 eV, take-off angle of 10°, sputter rate of 0.02 nm/s, and resolution step of 1 eV. High-resolution spectra were recorded with a pass energy of 26.0 eV, work function of 3.5 eV, take-off angle of 10°, sputtering rate of 0.02 nm/s, and resolution step of 0.1 eV. The recorded spectra were analyzed with CasaXPS processing software (v2.3.14, Casa Software Ltd.) with the Shirley background correction method and the experimental sensitivity factors specified by the instrument manufacturer. High-resolution spectra were referenced to a C–C/H C_{1s} binding energy of 284.6 eV.[17] Deconvolution of the high-resolution spectra was done with Gaussian/Lorentzian (70/30) peak profiles.

5.3.3. Surface free energy measurement

The surface free energy, γ_S, of the cleaned glass slides was determined from sessile drop contact angles, θ, of four different test liquids with the Owens-Wendt-Rabel-Kaelble method.[18-20] The method is based on the equation

$$\frac{\gamma_L\left(1+\cos\theta\right)}{2\left(\gamma_L^d\right)^{0.5}} = \left(\gamma_S^d\right)^{0.5} + \left(\frac{\gamma_S^p \times \gamma_L^p}{\gamma_L^d}\right)^{0.5} \quad [5.1]$$

where γ_L is the surface tension of the test liquid, γ_L^d and γ_L^p are the dispersive and the polar components of γ_L, respectively. γ_S^d and γ_S^p are the dispersive and the polar components of γ_S, respectively. γ_S^d and γ_S^p are obtained from the intercept and slope, respectively, of a plot of $\gamma_L\left(1+\cos\theta\right)\Big/ 2\left(\gamma_L^d\right)^{0.5}$ against $\left(\gamma_L^p/\gamma_L^d\right)^{0.5}$. γ_S is the sum of γ_S^d and γ_S^p. The four test liquids were DI water, ethylene glycol (Fisher, 99.8+, % purity), dimethyl sulfoxide (Fisher, 99.9 % purity), and n-octane (Acros organics, 99+ % purity). Contact angles were measured in quintuplicate with a video-based contact angle goniometer (First Ten Angstroms, Inc., model FTÅ200).

5.3.4. Atomic force microscopy (AFM)

AFM analysis of the cleaned glass slides was performed with an Asylum Research MFP-3D-Bio atomic force microscope mounted onto an Olympus IX 71 inverted fluorescence microscope. Height and phase images of the slide surfaces were recorded in air in intermittent contact mode (1 Hz, 512 scans, and 512 points/scan) at random locations with Olympus OMCL-AC160TS silicon probes (nominal tip radius <10 nm, spring constant 42 N/m). Reported root-mean-square (RMS) roughness values are means of 100 measurements of a 1 μm x 1 μm surface area.

5.3.5. Streaming and ζ-potential measurement

For streaming potential analysis, glass slides were cut into disks of 1 in. diameter prior to cleaning. The cleaned and dried glass disks were stored in polystyrene Petri dishes with their top surfaces marked. Care was taken to analyze the glass surface that was not in contact with the Petri dish. The streaming potential of the glass disks was measured with a ZetaSpin apparatus (Zetametrix Inc.) by the rotating disk method of Sides et al.[21] Measurements were done at 25 °C in DI water in the absence of electrolyte with a spinning speed of 4000 rpm and a distance of 1

mm between the electrode and the glass surface. Reported streaming potentials are means of ten measurements with three cycles each.

5.3.6. Scanning Kelvin probe microscopy (SKPM)

SKPM analysis of the cleaned glass slides was performed with the MFP-3D-Bio atomic force microscope. Potential images of the slide surfaces were recorded in air at random locations with Olympus OMCL-AC240TM platinum-coated silicon probes (nominal tip radius <25 nm, spring constant 2 N/m), 512 scans at a resolution of 512 points/scan, a scan frequency of 0.5 Hz, a tip-sample distance of 5 nm, and an AC voltage of 3.0 V. Scanning was done in nap mode, a two-pass technique, which for each image line and scan direction involves a regular (no potential applied) line scan in intermittent contact-mode for determination of the height profile followed by a line scan with applied potential and the tip at a fixed distance from the sample surface. Before scanning, the relative humidity in the acoustic enclosure (AEK-5004, Herzan LLC) was reduced to 5% by circulation of the air from the enclosure through a PVC pipe filled with silica gel (Fisher, 6-12 mesh, certified ACS) and back into the enclosure until it had the desired relative humidity. During this process, the relative humidity was monitored with a traceable hygrometer (Model 11-661-18, Control Company). Once the desired relative humidity was reached, the pump was turned off for noise minimization. The relative humidity in the enclosure stayed constant for the duration of image acquisition. Reported RMS potential variation values were measured over a 10 μm x 10 μm area.

5.4. Results and discussion

5.4.1. Surface chemical composition

The effects of the cleaning procedures on the surface chemical composition of the glass slides were analyzed by XPS. Figure 5.1 shows the XPS survey spectra of glass slides subjected to different cleaning procedures. All glass slides gave strong silicon, oxygen, and carbon emission signals. Except for the aqua regia-cleaned slide, the glass slides also gave emission signals for

sodium, calcium, and in some cases magnesium and aluminum. As opposed to the other glass slides, the solvent-cleaned slide also gave a nitrogen emission signal. Table 5.1 lists the relative atomic surface compositions of the glass slides normalized to the silicon content.

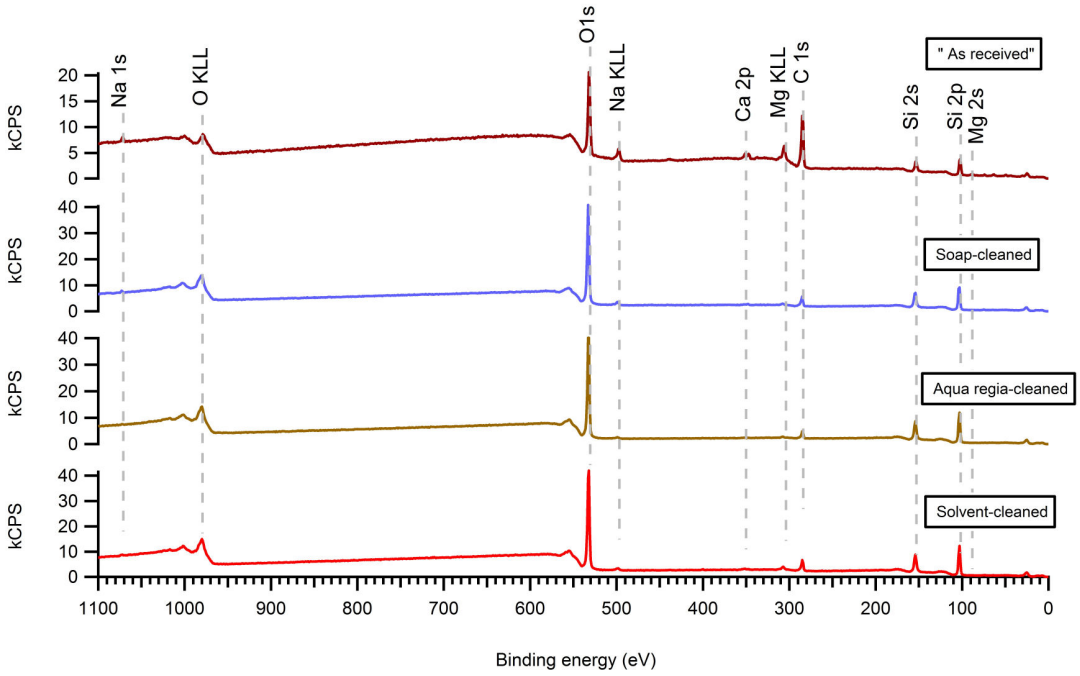

Figure 5.1. Survey photoelectron spectra of glass slides subjected to different cleaning procedures.

Table 5.1. Relative atomic surface composition of glass slides subjected to different cleaning procedures normalized to the Si content.

Sample	C_{1s}	O_{1s}	Si_{2p}	Na_{1s}	Ca_{2p}	Mg_{2s}	Al_{2p}	N_{1s}
"As received"	5.652	2.886	1.000	0.047	0.082	0.033	--	--
Soap-cleaned	0.657	2.672	1.000	0.016	0.012	--	0.029	--
Aqua regia-cleaned	0.400	2.352	1.000	--	--	--	--	--
Solvent-cleaned	0.635	2.309	1.000	0.013	0.012	0.015	0.033	0.021

Silica-based glasses consist of a random network of SiO_4 tetrahedra, forming the matrix. Most glass oxygen atoms are covalently bonded to two silicon atoms (Si–O–Si). These oxygen atoms are called bridging oxygen (BO) atoms. Inclusion of alkali and alkaline earth oxides in the glass formulation introduces alkali and alkaline earth metal ions into the glass structure. These ions are called modifiers because they modify the Si–O network. Alkali and alkaline earth atoms are ionically bonded to silanolate groups ($Si–O^- M^+$ and $Si–O^- M^{2+} {}^-O–Si$). The oxygen atoms in these bonds are called non-bridging oxygen (NBO) atoms. Aluminum atoms can function both as network formers, covalently bonded to three BO atoms, and as modifiers, ionically linked to three NBO atoms.[1, 22]

Glass surfaces contain a large number of silanol groups ($\leq 4.6/nm^2$)[23] formed in the manufacturing process by the reaction of surface siloxane groups with water molecules from the air during cooling of the glass. The silanol groups promote the adsorption of water molecules and organic compounds on glass surfaces. When glass surfaces come in contact with aqueous liquids, ion exchange reactions may take place, which result in replacement of the modifier ions with H^+ followed by migration of the ions into the liquid.[22, 24] Leaching of these ions from the glass surface results in a modifier-depleted leach layer.[22, 25] In addition to ion leaching, aqueous liquids can cause matrix dissolution, which is the release of SiO_2 from the glass surface. In some cases, a protective precipitate layer may be formed on top of the leach layer at the liquid–glass interface, consisting of poorly soluble water–glass reaction products, such as $Al(OH)_3$.[25-26]

The surface of the “as received” glass slide showed a considerable amount of adventitious carbon (see Table 5.1), suggesting that the factory pre-cleaning process left organic residues on the slide surfaces. The extent of organic surface contamination was much reduced in the other three cases, compared to the “as received” slide, and was lowest in the case of the aqua regia-cleaned slide. The relative surface oxygen content of the “as received” glass slide was nearly 2.9 times its silicon content. An O:Si ratio greater than two was expected on account of the surface silanol groups and the silanolate groups associated with the surface Na, Ca, and Mg atoms. In light of the high surface carbon content of the “as received” glass slide, its high surface oxygen content was attributed in part to organic surface contaminants. The surfaces of the soap-, aqua regia-, and solvent-cleaned glass slides showed reduced modifier contents, with respect to the “as received”

slide, indicating the existence of a leach layer. Modifier depletion was most extensive in the case of the aqua regia-cleaned glass slide, which showed a complete lack of Na, Ca, and Mg atoms on the surface. The surfaces of both the soap- and solvent-cleaned glass slides showed a measurable Al content, which was not observed in the case of the "as received" glass slide. The higher Al:Si ratio in these surfaces, with respect to the "as received" slide, indicated the existence of an Al-enriched surface layer. The absence of such layer on the aqua regia-cleaned slide could have two reasons. Water–glass reactions yielding poorly soluble reaction products might not have occurred in the aqua regia cleaning procedure or the reaction products that formed during the procedure were soluble in aqua regia. Whether matrix dissolution had occurred in any of the cleaning procedures could not be inferred from the relative atomic surface compositions of the glass slides. In general, however, matrix dissolution occurs at low pH, where it is due to concomitant dissolution of SiO_2 with acid soluble glass components, and at high pH, where it is due to the cleavage of siloxane bonds by hydroxyl ions.[27] Therefore matrix dissolution probably occurred in the aqua regia and soap cleaning procedures. From the observed difference in surface Al contents, we inferred that matrix dissolution in the aqua regia cleaning procedure included the Al glass component whereas that component did not co-dissolve in the soap cleaning procedure. The lower relative surface oxygen contents of the soap-, aqua regia-, and solvent-cleaned glass slides, with respect to the "as received" slide, were attributed to the decreased amount of organic surface contamination. The origin of the nitrogen atoms on the surface of the solvent-cleaned glass slide is not obvious. The solvents that were used in the solvent cleaning procedure (ethanol and chloroform) did not contain nitrogen. Nitrogen atoms might have adsorbed onto the surface of the slide upon drying of the slide in a nitrogen stream. If that were the case, however, it would be unclear why nitrogen adsorption was not observed in the other three cleaning procedures, which also involved placement of the glass slides into a nitrogen stream.

The Si_{2p}, C_{1s}, and O_{1s} emission were analyzed in high resolution for information about the chemical environments of these atoms. Figure 5.2 shows Si_{2p} core level spectra for glass slides subjected to different cleaning procedure.

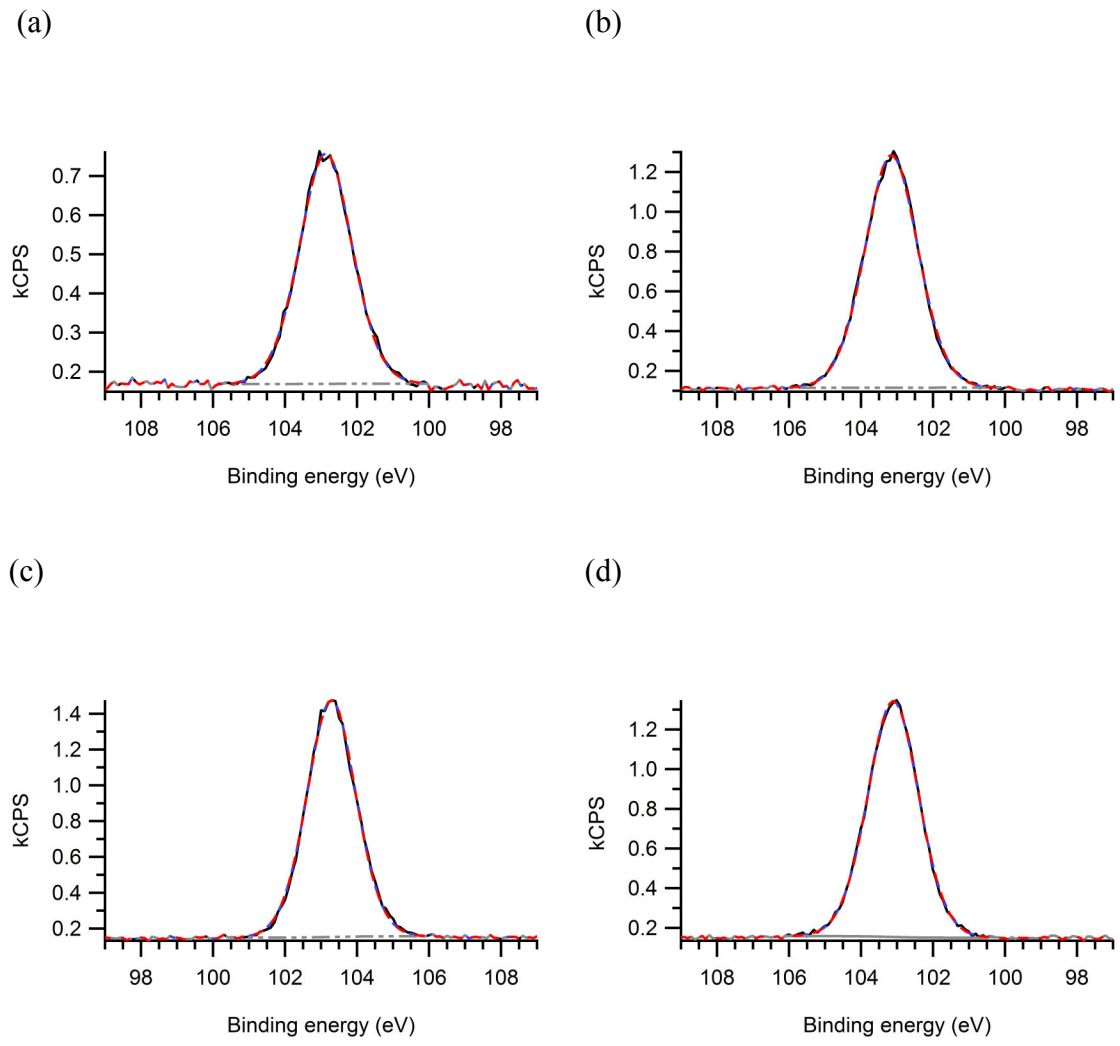

Figure 5.2. High-resolution Si_{2p} photoelectron spectra of glass slides subjected to different cleaning procedures: (a) "as received", (b) soap-cleaned, (c) aqua regia-cleaned, (d) solvent-cleaned.

Hsieh *et al.* have demonstrated that the atomic charge on a silicon atom bonded to four BO atoms, each of which is bonded to another silicon atom, is slightly higher than that of a silicon atom for which one of the bonds has been replaced with a bond to an NBO atom or to a BO atom that is bonded to an aluminum atom instead of a silicon atom.[28] Thus, one could expect to see more than one Si_{2p} peak in the photoelectron spectra of glasses. The charge differences are, however,

so small that the associated differences in binding energies cannot be resolved with current XPS instruments. Si_{2p} photoelectron spectra of glasses therefore currently show only one peak,[8, 29] which enfolds all the different chemical environments of the sample's silicon atoms. The Si_{2p} peaks of the four glass slides occurred at an average binding energy of 103.1 eV, which was between the Si_{2p} binding energies of quartz (103.6 eV)[30] and the mineral olivine, $(Mg, Fe)_2SiO_4$, which has only NBO atoms (101.8 eV).[31] Notable differences between the Si_{2p} core level spectra of the different glass slides were not detected.

Figure 5.3 shows the C_{1s} core level spectra for the different cleaning procedures. Adventitious carbon consists primarily of hydrocarbon compounds with a certain number of oxygen-containing functional groups.[17] Except for the spectrum of the aqua regia-cleaned glass slide, all spectra were fitted with three peaks. The largest peak, attributable to carbon atoms bonded to other carbon or to hydrogen atoms, was used as a reference peak and was placed at a binding energy of 284.6 eV.[17] The "as received", aqua regia-cleaned, and solvent-cleaned glass slides showed a second peak at 286.1 eV, which was attributed to carbon atoms singly bonded to an oxygen atom, on the basis of the C_{1s} binding energies reported for methanol (287.2 eV)[32] and the oxygen-adjacent carbon atoms of diethylether (286.8 eV).[32] (It should be noted that this reference uses a C–C/H C_{1s} binding energy of 285.0 eV, which causes the reported binding energies to be 0.4 eV higher than the energies that would be obtained with a reference binding energy of 284.6 eV.) In the spectrum of the soap-cleaned slide, this peak was located at 285.8 eV.

The detergent that was used in the soap cleaning procedure (Alconox) had a nominal composition of 10–30% sodium dodecylbenzenesulfonate, 10–30% sodium phosphate, 10–30% tetrasodium pyrophosphate, and 7–13% sodium carbonate. Sulfur and phosphorous were not detected in the survey spectrum of the soap-cleaned glass slide and sodium carbonate has a C_{1s} binding energy of 289.7 eV.[32] Furthermore, poly(styrenesulfonate), which has similar carbon chemical environments as sodium dodecylbenzensulfonate, has a C_{1s} binding energy of 285.0 eV.[33] Thus, the peak at 285.8 eV was probably not due to residual detergent and was also attributed to carbon atoms singly bonded to an oxygen atom.

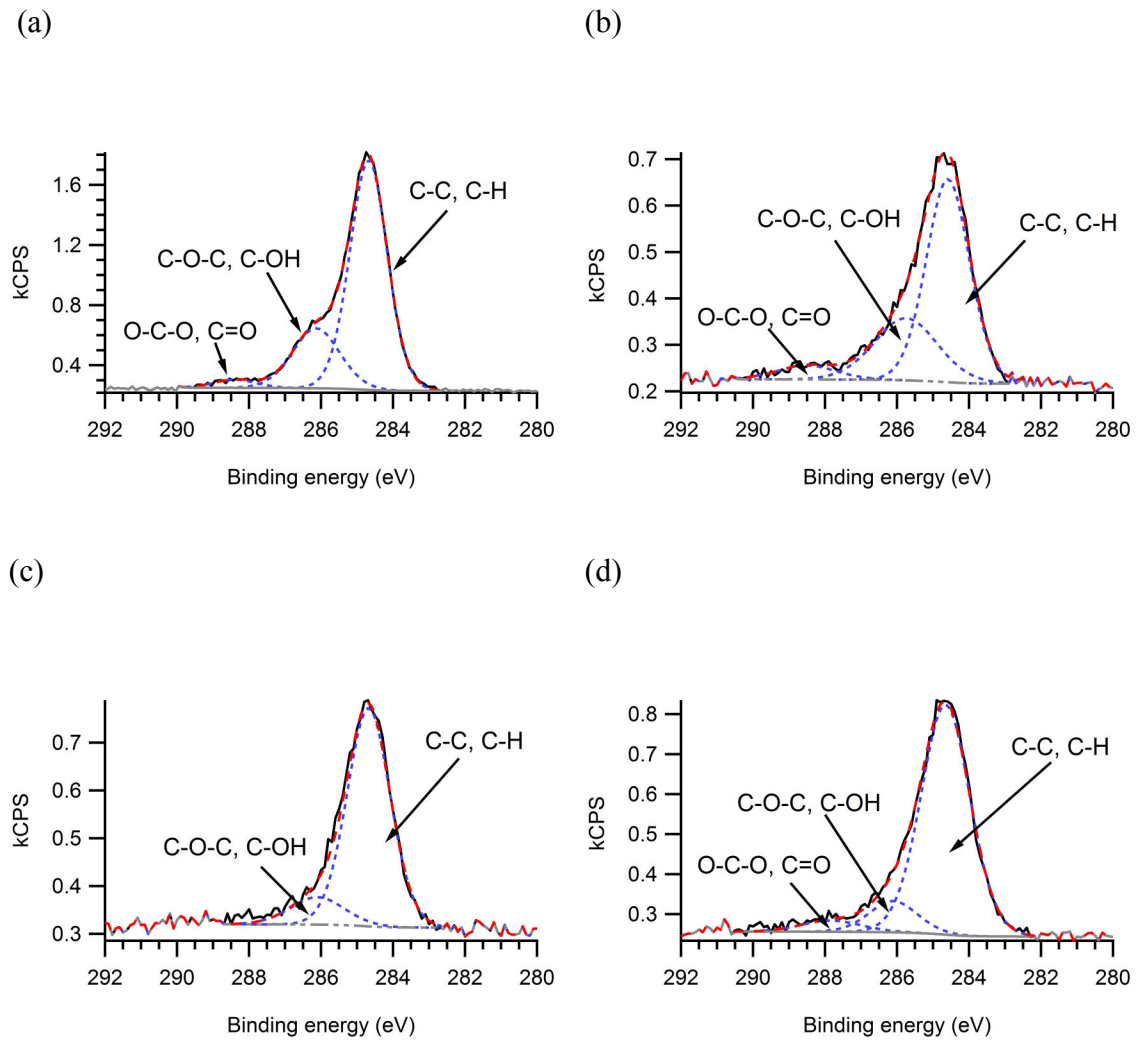

Figure 5.3. High-resolution C_{1s} photoelectron spectra of glass slides subjected to different cleaning procedures: (a) "as received", (b) soap-cleaned, (c) aqua regia-cleaned, (d) solvent-cleaned.

The "as received", soap-cleaned, and solvent-cleaned glass slides showed a third peak at binding energies above 287 eV, which was attributed to carbon atoms doubly bonded to oxygen atoms or singly bonded to two oxygen atoms, on the basis of the C_{1s} binding energies reported for the carbonyl carbon of acetone (288.1 eV)[32] and the ring carbons of paraldehyde (287.8 eV).[32] The absence of this peak in the spectrum of the aqua regia-cleaned slide indicated that the

adventitious carbon on this slide contained undetectably few carbonyl and acetal groups. The solvents that were used in the solvent cleaning procedure were ethanol and chloroform. Ethanol has C_{1s} binding energies of 286.5 and 285.1 eV[32] for the α- and β-carbon, respectively, and chloroform has a C_{1s} binding energy of 289.8 eV.[32] In light of the peak positions obtained for the solvent-cleaned glass slide (284.6, 286.1, and 287.8 eV), residual chloroform was most likely not present on the surface of that slide but the presence of residual ethanol could not be ruled out.

Figure 5.4 shows the O_{1s} core level spectra for the different cleaning procedures. The spectra should show peaks for the BO and NBO atoms as well as the oxygen atoms associated with the adventitious carbon. The O_{1s} binding energy of quartz is 532.8 eV and that of olivine 531.1 eV (referenced to a C–C/H C_{1s} binding energy of 285.0 eV),[30] which demonstrates that NBO atoms have a lower binding energy than BO atoms. The binding energies of oxygen atoms doubly bonded to carbon atoms have been reported to be in the range of 531.5–533.6 eV and those of oxygen atoms singly bonded to carbon atoms in the range of 533.1–534.9 eV.[34-37] The range of the former spans both the BO and NBO binding energies. Oxygen atoms doubly bonded to carbon atoms may therefore distort the measured BO:NBO ratio. Except for the spectrum of the aqua regia-cleaned glass slide, all spectra were fitted with three peaks. The aqua regia-cleaned slide showed a large peak at 532.6 eV, which was attributed to the BO atoms, and a small peak at 530.3 eV, which was attributed to the NBO atoms. In addition to these two peaks, the "as received", soap-cleaned, and solvent-cleaned slides showed a third peak above 533.3 eV. This peak was attributed to oxygen atoms singly bonded to carbon atoms. The absence of this peak in the spectrum of the aqua regia-cleaned slide was in disagreement with the presence of a C–O peak in the C_{1s} spectrum of the slide. The BO:NBO ratios, calculated by taking the ratios of the peak areas, were 7.6, 28.1, 211.8, and 21.5 for the "as received", soap-cleaned, aqua regia-cleaned, and solvent-cleaned glass slides, respectively. The high BO:NBO ratio of the aqua regia-cleaned slide was in accordance with the observed absence of modifier ions on the surface of this glass slide. Exchange of the modifier ions with H^+ converts the silanolate groups into silanol groups. The O_{1s} binding energy of silanol groups is only 0.3 eV lower than that of siloxane groups.[38] The silanol oxygen atoms, therefore, fall under the peak envelope of the BO atoms and are no longer measured separately. Accordingly, the soap- and solvent-cleaned glass slides had lower BO:NBO ratios than the "as received" slide because of their lower surface

modifier contents. Except for the aqua regia-cleaned slide, the BO:NBO ratios might be distorted by the carbonyl and acetal oxygen atoms of the adventitious carbon.

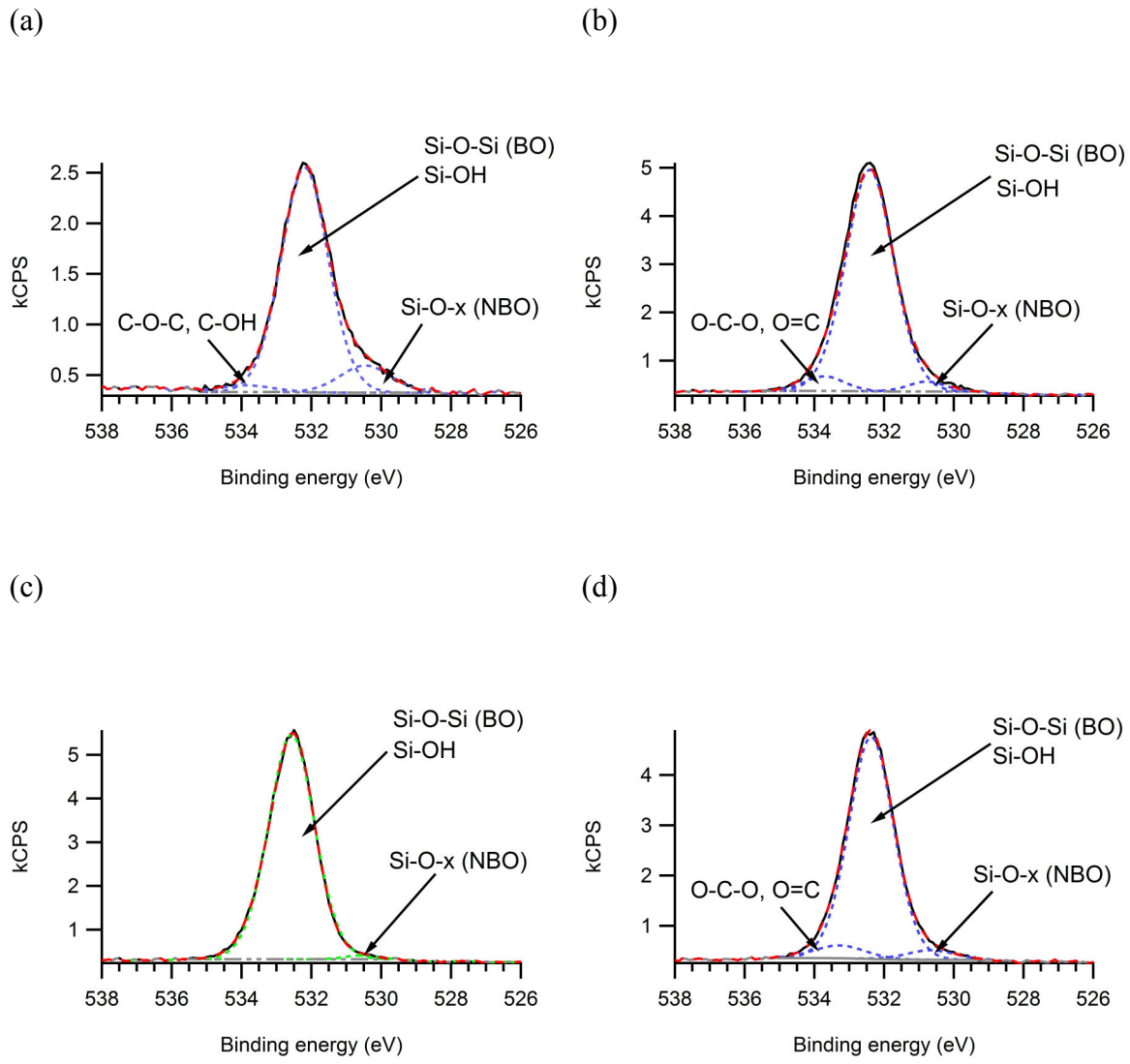

Figure 5.4. High-resolution O_{1s} photoelectron spectra of glass slides subjected to different cleaning procedures: (a) "as received", (b) soap-cleaned, (c) aqua regia-cleaned, (d) solvent-cleaned.

5.4.2. Surface free energy

The effects of the cleaning procedures on the surface free energy of the glass slides were analyzed by the Owens-Wendt-Rabel-Kaelble method.[18-20] Figure 5.5 shows the Owens-Wendt-Rabel-Kaelble plots of glass slides subjected to different cleaning procedures. The dispersive and polar components, γ_S^d and γ_S^p, respectively, of the surface free energy, γ_S, of the glass slides were determined from the intercept and the slope, respectively, of linear fits of the data. Table 5.2 lists the surface free energies and their dispersive and polar components obtained for the different glass slides. Literature values for the surface free energy of glass are 70 mJ/m^2 for a "clean" surface and 20–40 mJ/m^2 for a contaminated surface.[1] The values that we obtained were in the range of 45–60 mJ/m^2 (Table 5.2). The highest surface free energy was observed for the soap-cleaned slide, which showed slightly more polar surface properties than the "as received" slide. The lowest surface free energy was measured for the solvent-cleaned slide, which exhibited the least polar character of all slides.

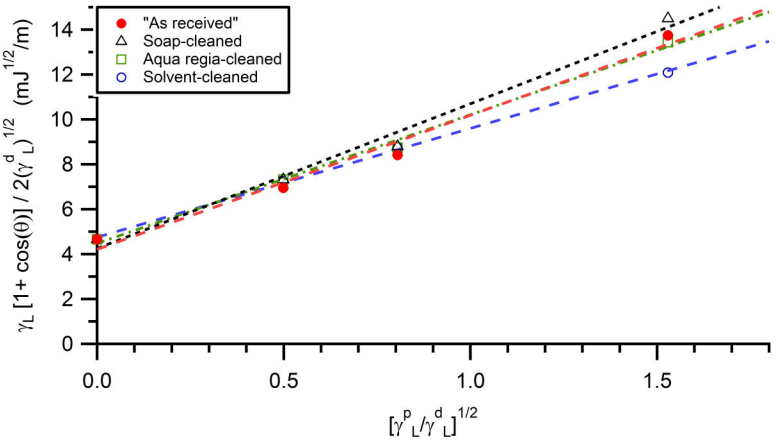

Figure 5.5. Owens-Wendt-Rabel-Kaelble plots of glass slides subjected to different cleaning procedures. Each data point is an average of 5 observations. Error bars are omitted for clarity.

The aqua regia-cleaned slide exhibited a less polar character than the "as received" slide but had a similar surface energy. The polarity of the chemical bonds present on the glass surface increases in the order C–C, C–H, C–O, O–H, Si–O. The surface polarity of the glass slides should correlate with their surface oxygen and hydrocarbon contents. The surface oxygen:hydrocarbon ratio, calculated from the relative oxygen and carbon surface contents and the C–C/H C_{1s} peak areas, are listed in Table 5.2. The surface polarities of the soap- and solvent-cleaned glass slides correlated well with their oxygen:hydrocarbon ratio but those of the "as received" and aqua regia-cleaned glass slides did not. The aqua regia-cleaned slide had a less polar character than predicted by its oxygen:hydrocarbon ratio whereas the "as received" slide was more polar than predicted. The deviation could be due to the difference in sampling depth. XPS has a sampling depth of a few nanometers whereas contact angle measurements only analyze the topmost layer of molecules. This layer might have been more polar (e.g. an oxygen-rich carbon layer) in the case of the "as received" slide or less polar (e.g. a hydrocarbon surface layer) in the case of the aqua regia-cleaned slide than the layers below.

Table 5.2. Surface free energy, γ_S, and its polar and dispersive components, γ_S^p and γ_S^d, respectively, of glass slides subjected to different cleaning procedures.

Sample	γ_S (mJ/m^2)	γ_S^p/γ_S	γ_S^d/γ_S	Surface oxygen:hydrocarbon ratio[a]
"As received"	53.4±0.1	0.67±0.0	0.33±0.0	0.7
Soap-cleaned	59.6±0.2	0.70±0.0	0.30±0.0	6.3
Aqua regia-cleaned	52.9±0.1	0.62±0.0	0.38±0.0	6.8
Solvent-cleaned	46.1±0.1	0.51±0.0	0.49±0.0	4.5

[a] calculated from the relative oxygen and carbon surface contents and the C–C/H C_{1s} peak area

5.4.3. Surface roughness and chemical homogeneity

The effects of the cleaning procedures on the surface roughness and chemical homogeneity of the glass slides were analyzed by AFM. Figure 5.6 shows representative height, amplitude, and

phase images of glass slides subjected to different cleaning procedures. The RMS surface roughness values obtained from the AFM height data are listed in Table 5.3.

Table 5.3. RMS surface roughness values of glass slides subjected to different cleaning procedures

Sample	RMS surface roughness (nm)[b]
"As received"	0.69±0.01
Soap-cleaned	0.63±0.01
Aqua regia-cleaned	0.36±0.01
Solvent-cleaned	1.02±0.02

[b] measured from 1 μm x 1 μm areas of AFM height images

The RMS roughness of the "as received" sample was in agreement with values reported in literature for untreated SLS glass microscope slides (0.63±0.07 nm)[39]. The soap cleaning procedure had only a minor effect on the RMS surface roughness. The aqua regia cleaning procedure greatly reduced the surface roughness of the glass slides whereas the solvent cleaning procedure caused a significant increase in surface roughness. The reduction in RMS surface roughness caused by the aqua regia-cleaning procedure supported our interpretation of the XPS results of the concomitant dissolution of SiO_2 with other glass components during the aqua regia cleaning procedure.

Currently, we do not have an explanation for the increase in surface roughness brought about by the solvent cleaning procedure. The height and amplitude images (Figure 5.6) revealed a granular topography for all glass slides. Although the RMS surface roughness values of the "as received" and soap-cleaned glass slides were similar, a difference in surface topography was observable in the height images. Whereas the topography of the "as received" slide was uniform, the soap-cleaned glass slide showed large protuberances on a fairly smooth background. This topography was in accordance with our interpretation of the XPS results of the selective dissolution of SiO_2 but not the aluminum glass component during the soap cleaning procedure.

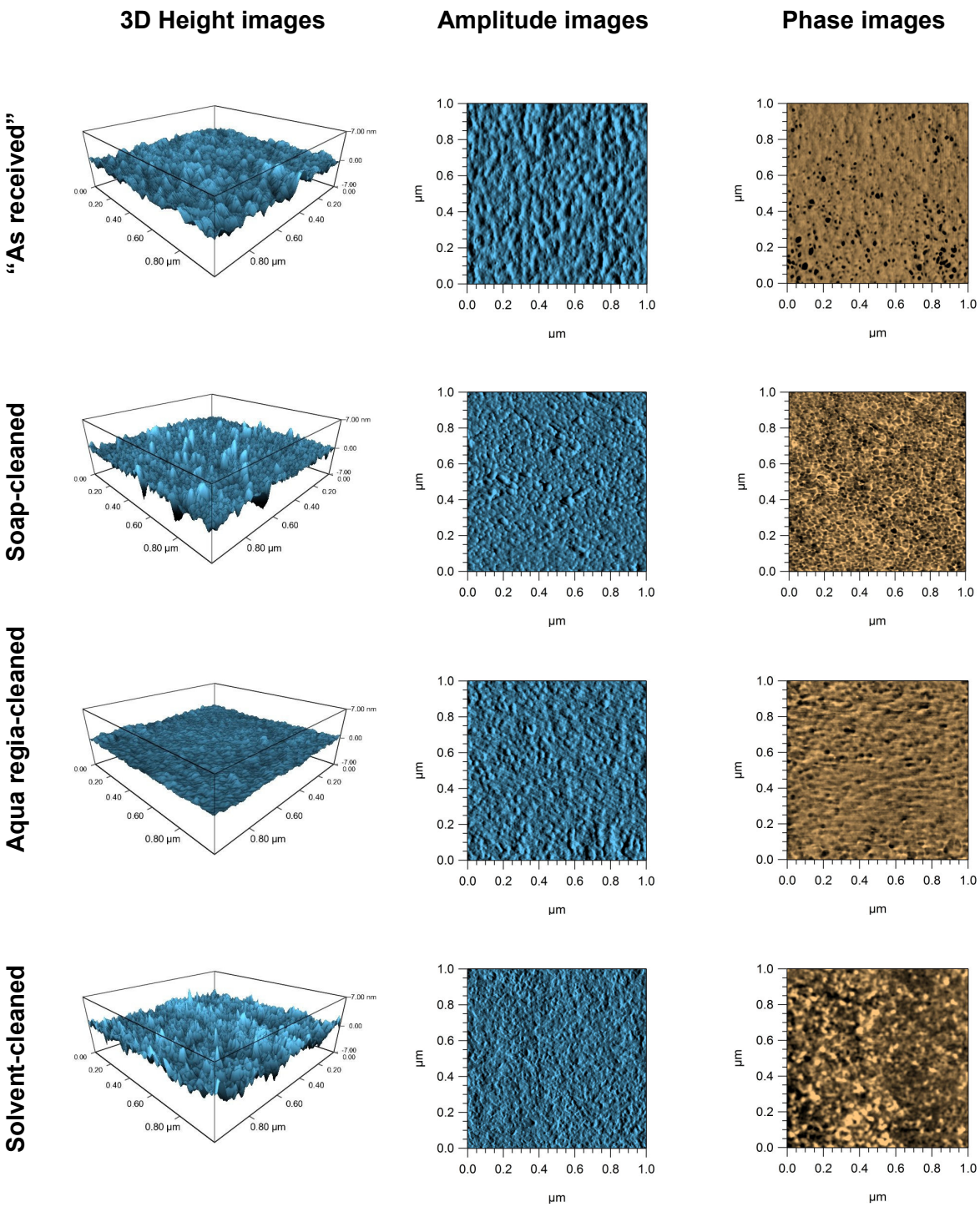

Figure 5.6. AFM height, amplitude, and phase images of glass slides subjected to different cleaning procedures. The z-scales for the amplitude and phase images are 600 pm and 5 degrees, respectively.

The phase image of the "as received" glass slide showed dark spots, indicating areas of greater phase lag. The phase image of the aqua regia-cleaned glass slide looked similar but had fewer spots. Adventitious carbon has been described as a series of well dispersed nanostructures composed of physically isolated sections.[17] The dark spots in the phase images of the "as received" and aqua regia-cleaned glass slides might therefore be isolated patches of adventitious carbon. The phase images of the soap- and solvent-cleaned glass slides also showed dark spots but the rest of the images looked quite different with respect to the image of the "as received" slide. Both images were mottled but the image of the soap-cleaned glass slide had highlighted grain edges whereas the image of the solvent-cleaned slide did not but instead showed bright spots, indicating areas of lesser phase lag. The phase images of the glass slides revealed a certain degree of chemical inhomogeneity.

5.4.4. Streaming and ζ-potentials

The effects of the cleaning procedures on the streaming and ζ-potentials of the glass slides were analyzed by streaming potential measurements. Figure 5.7 shows streaming potential curves for glass slides subjected to different cleaning procedures. The curves are averages of ten measurements. The measured streaming potentials were converted to ζ-potentials with the equation published by Sides et al.[21]. The streaming and ζ-potentials of the glass slides are listed in Table 5.4. The ζ-potential of the "as received" glass slide was in good agreement with the value reported by Lameiras et al. (~ –100 mV),[40] obtained with the same method (rotating disk), but much higher than the values reported by Mohiuddin Mala et al.[41] and Gu and Li[42] (~ –60 mV), obtained with the parallel plate method. In addition to the difference in the analytical method, experimental differences in the glass cleaning procedure and conductivity of the DI water are potential reasons for this discrepancy.

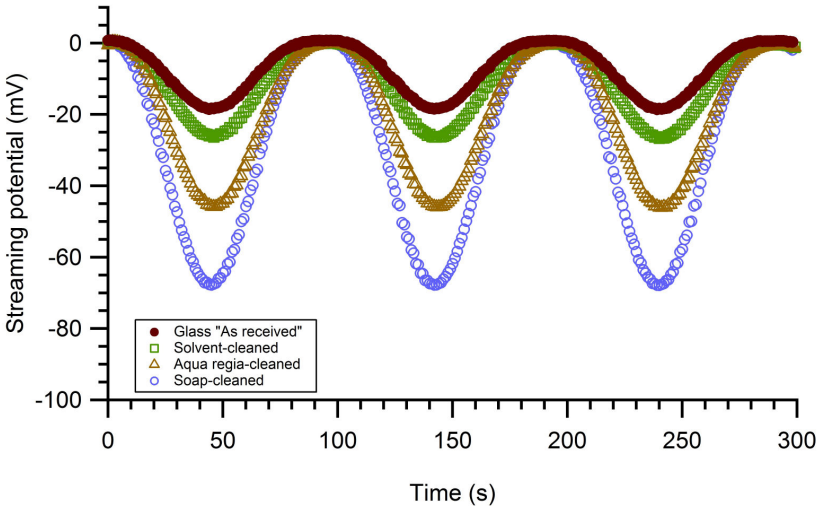

Figure 5.7. ZetaSpin curves for glass slides subjected to different cleaning procedures. Each curve is an average of ten measurements. Measurements were done in DI water in the absence of electrolyte.

Table 5.4. Streaming and ζ-potentials of glass slides subjected to different cleaning procedures.

Sample	Streaming potential (mV)	ζ-potential (mV)
"As received"	–19.1±0.0	–105.2±0.2
Soap-cleaned	–68.7±2.1	–448.5±2.9
Aqua regia-cleaned	–46.0±0.6	–392.6±0.9
Solvent-cleaned	–26.1±0.2	–145.6±0.7

As mentioned earlier, glass surfaces contain a large number of silanol groups ($\leq$ 4.6 nm^{-2}),[23] which have a pKa of 6.8.[43] Consequently, when a glass surface is in contact with DI water, about 50% of the surface's silanol groups are dissociated. These negatively charged silanolate groups are the reason for the negative ζ-potential of glass surfaces. The ζ-potential of the solvent-cleaned glass slide was slightly higher, in absolute terms, than that of the "as received" slide. A study of the acidity of hydroxyl groups on silica–alumina surfaces has shown that the acidity of

the hydroxyl groups increases with the aluminum content.[44] Given that the solvent-cleaned glass slide had a higher surface aluminum content than the "as received" glass slide, the larger ζ-potential could be related to a higher acidity of the surface hydroxyl groups, with respect to those of the "as received" slide. Another, probably more important, reason for the higher ζ-potential could be the reduced surface modifier content and therefore higher silanol content of the solvent-cleaned glass slide with respect to the "as received" glass slide. The highest ζ-potential was observed for the soap-cleaned glass slide. The soap cleaning procedure exposed the glass slides to an alkaline (pH > 9.5) detergent solution. Above pH 9,[1] siloxane bonds react with hydroxyl ions under formation of silanol and silanolate groups. Thus, the high ζ-potential of the soap-cleaned glass slide was probably due to a large number of surface silanol and silanolate groups. The aqua regia-cleaned glass slide had a ζ-potential intermediate between that of the soap– and solvent–cleaned glass slides. The higher ζ-potential of the aqua regia-cleaned slide with respect to the "as received" slide was attributed to the much-reduced surface modifier content and accordingly increased silanol content.

5.4.5. Charge distribution on dry surfaces

The effects of the cleaning procedures on the surface charge distribution of the glass slides in air were analyzed by SKPM. SKPM measures the electric potential between a sample's surface and a conductive AFM tip positioned at some distance above the surface. It is important to note that the measured potential is neither the true electric surface potential of the sample[45] nor the true contact potential difference between the sample's surface and the probe.[46] For insulators, the measured potential between the tip and the sample depends on (a) the tip and cantilever geometry, (b) the lateral electrostatic periodicity of the sample, and (c) the dielectric properties (e.g. polarizability) of the sample, which for measurements in air will be affected by surface water.[47-49] Thus, although SKPM currently cannot accurately measure electric surface potential, it can provide relative information about the local surface charge of the sample.

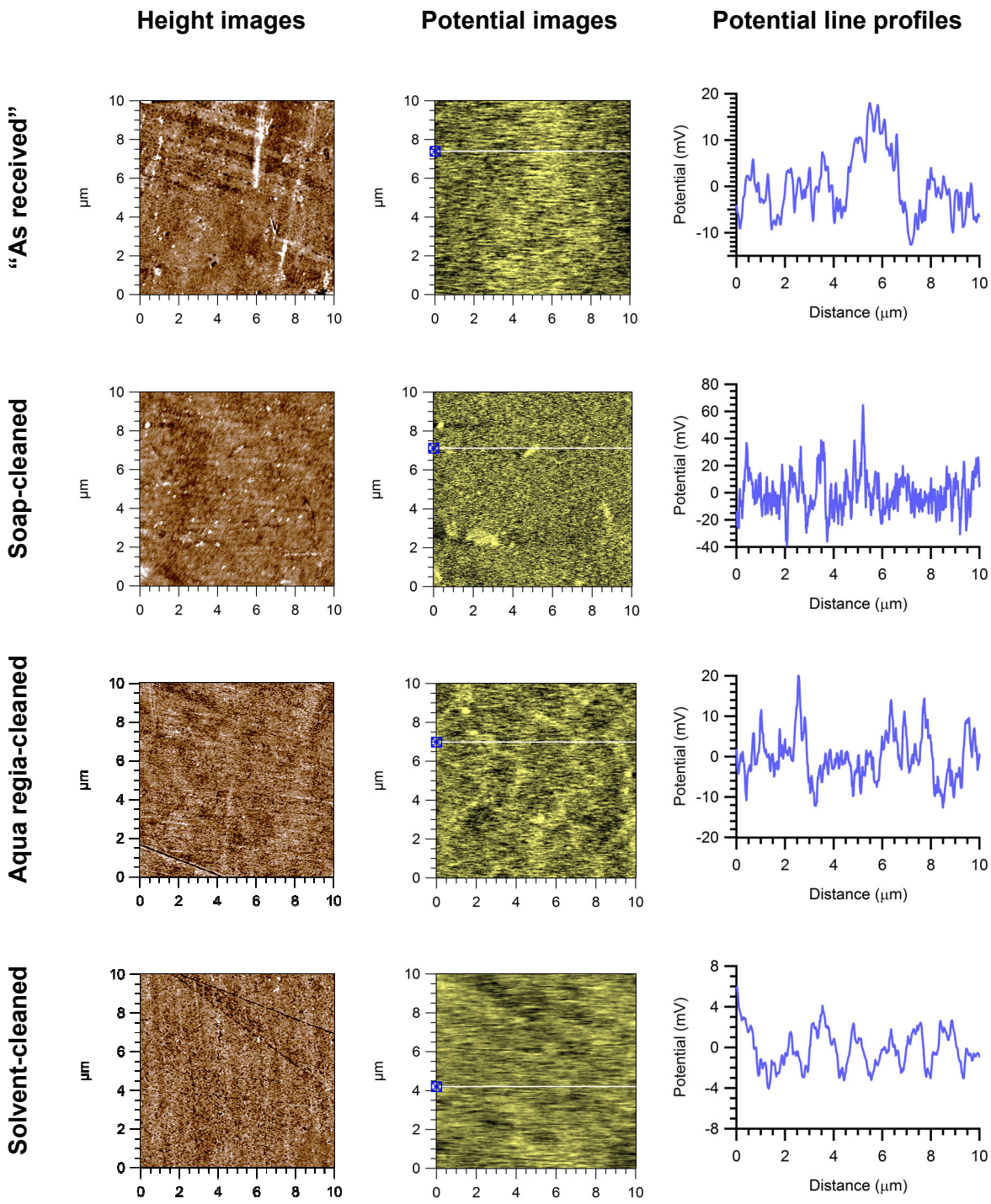

Figure 5.8. SKPM height images, potential images, and potential line profiles of glass slides subjected to different cleaning procedures. The z-scales for the height and potential images are 2 nm and 35 mV, respectively.

Figure 5.8 shows representative height images, potential images, and potential line scans of glass slides subjected to different cleaning procedures. For minimization of the obscuring effect of surface water, images were recorded at low relative humidity (5%). The potential image of the solvent-cleaned glass slide was featureless and had the lowest RMS potential variation of all images (4.9 mV). The potential image of the "as received" slide showed a vertical band with a more positive potential (20 mV), indicating a positive surface charge within the band.The potential image of the soap-cleaned slide showed positively charged patches (> 60 mV) and had the highest RMS potential variation of all images (12.9 mV). Most strikingly, the potential image of the aqua regia-cleaned glass slide showed a honeycomb pattern of positive surface charge (20 mV). The RMS potential variations of the "as received" and aqua regia-cleaned glass slide were 5.9 and 7.3 mV, respectively. Currently, we do not have a good explanation for the positive surface charge observed on some of the glass slides. The charge could possibly be due to the modifier ions, although XPS analysis showed that the surface of the aqua regia-cleaned slide was devoid of modifier ions and that of the soap-cleaned slide contained very few, or it could be due to positively charged defects in the glass matrix,[50-51] but such defects are usually induced by ionizing radiation. Another possible and maybe the most likely reason for the surface charge are surface-adsorbed positively-charged atoms or molecules.

5.5. Conclusions

The objective of this study was to determine the effects of different cleaning procedures on the surface properties of glass substrates. Our conclusions, which are based on SLS glass substrates, are summarized in Table 5.5. The overall conclusion is that the cleaning procedure needs to be chosen on the basis of the desired surface properties for the glass substrates.

Table 5.5. Effects of different cleaning procedures on the surface properties of SLS glass substrates.[a]

Property	Soap cleaning	Aqua regia cleaning	Solvent cleaning
Surface Na, Ca, Mg content	−	− −	−
Surface Al content	+	−	+
Surface BO:NBO ratio[b]	+	++	+
Adventitious carbon composition	C–C/H, C–O, C=O/O–C–O	C–C/H, C–O	C–C/H, C–O, C=O/O–C–O
Surface polarity	+	−	− −
Surface free energy	+	O	−
ζ-potential (absolute value)	+++	++	+
Surface roughness	O	−	+
Positive surface charge pattern (in air)	Patches	honeycomb	None

[a] + increase, ++ strong increase, +++ very strong increase – decrease, – – strong decrease, O no/small effect

[b] represents conversion of silanolate to silanol groups

5.6. Acknowledgements

This project was supported by the National Research Initiative of the USDA Cooperative State Research, Education and Extension Service, grant number 2005-35504-16088, and by the National Science Foundation under grant numbers CHE-0724126 and DMR-0907567. The authors also gratefully acknowledge the generous scholarship support for F. N. by the Mexican Secretariat of Public Education (SEP) through its Professional Development for Teachers Program (PROMEP). The authors thank Prof. William Ducker for access to the ZetaSpin apparatus. Furthermore, additional support from OMNOVA, Inc. and Tembec, Inc. are also acknowledged.

5.7. References

1. Le Bourhis, E. Glass; Mechanics and Technology. WILEY-VCH: Weinheim, Germany, 2008.
2. De Marchi, G.; Gonella, F.; Mazzoldi, P.; Battaglin, G.; Knystautas, E. J.; Meneghini, C. Non-linear glasses by metal cluster formation: synthesis and properties. *Journal of Non-Crystalline Solids* **1996,** 196, 79-83.
3. Salgueiro, J. R.; Roman, J. F.; Moreno, V. System for laser writing to lithograph masks for integrated optics. *Optical Engineering* **1998,** 37, 1115-1123.
4. Pellegrino, P.; Garrido, B.; Lebour, Y.; Moreno, J. A.; Garcia, C.; Morante, J. R.; Bettotti, P.; Pavesi, L.; Prassas, M. Luminescent properties of Er and Si co-implanted silicates. *Optical Materials* **2005,** 27, 910-914.
5. Cho, Y.; Lee, S.; An, M.; Kim, D. Transparent carbon nanotube field emission devices for display and lamp. *physica status solidi (a)* **2007,** 204, 1804-1807.
6. Hwang, M.-S.; Lee, H. J.; Jeong, H. S.; Seo, Y. W.; Kwon, S. J. The effect of pulsed magnetron sputtering on the properties of indium tin oxide thin films. *Surface and Coatings Technology* **2002,** 171, 29-33.
7. Finley, J. J. Development of a multilayer thin-film solar control windshield. 1996; pp 739-746.
8. Sharma, A.; Jain, H.; Miller, A. C. Surface modification of a silicate glass during XPS experiments. *Surface and Interface Analysis* **2001,** 31, 369-374.
9. Szanyi, J. The origin of haze in CVD tin oxide thin films. *Applied Surface Science* **2002,** 185, 161-171.
10. Serra, J.; Gonzalez, P.; Liste, S.; Serra, C.; Chiussi, S.; Leon, B.; Perez-Amor, M.; Ylanen, H. O.; Hupa, M. FTIR and XPS studies of bioactive silica based glasses. *Journal of Non-Crystalline Solids* **2003,** 332, 20-27.
11. Hayashi, Y.; Akiyama, R.; Kudo, M. Surface characterization of float glass related to changes in the optical properties after reheating. *Surface and Interface Analysis* **2001,** 31, 87-92.

12. Beerkens, R. G. C.; Kahl, K. Chemistry of sulphur in soda-lime-silica glass melts. *Physics and Chemistry of Glasses* **2002,** 43, 189-198.
13. Koike, A.; Tomozawa, M. Size effect on surface structural relaxation kinetics of silica glass sample. *Journal of Non-Crystalline Solids* **2006,** 352, 3787-3793.
14. Brückner, R.; Chun, H. U.; Goretzki, H.; Sammet, M. XPS measurements and structural aspects of silicate and phosphate glasses. *Journal of Non-Crystalline Solids* **1980,** 42, 49-60.
15. North, S. H.; Lock, E. H.; King, T. R.; Franek, J. B.; Walton, S. G.; Taitt, C. R. Effect of Physicochemical Anomalies of Soda-Lime Silicate Slides on Biomolecule Immobilization. *Analytical Chemistry* **2010,** 82, 406-412.
16. Yamamoto, Y.; Yamamoto, K. Precise XPS depth profile of soda-lime-silica glass using C60 ion beam. *Journal of Non-Crystalline Solids* **2010,** 356, 14-18.
17. Barr, T. L.; Seal, S. Nature of the Use of Adventitious Carbon as a Binding-Energy Standard. *Journal of Vacuum Science & Technology a-Vacuum Surfaces and Films* **1995,** 13, 1239-1246.
18. Owens, D. K.; Wendt, R. C. Estimation of the surface free energy of polymers. *Journal of Applied Polymer Science* **1969,** 13, 1741-1747.
19. Rabel, W. Einige Aspekte der Benetzungstheorie und ihre Anwendung auf die Untersuchung und Veränderung der Oberflächeneigenschaften von Polymeren. *Farbe und Lack* **1971,** 77, 997-1006.
20. Kaelble, D. H. Dispersion-Polar Surface Tension Properties of Organic Solids. *Journal of Adhesion* **1970,** 2, 66-81.
21. Sides, P. J.; Newman, J.; Hoggard, J. D.; Prieve, D. C. Calculation of the streaming potential near a rotating disk. *Langmuir* **2006,** 22, 9765-9769.
22. Wicks, G. G. Nuclear Waste Glasses: Corrosion Behavior and Field Tests. In: Corrosion of Glass, Ceramics and Ceramic Superconductors; Clark, D. E., Zoitos, B. K., Eds.; Noyes Publications: Park Ridge, NJ, 1992; pp 218-268.

23. Bather, J. M.; Gray, R. A. C. Relationship between Chromatographic Performance and Surface-Structure of Silica Microspheres. *Journal of Chromatography* **1976,** 122, 159-169.
24. Grambow, B. Geochemical Approach to Glass Dissolution. In: Corrosion of Glass, Ceramics and Ceramic Superconductors; Clark, D. E., Zoitos, B. K., Eds.; Noyes Publications: Park Ridge, NJ, 1992; pp 124-152.
25. White, W. B. Theory of Corrosion of Glass and Ceramics. In: Corrosion of Glass, Ceramics and Ceramic Superconductors; Clark, D. E., Zoitos, B. K., Eds.; Noyes Publications: Park Ridge, NJ, 1992; pp 2-28.
26. Jantzen, C. M. Thermodynamic Approach to Glass Corrosion. In: Corrosion of Glass, Ceramics and Ceramic Superconductors; Clark, D. E., Zoitos, B. K., Eds.; Noyes Publications: Park Ridge, NJ, 1992; pp 153-217.
27. Clark, D. E.; Zoitos, B. K. Corrosion Testing and Characterization. In: Corrosion of Glass, Ceramics and Ceramic Superconductors; Clark, D. E., Zoitos, B. K., Eds.; Noyes Publications: Park Ridge, NJ, 1992; pp 51-102.
28. Hsieh, C. H.; Jain, H.; Miller, A. C.; Kamitsos, E. I. X-Ray Photoelectron-Spectroscopy of Al-Substituted and B-Substituted Sodium Trisilicate Glasses. *Journal of Non-Crystalline Solids* **1994,** 168, 247-257.
29. Nagel, S. R.; Tauc, J.; Bagley, B. G. X-ray Photoemission of a Soda-Lime-Silica Glass. *Solid State Communications* **1976,** 20, 245-249.
30. Zakaznova-Herzog, V. P.; Nesbitt, H. W.; Bancroft, G. M.; Tse, J. S.; Gao, X.; Skinner, W. High-resolution valence-band XPS spectra of the nonconductors quartz and olivine. *Physical Review B* **2005,** 72, 205113.
31. Zakaznova-Herzog, V. P.; Nesbitt, H. W.; Bancroft, G. M.; Tse, J. S. High resolution core and valence band XPS spectra of non-conductor pyroxenes. *Surface Science* **2006,** 600, 3175-3186.
32. Gelius, U.; Hedén, P. F.; Hedman, J.; Lindberg, B. J.; Manne, R.; Nordberg, R.; Nordling, C.; Siegbahn, K. Molecular Spectroscopy by Means of ESCA III. Carbon compounds. *Physica Scripta* **1970,** 2, 70.

33. Jonsson, S. K. M.; Birgerson, J.; Crispin, X.; Greczynski, G.; Osikowicz, W.; van der Gon, A. W. D.; Salaneck, W. R.; Fahlman, M. The effects of solvents on the morphology and sheet resistance in poly (3,4-ethylenedioxythiophene)-polystyrenesulfonic acid (PEDOT-PSS) films. *Synthetic Metals* **2003,** 139, 1-10.
34. Clark, D. T.; Dilks, A. ESCA Applied to Polymers XXIII. RF Glow Discharge Modification of Polymers in Pure Oxygen and Helium-Oxygen Mixtures. *Journal of Polymer Science Part A-Polymer Chemistry* **1979,** 17, 957-976.
35. Barth, G.; Linder, R.; Bryson, C. Advances in Charge Neutralization for XPS Measurements of Nonconducting Materials. *Surface and Interface Analysis* **1988,** 11, 307-311.
36. Gross, T.; Lippitz, A.; Unger, W. E. S.; Wöll, C.; Hähner, G.; Braun, W. Some remarks on fitting standard- and high-resolution C 1s and O 1s X-ray photoelectron spectra of PMMA. *Applied Surface Science* **1993,** 68, 291-298.
37. Le, Q. T.; Pireaux, J. J.; Caudano, R. XPS study of the PET film surface modified by CO2 plasma: Effects of the plasma parameters and ageing. *Journal of Adhesion Science and Technology* **1997,** 11, 735-751.
38. Simmons, G. W.; Angst, D. L.; Klier, K. A self-modeling approach to the resolution of XPS spectra into surface and bulk components. *Journal of Electron Spectroscopy and related Phenomena* **1999,** 105, 197-210.
39. North, S. H.; Lock, E. H.; King, T. R.; Franek, J. B.; Walton, S. G.; Taitt, C. R. Effect of Physicochemical Anomalies of Soda-Lime Silicate Slides on Biomolecule Immobilization. *Analytical Chemistry* **2009,** 82, 406-412.
40. Lameiras, F. S.; de Souza, A. L.; de Melo, V. A. R.; Nunes, E. H. M.; Braga, I. D. Measurement of the Zeta Potential of Planar Surfaces With a Rotating Disk. *Materials Research-Ibero-American Journal of Materials* **2008,** 11, 217-219.
41. Mohiuddin Mala, G. M.; Li, D. Q.; Werner, C.; Jacobasch, H. J.; Ning, Y. B. Flow characteristics of water through a microchannel between two parallel plates with electrokinetic effects. *International Journal of Heat and Fluid Flow* **1997,** 18, 489-496.

42. Gu, Y. G.; Li, D. Q. The zeta-potential of glass surface in contact with aqueous solutions. *Journal of Colloid and Interface Science* **2000,** 226, 328-339.
43. Schindler, P.; Kamber, H. R. Die Acidität von Silanolgruppen. Vorläufige Mitteillung. *Helvetica Chimica Acta* **1968,** 51, 1781-1786.
44. Rouxhet, P. G.; Sempels, R. E. Hydrogen bond strengths and acidities of hydroxyl groups on silica–alumina surfaces and in molecules in solution. *Journal of the Chemical Society-Faraday Transactions I: Physical Chemistry in Condensed Phases* **1974,** 70, 2021 - 2032.
45. Charrier, D. S. H.; Kemerink, M.; Smalbrugge, B. E.; de Vries, T.; Janssen, R. A. J. Real versus measured surface potentials in scanning Kelvin probe microscopy. *ACS Nano* **2008,** 2, 622-626.
46. Baumgart, C.; Helm, M.; Schmidt, H. Quantitative dopant profiling in semiconductors: A Kelvin probe force microscopy model. *Physical Review B* **2009,** 80, 085305.
47. Sugimura, H.; Ishida, Y.; Hayashi, K.; Takai, O.; Nakagiri, N. Potential shielding by the surface water layer in Kelvin probe force microscopy. *Applied Physics Letters* **2002,** 80, 1459-1461.
48. Bocquet, F.; Nony, L.; Loppacher, C.; Glatzel, T. Analytical approach to the local contact potential difference on (001) ionic surfaces: Implications for Kelvin probe force microscopy. *Physical Review B* **2008,** 78, 035410.
49. Liscio, A.; Palermo, V.; Müllen, K.; Samorì, P. Tip-Sample Interactions in Kelvin Probe Force Microscopy: Quantitative Measurement of the Local Surface Potential. *Journal of Physical Chemistry C* **2008,** 112, 17368-17377.
50. Fowler, W. B.; Edwards, A. H. Theory of defects and defect processes in silicon dioxide. *Journal of Non-Crystalline Solids* **1997,** 222, 33-41.
51. Uchino, T.; Yoko, T. Density functional theory of structural transformations of oxygen-deficient centers in amorphous silica during hole trapping: Structure and formation mechanism of the E '(gamma) center. *Physical Review B* **2006,** 74, 125203.

Chapter 6

Radial Alignment of Rod-like Nanoparticles in Drying Droplets

Radial Alignment of Rod-like Nanoparticles in Drying Droplets

Fernando Navarro and Maren Roman

Macromolecules and Interfaces Institute and Department of Wood Science and Forest Products, 230 Cheatam Hall, Virginia Polytechnic Institute and State University, Blacksburg, Virginia, 24061, United States of America.

6.1. Abstract

The controlled placement of polymers and nanoparticles onto solid substrates using colloidal deposition methods requires a detailed understanding of the hydrodynamics and mass transport processes in evaporating sessile droplets. A drying droplet with a pinned contact line is known to develop a radial, outward capillary flow. Using polarized-light and atomic force microscopy, we show that this radial, outward capillary flow can cause shear-induced, radial alignment of suspended rod-like nanoparticles. Our results demonstrate the utility of rod-like nanoparticles in the study of droplet hydrodynamics.

Keywords: c*ellulose nanocrystals, drying droplet, radial alignment, polarized-light microscopy, AFM.*

6.2. Introduction

The drying of droplets of colloidal suspensions on non-absorbing, solid surfaces is a ubiquitous phenomenon. Coffee stains on table surfaces and water stains on kitchen and bathroom fixtures are two familiar examples of the ensuing particle deposits. Recent technological advances, such as the patterning of polymers and nanoparticles by inkjet printing and the fabrication of chemical and biological microarrays, require a detailed understanding of the hydrodynamics and mass transport processes in evaporating sessile droplets.[1-2]

Two extreme modes of evaporation can be distinguished:[3] Upon drying, a droplet can either maintain its contact angle and decrease in diameter or it can maintain its diameter and decrease in contact angle. In many cases, a combination of the two extremes is observed. A decrease in contact angle upon drying occurs when the contact line of the droplet is pinned to its initial position by surface roughness or chemical heterogeneities of the substrate. A drying droplet with a pinned contact line develops a radial, outward capillary flow, which carries any dissolved or suspended matter to the periphery of the droplet, leading to ring-like deposits of the solutes or particles.[4]

We show that the radial, outward capillary flow in drying droplets can cause shear-induced, radial alignment of suspended rod-like nanoparticles. For this proof-of-principle study, we used aqueous suspensions of wood-derived cellulose nanocrystals (Figure 6.1-a). Cellulose nanocrystals are highly crystalline fragments of natural cellulose fibers with average dimensions, for wood-based cellulose, between 100 and 150 nm in length and 3 and 5 nm in width.[5]

6.3. Experimental

6.3.1. Cellulose nanocrystal preparation

Cellulose nanocrystals were prepared from dissolving-grade softwood sulfite pulp (Temalfa 93A-A), kindly provided by Tembec, Inc. Lapsheets of the pulp were cut into pieces of approximately 1 × 1 cm and milled in a Wiley mill (Thomas Wiley Mini-Mill) to pass a 60 mesh screen. The milled pulp was hydrolyzed under stirring with 60 wt % sulfuric acid (10 mL/g cellulose) at 50 °C for 60 min. The hydrolysis was stopped by diluting the reaction mixture 10-fold with deionized water (Millipore Direct-Q 5, 18.2 MΩ·cm). The nanocrystals were collected and washed once with deionized water by centrifugation for 10 min at 25 °C and 4550 × g (Thermo IEC Centra-GP8R) and then dialyzed (Spectra/Por 4 dialysis tubing) against deionized water until the pH of fresh dialysis medium stayed constant over time. The nanocrystal suspension was sonicated (Sonics & Materials Model VC-505) for 10 min at 200 W under ice-

bath cooling and filtered through a 0.45 μm polyvinylidene fluoride syringe filter (GD/XP, Whatman) to remove any aggregates present.

6.3.2. Cleaning of glass substrates

A 3:1 mixture by volume of hydrochloric acid (NF/FCC, Fisher Chemical, 36.5-38%) and nitric acid (NF, Fisher Chemical, 69-70%) was poured into a glass staining dish loaded with 3 × 1 in. glass microscope slides (PEARL, MingZhu Industries). The staining dish was covered and left undisturbed for 30 min. Then, the acid mixture was replaced with deionized water and the staining dish placed into an ultrasonic bath (Branson 3510 Ultrasonic Cleaner) and subjected to ultrasound for 10 min at 45 °C. The slides were ultrasonicated twice more in the presence of fresh deionized water for 5 and 2 min, respectively. Finally, the slides were dried in a stream of nitrogen and stored in a slide storage box. Before use, glass slides were cut with a diamond-tipped glass cutter into 1.5 in. × 1 in. pieces.

6.3.3. Preparation of dried droplets

A small droplet (2 μL) of a 1 wt % cellulose nanocrystal suspension was placed onto a cleaned glass slide in a polystyrene Petri dish (∅ = 50 mm). The dish was covered with a polystyrene lid that had been perforated in the center with a hole of approximately 1 mm in diameter, and the droplet was allowed to dry overnight.

6.3.4. Polarized-light microscopy

Polarized-light microscopy experiments employed a Zeiss Axioskop 40 A POL, equipped with a 530 nm first-order retardation plate. The polarizer and analyzer were oriented in east–west and north–south direction, respectively. The first-order retardation plate was inserted so that its slow axis was oriented northeast–southwest and its fast axis northwest–southeast. Images were recorded with a Canon EOS 20D digital single-lens reflex camera (8.2 megapixels) mounted onto the microscope.

6.3.5. Atomic force microscopy

Atomic force microscopy (AFM) was performed with an Asylum Research MFP 3D mounted onto an Olympus IX 71 inverted fluorescence microscope. For images of individual cellulose nanocrystals, 100 μL of a 0.001 wt % aqueous suspension of cellulose nanocrystals was spin coated (3000 rpm, 1 min) onto an aqua regia-cleaned glass slide. The sample was scanned in intermittent contact mode in air, using Nanoworld SSS-NCH Super Sharp Silicon probes (nominal tip radius: <5 nm). Dried droplets were scanned in intermittent contact mode in air, using Olympus OMCL-AC160TS probes (nominal tip radius: <10 nm).

6.4. Results

6.4.1. Morphology of the dried droplets

Small droplets (2 μL) of a 1 wt % suspension of cellulose nanocrystals were allowed to evaporate slowly on aqua regia-cleaned glass slides and the resulting deposits were analyzed by polarized-light microscopy. Cellulose is birefringent, having a higher refractive index along the polymer backbone than perpendicular to it. As a result, an ordered cellulose domain appears bright under cross-polarized illumination unless its direction of high refractive index, corresponding to the slow optical axis of that domain, is aligned with the transmission axis of one of the polarizers. Because the polymer chains in cellulose nanocrystals are oriented along the long axis of the particles, the slow optical axis of an ordered domain indicates the orientation of the long axis of the nanocrystals. When viewed between crossed polarizers, with conventional east–west (E/W) and north–south (N/S) orientations, dried cellulose nanocrystal droplets displayed Maltese cross extinction patterns (Figure 6.1-b), indicating radial symmetry of the optical axes.

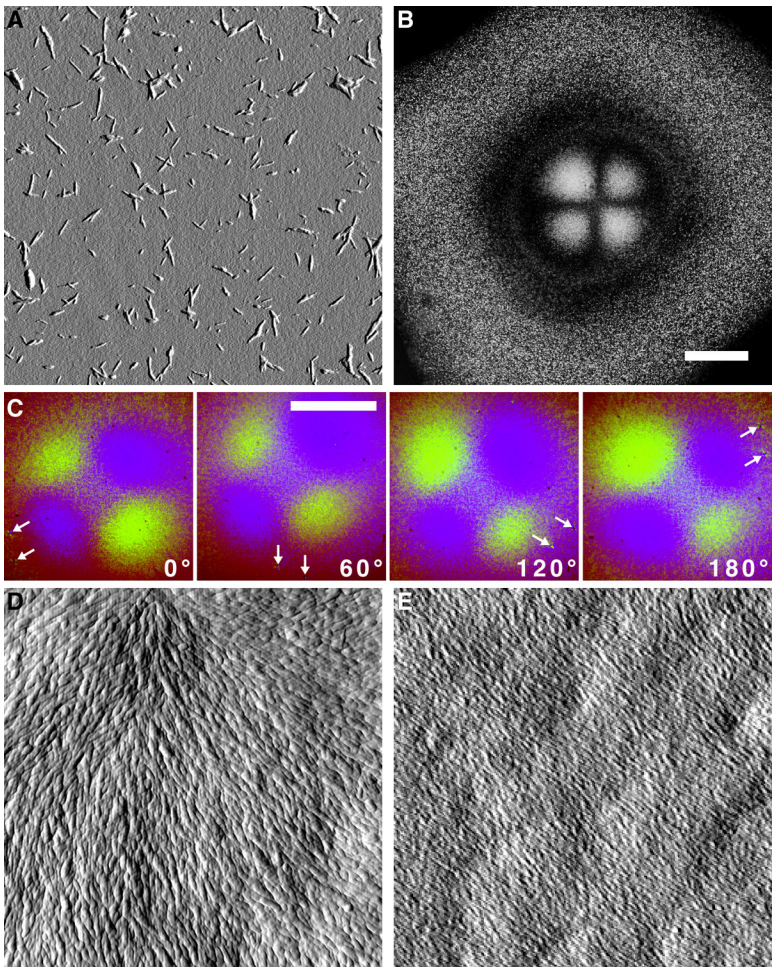

Figure 6.1. (a) AFM amplitude image of cellulose nanocrystals (scan size: 5 μm); (b) Polarized-light micrograph of a dried 2 μL droplet of a cellulose nanocrystal suspension showing a Maltese cross extinction pattern (scale bar: 500 μm); (c) Polarized-light micrographs of the Maltese cross region at different sample orientations viewed using a first-order retardation plate (scale bar: 500 μm, arrows mark two dust particles for reference of sample orientation); (d) AFM amplitude image of an area near the center of the droplet showing radial alignment of the nanocrystals (scan size: 2.5 μm); (e) AFM amplitude image of an area some distance away from the center of the droplet showing parallel alignment of the nanocrystals (scan size: 5 μm).

The direction of the optical axes of a birefringent sample can be determined with a first-order retardation plate, which produces blue color where the slow optical axis of the sample is aligned with the slow optical axis of the wave plate and yellow color where the slow axis of the sample is aligned with the fast axis of the wave plate, i.e. the wave plate's direction of low refractive index. By convention, the slow optical axis of a first-order retardation plate is oriented in a NE/SW direction. Figure 6.1-c shows the center of a dried cellulose nanocrystal droplet at different sample orientations viewed with a first-order retardation plate. Blue indicates a NE/SW orientation of the nanocrystals and yellow a NW/SE orientation. Rotation of the microscope's sample stage did not alter the color pattern, consistent with a radial alignment of the rod-like particles.

The radial alignment of the nanocrystals was also evident by atomic force microscopy (AFM). Figure 6.1-d shows an AFM image of a 2.5 × 2.5 μm area near the center of a droplet. In the image, the rod-like particles all seem to be pointing to a common origin. At some distance from the center, large areas (>100 μm^2) showed parallel alignment of the particles (Figure 6.1-e), with the direction of alignment being in line with the center of the droplet. The observed radial alignment is most likely a result of hydrodynamic drag forces exerted on the cellulose nanocrystals by the water moving radially outward upon evaporation of the droplet.

6.5. Conclusions

In closing, the demonstrated radial alignment of rod-like nanoparticles in dried droplets represents new evidence for the occurrence of a radial outward flow in droplets upon drying. Our results further demonstrate the utility of rod-like nanoparticles in the study of droplet hydrodynamics.

6.6. Acknowledgements

The authors gratefully acknowledge generous scholarship support for F. N. by the Mexican Secretariat of Public Education (SEP) through its Professional Development for Teachers

program (PROMEP). This project was further supported by the National Research Initiative of the USDA Cooperative State Research, Education and Extension Service, grant number 2005-35504-16088, and by the National Science Foundation under grant numbers CHE-0724126 and DMR-0907567. Additional support from OMNOVA, Inc. and Tembec, Inc. is also acknowledged.

6.7. References

1. Tekin, E.; Smith, P. J.; Schubert, U. S. Inkjet printing as a deposition and patterning tool for polymers and inorganic particles. *Soft Matter* **2008,** 4, 703-713.
2. McHale, G. Surface Free Energy and Microarray Deposition Technology. *Analyst* **2007,** 132.
3. Picknett, R. G.; Bexon, R. The evaporation of sessile or pendant drops in still air. *Journal of Colloid and Interface Science* **1977,** 61, 336-350.
4. Deegan, R. D.; Bakajin, O.; Dupont, T. F.; Huber, G.; Nagel, S. R.; Witten, T. A. Capillary flow as the cause of ring stains from dried liquid drops. *Nature* **1997,** 389, 827-829.
5. Beck-Candanedo, S.; Roman, M.; Gray, D. G. Effect of reaction conditions on the properties and behavior of wood cellulose nanocrystal suspensions. *Biomacromolecules* **2005,** 6, 1048-1054.

Chapter 7

Fabrication of Cellulose Micropatterns on Glass Substrates by Inkjet Printing of Cellulose Nanocrystal Suspensions

Fabrication of Cellulose Micropatterns on Glass Substrates by Inkjet Printing of Cellulose Nanocrystal Suspensions

Fernando Navarro and Maren Roman

Macromolecules and Interfaces Institute and Department of Wood Science and Forest Products, 230 Cheatam Hall, Virginia Polytechnic Institute and State University, Blacksburg, Virginia, 24061, United States of America.

7. 1. Abstract

Inkjet printing has generated considerable interest as a technique for the patterning of functional materials in the liquid phase onto a substrate. Despite its high promise, the phenomena associated with inkjet printing remain incompletely understood. In the present paper, we investigated inkjet printing of cellulose nanocrystals (CNCs) as a possible method for the fabrication of cellulose micropatterns. Aqueous CNC suspensions were printed in different patterns onto glass substrates with a commercial, piezoelectric drop-on-demand inkjet printer. At low CNC concentrations (0.05 wt %), inkjet-deposited droplets formed ring-like residues due to the "coffee drop effect". The "coffee drop effect" could be suppressed by use of higher CNC concentrations. The resulting dot-like droplet residues exhibited Maltese cross interference patterns between crossed polarizers, indicating a radial orientation of the birefringent CNCs in these residues. The degree of definition of the micropatterns depended strongly on the surface properties of the glass substrates. Well-defined micropatterns were obtained on aqua regia-cleaned substrates. In addition to the surface free energy and polarity, other factors seemed to play a role in the formation of the inkjet-printed micropatterns. If these factors can be identified and controlled, inkjet deposition of CNCs could become an attractive method for the fabrication of cellulose micropatterns.

Key words: Cellulose nanocrystals, inkjet printing, micropatterning, coffee drop effect, radial alignment, Maltese cross interference pattern.

7. 2. Introduction

The ability to generate microscale material patterns on flat substrates, brought about by the advent of photolithography, has revolutionized the electronics industry.[1] In recent years, resolution- and material-related limitations of photolithography combined with a general technology push towards miniaturization have spurred the development of non-photolithographic methods for the fabrication of two- and three-dimensional micro- and nanostructures.[2] Among these alternative methods, inkjet printing has generated considerable interest due to its low cost, ease of controllability, versatility, contact free nature, and potential for high throughput.[3] It has been explored as a tool to fabricate organic and inorganic electronic devices, 3D ceramic structures, and bio-microarrays by printing polymer solutions or colloidal suspensions of ceramic, metal, and polymer particles.[4-8] Despite its high promise as a technique for the deposition and patterning of functional materials in the liquid phase onto a substrate, the phenomena associated with inkjet printing of colloidal systems remain incompletely understood. Important factors that determine the quality of inkjet printed micropatterns of nanoparticles include the viscosity of the colloidal suspension, the wetting properties of the substrate with respect to the colloidal suspension, and the molecular interactions between the nanoparticles and the substrate.

Cellulose, a linear polysaccharide of β-glucose, has recently attracted interest as a substrate for self-assembled lipid monolayers,[9] native cellular membranes,[10, 11] antibody microarrays,[12] and cell growth.[13] Several different methods to generate cellulose micropatterns have been reported.[9, 11, 14-16] Most of these methods are based on soluble cellulose derivatives and either require a lithography mask[9, 11] or do not provide much control over the pattern itself.[14-16] In the present paper, we investigated inkjet printing of cellulose nanocrystals (CNCs) as a possible method for the fabrication of cellulose micropatterns. CNCs, also referred to as cellulose whiskers, are elongated, crystalline cellulose particles with cross-sectional dimensions of less than 100 nm and lengths of up to several micrometers. They are generally produced by acid hydrolysis of purified plant-, algae-, microbial-, or animal-based cellulose. The objectives of this study were to determine the factors that govern the morphology of inkjet-deposited droplet residues and micropatterns of CNCs on glass substrates and to evaluate inkjet printing of CNCs as a method for the fabrication of cellulose micropatterns.

7. 3. Experimental section

7. 3. 1. CNC preparation

Lap sheets of dissolving-grade softwood sulfite pulp (Temalfa 93 A-A), kindly provided by Tembec, Inc., were cut into small pieces and milled (Thomas Wiley mini mill) to pass a 60-mesh screen. The milled pulp was hydrolyzed for 60 min at 50 °C with sulfuric acid (Fisher Scientific, 97.1%, Certified ACS Plus), diluted to 64 wt % with deionized (DI) water (Millipore Direct-Q 5, 18.2 MΩ·cm), at an acid-to-pulp ratio of 10 mL/g. Hydrolysis was stopped by 10-fold dilution of the reaction mixture with cold (4 °C) DI water. The suspension was centrifuged (Thermo IEC Centra-GP8R) for 10 min at 4500 rpm and 25 °C. The sediment was redispersed in DI water by shaking and the suspension was centrifuged again as described above. The sediment was again redispersed in DI water by shaking and the suspension was dialyzed (Spectra/Por 4 dialysis tubing) against DI water for several days until the pH of the dialysate remained constant. For the disruption of potential CNC aggregates, the CNC suspension was sonicated for 10 min at 40% output using a 500-Watt ultrasonic processor (Sonics Vibra-Cell VC-505). After sonication, the suspension, with a final concentration of 1.29 wt %, was filtered through a polyvinylidene fluoride syringe filter, having a pore size of 0.45 μm (Whatman GD/XP). CNC suspensions of lower concentration were prepared from the stock suspension by dilution with DI water.

7. 3. 2. Substrate treatments

The substrates used in this study were 3 in. x 1 in. soda–lime–silica (SLS) glass microscope slides (T & Q Industries, Pearl Brand, "pre-cleaned"). The glass slides were either used as received, after removal of any loose particles from their surface by a stream of nitrogen, or subjected to one of the following treatments:

Soap cleaning. A 4 wt % solution (pH > 9.5) of Alconox in DI water was degassed for 30 min at 45 ºC in an ultrasonic cleaner (Bransonic, model B3510-DTH) and then poured into a glass staining dish loaded with glass slides. The staining dish was placed into the ultrasonic cleaner and subjected to ultrasound for 10 min at 45 °C. Next, the soap solution in the staining dish was

replaced with DI water and the ultrasound treatment was repeated. The slides were washed twice more with DI water and an ultrasound treatment of 5 and 2 min, respectively. Finally, the slides were dried in a stream of nitrogen and stored in a slide storage box until use.

Aqua regia cleaning. A 3:1 mixture by volume of hydrochloric acid (Fisher, 37.4% purity) and nitric acid (Fisher, 69.5% purity) was poured into a glass staining dish loaded with glass slides. The staining dish was covered and left undisturbed for 30 min. Then, the acid mixture was replaced with DI water and the slides were washed three times in an ultrasonic cleaner as described above. Finally, the slides were dried in a stream of nitrogen and stored in a slide storage box until use.

Solvent cleaning. Four glass slides at a time were carefully placed with minimal contact into the extraction tube of a Soxhlet apparatus. A 1:1 mixture by volume of ethanol (Sigma-Aldrich, anhydrous, 200 proof, 99.5+% purity) and chloroform (Fisher, ≥ 99.8% purity) was brought to a boil in the still pot. After four reflux cycles, the glass slides were placed into a glass staining dish and rinsed three times with DI water in an ultrasonic cleaner as described above. Finally, the slides were dried in a stream of nitrogen and stored in a slide storage box.

Polyethylene glycol grafting. A 10 wt % KOH (Acros Organics, pellets, 85 % purity) solution was poured into a glass staining dish loaded with glass slides. The staining dish was covered and left overnight undisturbed. The next morning, the KOH solution was replaced with DI water and the staining dish was placed into an ultrasonic cleaner and subjected to ultrasound for 10 min at 45 °C. The glass slides were dried in a stream of nitrogen and placed for 30 min into a staining dish filled with a 2.5 vol % aqueous solution of aminopropyltriethoxy silane (Acros Organics, 99 % purity). The glass slides were rinsed sequentially with DI water and absolute ethanol (Sigma Aldrich, anhydrous, 200 proof) and dried in a vacuum oven for 24 h at 80 °C. Next, the glass slides were immersed into a 0.1 M aqueous sodium carbonate (Sigma Aldrich, anhydrous, ≥ 99.9 % purity) solution containing 2.5 wt % glutaraldehyde (Acros Organics, 50 wt % in H_2O). After 2 h, the glass slides were removed and immersed into a 0.5 wt % aqueous solution of bis(3-amino propyl)-terminated poly(ethylene glycol) (Sigma Aldrich, 1.5 kD mol. weight, pure).

After 2 days, the slides were dried in a stream of nitrogen and stored in a slide storage box until use.

7. 3. 3. Conductometric titration

Twenty five milliliters of a 1 wt % CNC suspension was titrated under nitrogen and magnetic stirring with 0.01 N NaOH. The conductivity at each step was measured with an S47 SevenMulti pH/conductivity meter (Mettler-Toledo International, Inc.) equipped with an Inlab 730 conductivity probe (Mettler-Toledo International, Inc.).

7. 3. 4. Viscosity measurement

The steady-state shear viscosities of CNC suspensions with different concentrations between 0.008 and 1 wt % were measured at 25 °C for different shear rates between 3 and 300 1/s with a TA Instruments AR-1000 rheometer equipped with a stainless steel cone-and-plate fixture (40 mm diameter, 1.59°).

7. 3. 5. ζ-potential measurement

ζ-potentials were calculated from streaming potentials with the equation given by Sides *et al.*[17] For measurement of the streaming potential, untreated glass slides were cut into disks of 1 in. diameter prior to treatment. The treated and dried glass disks were stored in polystyrene Petri dishes with their top surfaces marked. Care was taken to analyze the glass surface that was not in contact with the Petri dish. The streaming potentials of the glass disks were measured with a ZetaSpin apparatus (Zetametrix Inc.) by the rotating disk method of Sides *et al.*[17] Measurements were done at 25 °C in 1 mM KCl solution, prepared by dilution of a 3 M standard (Mettler-Toledo, GMbH) with DI water, with a spinning speed of 4000 rpm and a distance of 1 mm between the electrode and the glass surface. Between measurements, the pH was lowered by approximately 0.5 each time from an initial value of 5.8 to a final value of about 3 by addition of 50 mM HCl. In a separate run, the pH was raised between measurements by approximately 0.5

each time from an initial value of 5.8 to a final value of about 9 by addition of 50 mM KOH. Reported ζ-potentials are means of five measurements with three cycles each.

7. 3. 6. Inkjet printing

Printing of CNC suspensions was done with an Epson Stylus Photo R280 piezoelectric, drop-on-demand inkjet printer and refillable, clear, spongeless cartridges (Inkproducts.com), both shown in Figure 7.1. We chose a piezoelectric printer for this study to avoid potential heat damage to the CNCs by a thermal inkjet print head. The glass substrates were mounted onto the printer's CD tray for printing as shown in Figure 7.1. To avoid contact between printer components and the top surface of the glass substrates, we removed several paper feed rollers, clamps, and springs from the path of the glass substrates.

(a) *(b)*

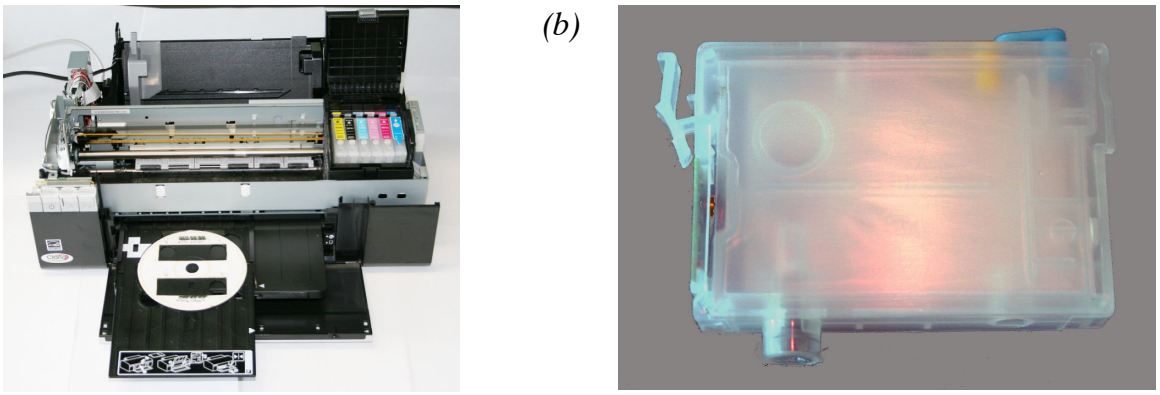

Figure 7.1. Epson stylus photo R280 inkjet printer (a) and one of the refillable, spongeless, inkjet cartridge (b) used for CNC micropatterning. Image (a) also shows the CD tray and the cardboard mount used as a glass substrate holder.

Four of the six cartridges of the CcMmYK color model, used by the Epson R280 printer, namely yellow (Y), light cyan (c), black (K), and light magenta (m), were identified as individually addressable and filled with CNC suspensions. The remaining two cartridges, cyan (C) and

magenta (M), were filled with DI water. Printing was done from the individually addressable cartridges by selection of one of the primary colors of the CMYK color model, *e.g.* 100% yellow. For printing, three different micropatterns, illustrated in Figure 7.2, were designed with Corel Draw software (v.X4, Corel Corporation).

Inkjet printers use industry standards like the International Color Consortium (ICC) color profiles to convert color data between native device color spaces and device independent color spaces. Often, color management by these profiles involves the mixing of ink from different cartridges to achieve a match between the color gamuts of the display and the printer.[18, 19] Therefore, printing was done with the ICC color profile and the color enhancement options turned off in the Corel Draw and printer software.

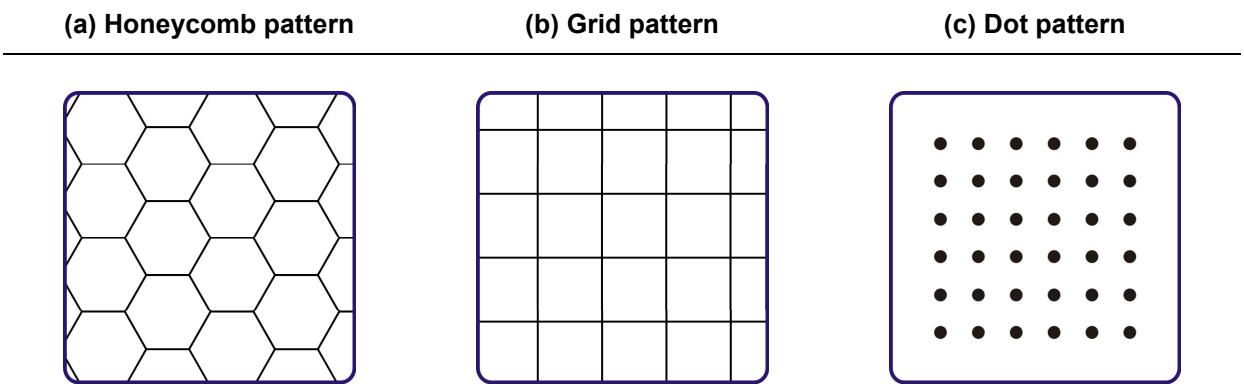

Figure 7.2. Patterns used for the inkjet printing of CNCs. The honeycomb and grid patterns used a line width of 25 μm and line spacings of 50–500 μm. The dot patterns used dot diameters of 10–100 μm and a dot spacing of 100-500 μm.

7. 3. 7. Atomic force microscopy (AFM)

AFM images were acquired with an Asylum Research MFP-3D-Bio atomic force microscope mounted onto an Olympus IX 71 inverted fluorescence microscope and Olympus OMCL-AC160TS silicon probes (nominal tip radius < 10 nm, spring constant 42 N/m). All the images were taken in intermittent contact mode in air with a scan frequency of 1 Hz, 512 scans, and 512 points/scan.

7. 3. 8. Scanning electron microscopy (SEM)

Because glass substrates are not electrically conductive, silicon wafers were used as substrates for the acquisition of SEM images of inkjet-printed droplet residues. Silicon wafers were cut into 1 cm x 1 cm pieces. The pieces were immersed into a 4:1:1 mixture by volume of DI water, hydrochloric acid (Fisher, 37.4% purity), and hydrogen peroxide (Fisher, 30%) at a temperature of 70 °C. After 15 min, the pieces were retrieved, rinsed with DI water, and dried in a stream of nitrogen. Printing onto the silicon substrates was done as described above. The samples were coated with a thin layer of gold prior to imaging. SEM images were acquired with a Zeiss LEO 1550 Schottky field-emission scanning electron microscope.

7. 3. 9. Polarized-light microscopy

Polarized-light micrographs of inkjet-deposited droplet residues and micropatterns were recorded with a Canon EOS 20D SLR camera mounted onto a Zeiss Axioskop 40 A POL polarized-light microscope.

7. 4. Results and discussion

7. 4. 1. Properties of the CNCs and CNC suspensions

The length, width, and thickness distributions of the CNCs were determined in a previous study, reported elsewhere.[20] The mean and median values are listed in Table 7.1.

Table 7.1. Statistical measures of the length, width, and thickness distributions of the CNCs

Dimension	Mean ± SE (nm)	Median ± SE (nm)	SD (nm)
Length	115.6 ± 2.1	89.5 ± 2.6	82.0
Width	13.3 ± 0.2	12.1 ± 0.2	7.0
Thickness	4.3 ± 0.1	4.3 ± 0.1	1.2

CNCs prepared by sulfuric acid hydrolysis have sulfate groups on their surface, which are negatively charged in neutral and basic aqueous media and stabilize the CNCs in suspension.[21-23] The sulfate group density of the CNCs was measured by conductometric titration. A typical conductometric titration curve is shown in Figure 7.3. The first section of the titration curve, showing a decrease in conductivity, is due to the neutralization of the sulfate groups on the surface of the CNCs. The second section, showing an increase in conductivity, is due to the addition of excess titrant (NaOH).

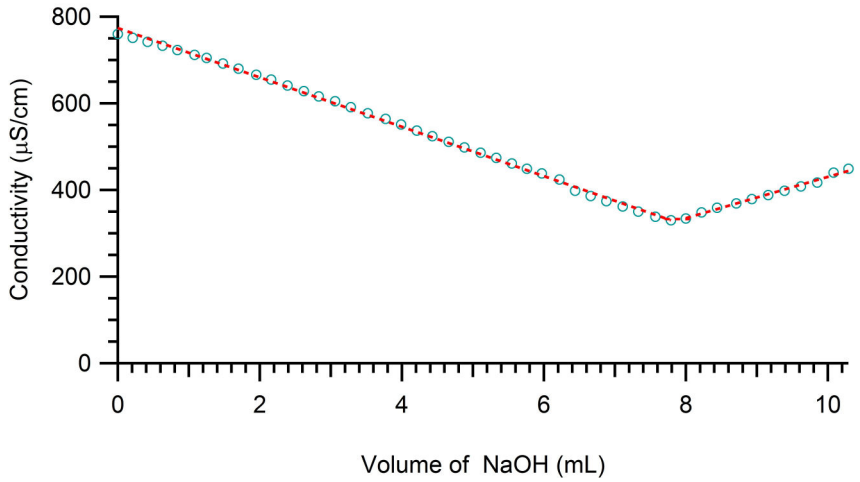

Figure 7.3. Conductometric titration curve of a CNC suspension.

The sulfate group density of the CNCs, calculated from the equivalence point of the titration, was 308 mmol/kg or 0.91 e/nm^2, assuming a density of 1.6 g/cm^3 [24] and a tabular morphology with a length, width, and thickness of 89.5, 12.1, and 4.3 nm, respectively. We used the medians for this calculation because the length and width distributions were non-normal.[20] For non-normal distributions the median is a better indicator of central tendency than the mean. The obtained value is more than twice the sulfate group density reported by Beck-Candanedo *et al.* for similar hydrolysis conditions (0.38 e/nm^2).[25] These authors assumed a cylindrical morphology and used the mean length and thickness for the calculation. Using the length and thickness means and assuming a cylindrical morphology, we obtained a sulfate group density of 0.31 e/nm^2, which compared reasonable well with the value of Beck-Candanedo *et al.*

The printer that was used in this study could tolerate ink viscosities of up to 20 mPa. A higher viscosity could result in clogging of the print head nozzles. Figure 7.4 shows the viscosity of CNC suspensions with different concentrations as a function of shear rate. At concentrations of up to 0.25 wt %, the CNC suspensions were Newtonian fluids with a shear-independent viscosity. However, at concentrations above 0.25 wt %, the CNC suspensions showed shear thinning behavior. This observation is in accordance with previous results published by Araki et al.,[26] who attributed the shear-thinning behavior of CNC suspensions to flow-induced particle orientation. The viscosity of the 1 wt % suspension approached 20 mPa at low shear rates. Therefore, 1 wt % was considered the maximum CNC concentration that could be used without risking damage to the printer.

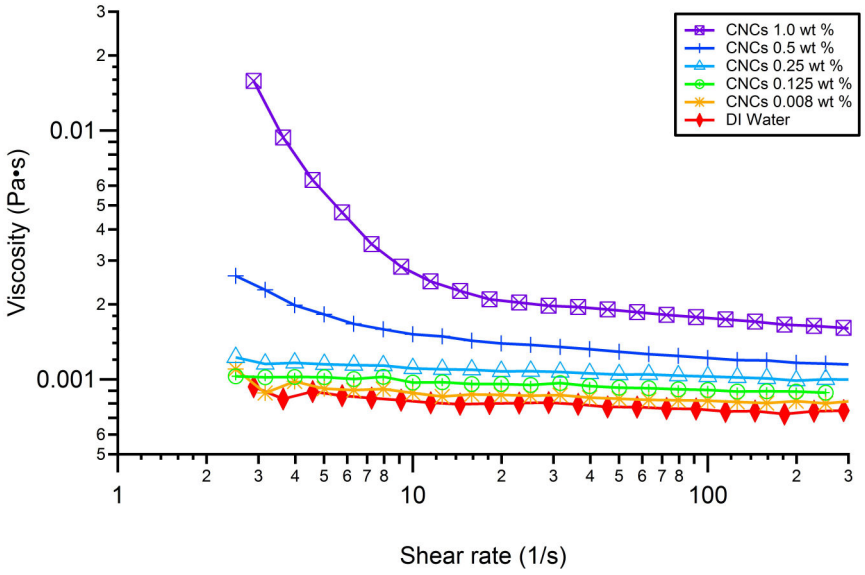

Figure 7.4. Viscosity of CNC suspensions with different concentrations as a function of shear rate.

7. 4. 2. Surface properties of the substrates

The surface properties of the untreated, soap-cleaned, aqua regia-cleaned, and solvent-cleaned glass substrates were determined in a previous study, reported elsewhere.[27] The surface properties of the PEG-grafted glass substrate were determined with the same methods used in the previous report.[27] The surface properties of the glass substrates are listed in Table 7.2.

The soap-cleaned glass substrate had the highest surface free energy, most polar surface character, and highest ζ-potential, in absolute terms. These properties were attributed to a large number of silanol groups on the substrate's surface.[27] The PEG-grafted glass substrate had the lowest surface free energy and least polar surface character of the glass substrates, which could be explained by the lower polarity of C–C, C–H, and C–O bonds, compared to Si–O bonds.

Table 7.2. Surface properties of the glass substrates[a]

Substrate	RMS surface roughness (nm)[b]	Surface free energy			ζ-potential (mV)[c]
		γ_S (mJ/m^2)	γ_S^p/γ_S	γ_S^d/γ_S	
Untreated	0.69 ± 0.01	53.40	0.67	0.33	–105.2 ± 0.2
Soap-cleaned	0.63 ± 0.01	59.62	0.70	0.30	–448.5 ± 2.9
Aqua-regia cleaned	0.36 ± 0.01	52.92	0.62	0.38	–392.6 ± 0.9
Solvent-cleaned	1.02 ± 0.02	46.08	0.51	0.49	–145.6 ± 0.7
PEG	4.80 ± 0.14[d]	29.78[d]	0.27[d]	0.73[d]	not available

[a] Source: Ref 27, [b] root-mean-square surface roughness of 1 μm by 1 μm areas, [c] in DI water, [d] Determined as described in ref 27

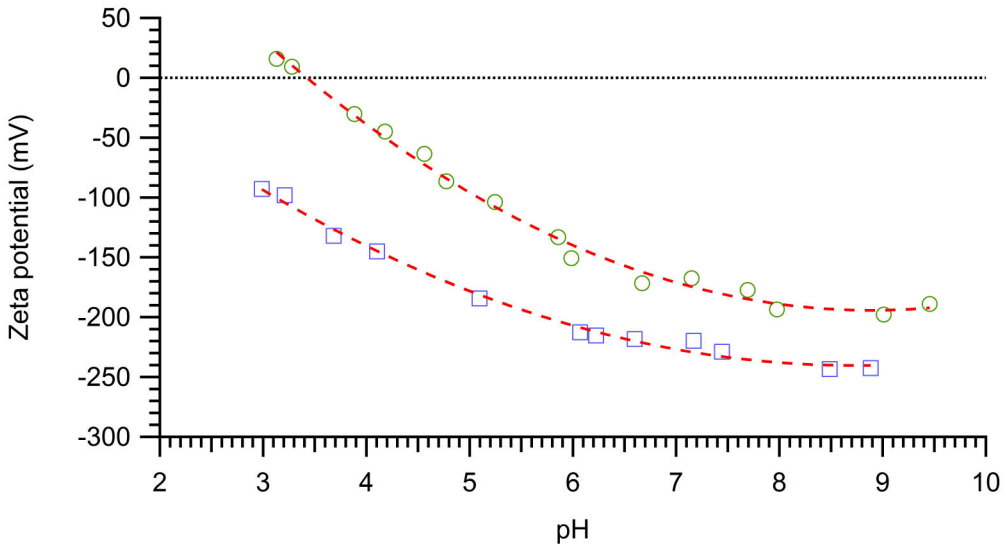

Figure 7.5. ζ-potentials of the soap-cleaned (□) and aqua regia-cleaned (○) glass substrates in 1 mM KCl solution as functions of pH. Data points are means of five measurements with three cycles each. Error bars are omitted for clarity.

The negative ζ-potential of glass substrates in contact with DI water is due to the dissociation of surface silanol groups. Because CNC suspensions are acidic, a glass surface in contact with a CNC suspension will have fewer dissociated silanol groups than a glass surface in contact with

DI water. To assess the effect of the acidity of CNC suspensions on the surface charge of the glass substrates, the ζ-potentials of the two substrates with the highest ζ-potentials, in absolute terms, were measured at different pH values. Figure 7.5 shows the ζ-potentials of the soap- and aqua regia-cleaned glass substrates in 1 mM KCl solution as functions of pH.

As expected, the ζ-potential became less negative with decreasing pH, from an initial pH of 5.8, because of the protonation of dissociated silanol groups. The ζ-potential of the aqua regia-cleaned glass slide crossed the *y*-axis at approximately pH 3.4, representing the isoelectric point of the substrate. Consequently, at a pH below 3.4, the aqua regia-cleaned slide would be neutral or slightly positively charged. The pH of the CNC suspensions was below 3.4 at CNC concentrations above 0.125 wt %. Therefore, at these CNC concentrations, attractive forces should dominate the interactions between the CNCs and the aqua regia-cleaned substrates. The ζ-potential of the soap-cleaned slide remained negative even at low pH. Therefore, repulsive electrostatic forces should dominate the interactions between the CNCs and the soap-cleaned substrates. The ζ-potential of both substrates became slightly more negative with increasing pH, from an initial pH of 5.8, but seemed to reach a limit at about pH 8. This behavior could be explained by the complete dissociation of all accessible surface silanol groups at that pH. Similar ζ-potential curves were reported for silica surfaces by Scales *et al.*[28] and for glass surfaces by Gu *et al.*[29]

7. 4. 3. Morphology of inkjet-deposited droplet residues

Figure 7.6 shows the droplet residue pattern obtained by printing a 0.76 wt % CNC suspension into a dot pattern (Figure 7.2-c) with dot diameters of 70 μm and a dot spacing of 280 μm onto an untreated glass slide. A regular array of ring-like residues of 68-74 μm in diameter can be observed. The positional offset of the residues is due to the inaccuracy of the printer with regard to droplet placement at single droplet print resolutions. Smaller rings with approximate diameters of 25 μm can be seen to the right of many larger rings (see inset in Figure 7.6). These smaller residues could be a result of satellite drop formation. Satellite drops are formed when the liquid thread exiting the print head nozzle breaks up into a primary drop and one or more satellite drops.

In commercial applications, this undesirable effect is controlled through ink properties (viscosity and surface tension) and system parameters (nozzle design, waveform of piezo driving signal).[30] The formation of satellite drops during inkjet printing of CNC suspensions could potentially be avoided through addition of surfactants and/or glycerin (to increase viscosity).

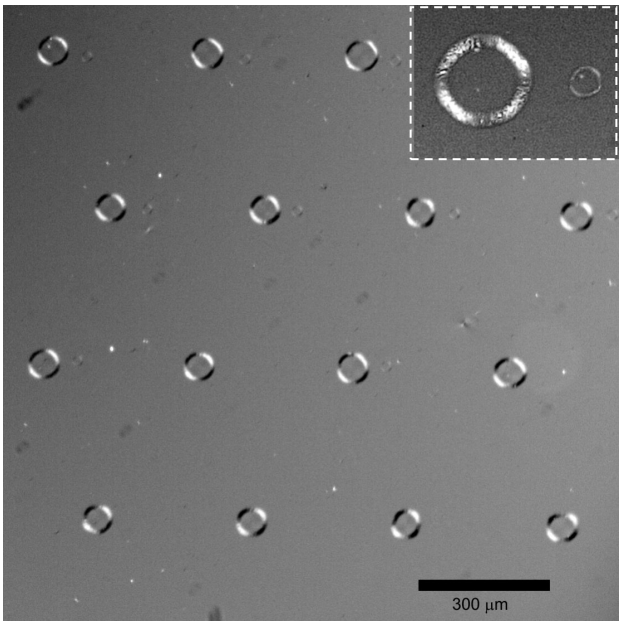

Figure 7.6. Polarized-light micrograph of the droplet residue pattern obtained by printing a 0.76 wt % CNC suspension into a dot pattern with dot diameters of 70 μm and a dot spacing of 280 μm onto an untreated glass slide. The inset shows one of the residues and its satellite at a higher magnification.

The formation of ring-like, as opposed to dot-like, droplet residues is a common phenomenon known as the "coffee drop effect", observed when drops containing dispersed solids evaporate on a solid substrate.[31, 32] The drying of a droplet deposited on a solid surface can follow any of the two following mechanisms: (a) It can keep a constant contact angle and decrease in size until complete evaporation of the liquid component, or (b) it can maintain a constant diameter by varying its contact angle and decreasing its height upon drying. The latter case is more likely to occur and requires that the contact line, *i.e.* the line between wet and dry substrate, of a drying drop be pinned to its initial position as a result of surface roughness or chemical heterogeneities.

Pinning of the contact line results in a type of capillary flow from the center of the drop to its edge upon evaporation of the liquid. The resulting outward flow carries any dispersed material to the edge of the drop, leading to dense deposits along its perimeter.

Figure 7.7 compares AFM images of inkjet-deposited droplet residues from a dilute (0.05 wt %) and more concentrated (0.76 wt %) CNC suspension on soap- and aqua regia-cleaned glass substrates. The droplet residues from the more dilute suspension (Figures 7.7-a and 7.7-b) showed the coffee drop effect, leading to ring formation. In the case of the soap-cleaned glass substrate (Figure 7.7-a), all solid matter present in the droplet had been moved to the periphery, whereas in the case of the aqua regia-cleaned substrate (Figure 7.7-b), a thin layer of particles covering the center of the droplet residue, was observed. The difference in the appearance of the two droplet residues suggested that the soap-cleaned glass slide exerted stronger repulsive forces upon the CNCs than the aqua regia-cleaned glass slide, in accordance with the ζ-potential results.

At higher suspension concentrations, the coffee drop effect was less pronounced (Figures 7.7-c and 7-d). The higher solid content in the droplet might result in an increased width of the ring to the extent that the ring covers the entire area of the residue. Another explanation for the more uniform distribution of particles in the droplet residues from the more concentrated suspension could be a reduced radial flow inside the droplet due to an almost 5-fold higher viscosity with respect to that of the more dilute suspension (4.49×10^{-3} mPa·s versus 0.94×10^{-3} mPa·s).

The large, elongated particles, visible in the droplet residues from the more concentrated suspension (Figures 7.7-c and 7.7-d) but not observed in the residues from the more dilute suspension (Figure 7.7-a and 7.7-b), are most likely aggregates of CNCs formed during drying of the droplets or as a result of the high shear forces upon ejection through the print head nozzle.

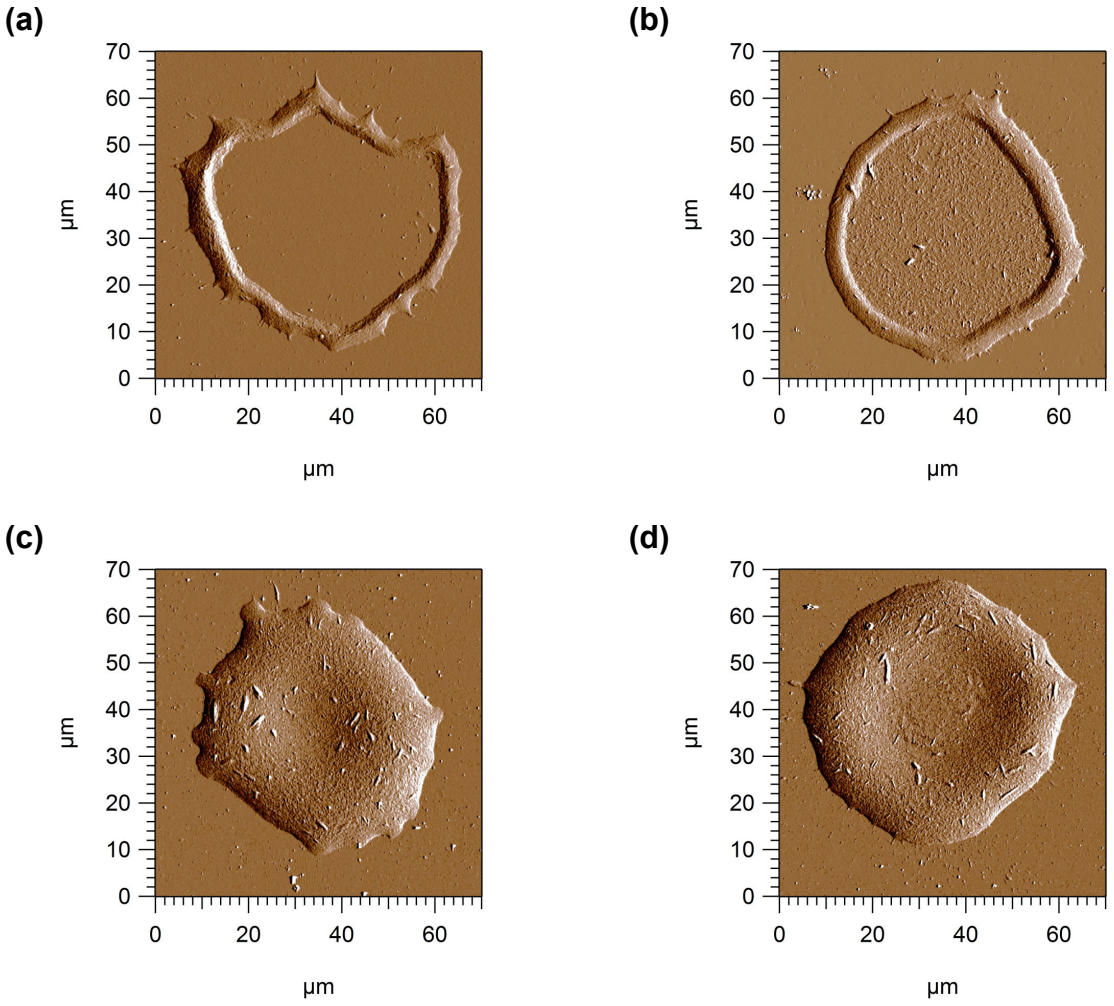

Figure 7.7. AFM amplitude images of inkjet-deposited droplet residues from two different CNC concentrations (a, b: 0.05 wt %, c, d: 0.76 wt %) and on two different glass substrates (a, c: soap-cleaned, b, d: aqua regia-cleaned). The z-scale for the amplitude images is 20 nm.

The morphology of inkjet-deposited droplet residues was also analyzed by SEM. Figure 7.8 shows SEM images at different magnifications of inkjet-deposited droplet residues from a dilute (0.05 wt %) and more concentrated (0.76 wt %) CNC suspension on silicon substrates. As was the case for the glass substrates, the droplet residue from the more dilute suspension showed the coffee drop effect (Figure 7.8-a) whereas the residue from the more concentrated suspension did not (Figure 7.8-c). At higher magnification (Figure 7.8-b), the image of the ring-like residue

showed some CNCs in the center of the residue (right side of the image), suggesting that the silicon substrate behaved more like the aqua regia-cleaned glass substrate than the soap-cleaned glass substrate. The higher-magnification image of the dot-like droplet residue (Figure 7.8-d) showed uniform coverage of the substrate with CNCs. The cracks that can be seen in the higher-magnification images are due to beam damage of the sample.

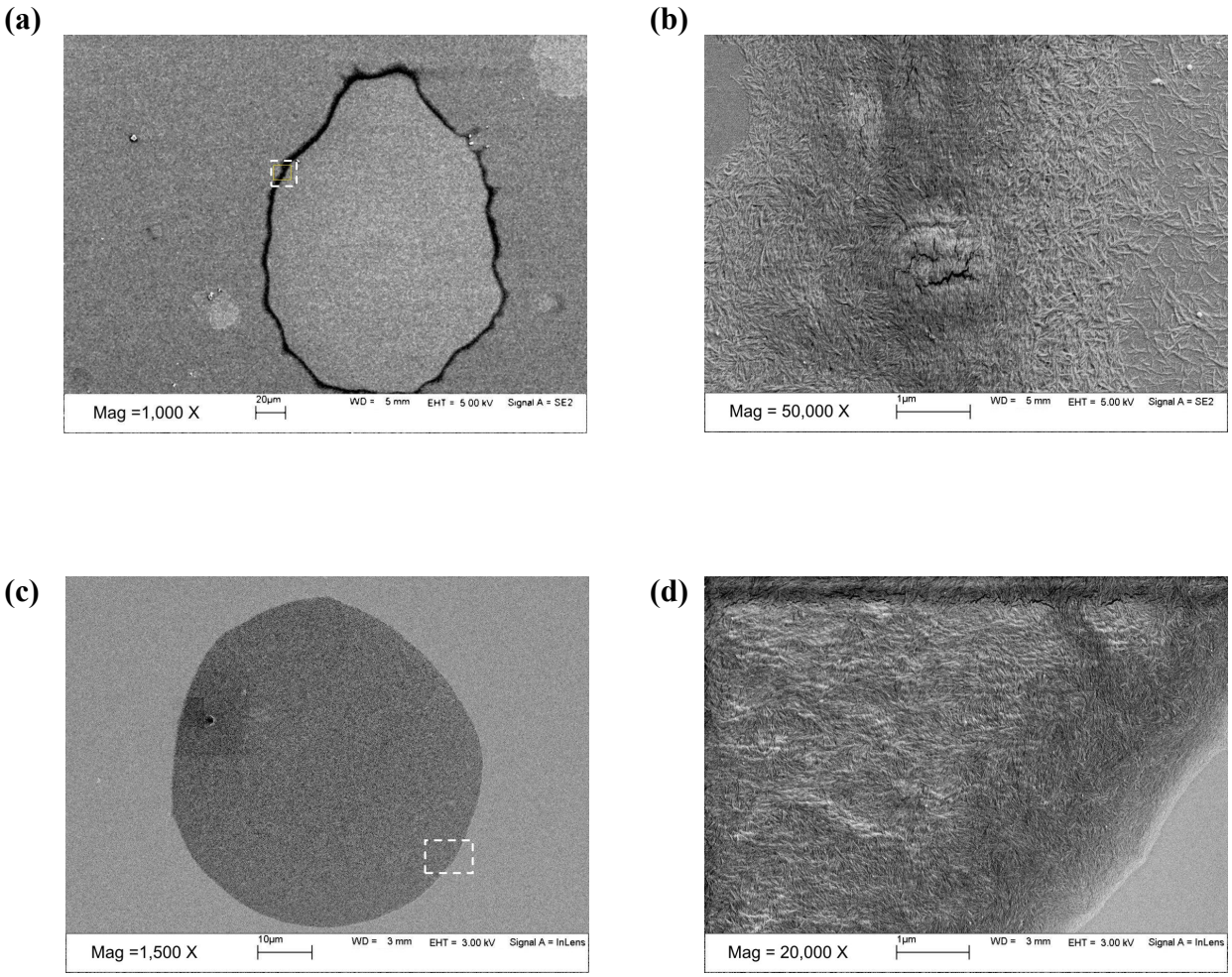

Figure 7.8. SEM micrographs of inkjet-deposited droplet residues from two different CNC concentrations (a, b: 0.05 wt %, c, d: 0.76 wt %) on silicon substrates.

Figure 7.9 shows a polarized-light micrograph of dot-like droplet residues obtained by printing a 1 wt % CNC suspension onto a soap-cleaned glass slide. Many of the residues showed a Maltese cross interference pattern, indicative for a radial symmetrical orientation of CNCs in the residues.[33] The radial alignment of CNCs in inkjet-deposit droplet residues represents unprecedented indirect evidence for a center-to-edge radial flow in drying droplets because it is most likely a result of shear stress induced alignment of the rod-like particles in the direction of flow.

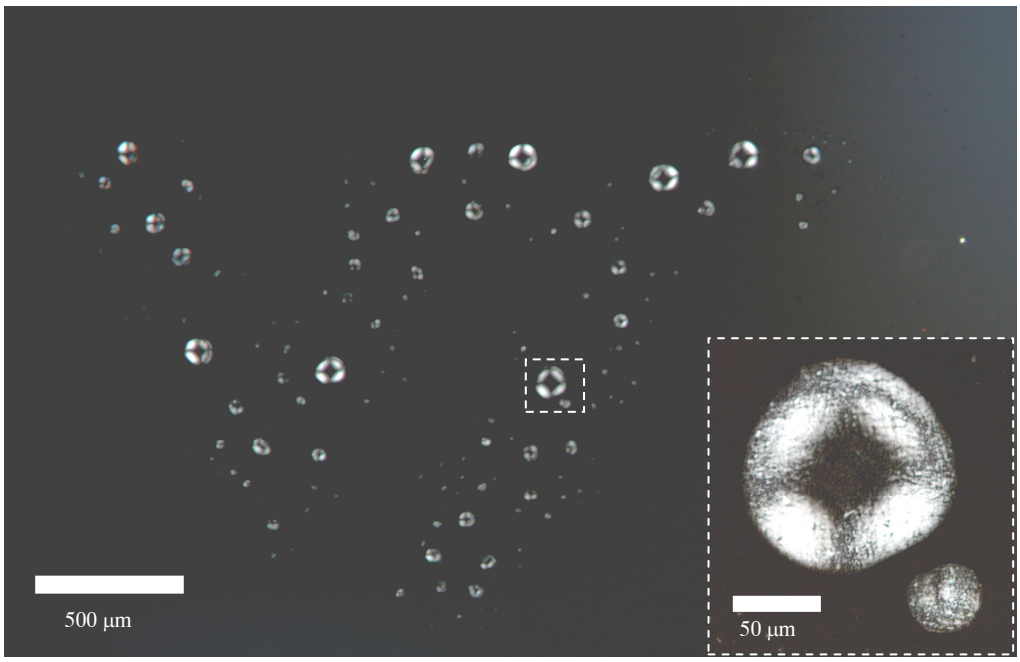

Figure 7.9. Polarized-light micrograph of inkjet-deposited droplet residues showing Maltese cross interference patterns due to radial alignment of the birefringent, elongated CNCs in the residues. The inset shows one of the residues at a higher magnification.

7. 4. 4. Morphology of inkjet-deposited micropatterns

In preliminary printing experiments, the degree of definition of the printed micropatterns was found to strongly depend on the spacing of the lines in the micropattern and the number of droplets ejected from the print head onto the same location on the substrate. The minimum line spacing for limited coalescence of droplets from adjacent lines was 200 μm. The number of droplets ejected from the print head onto a location on the substrate was controlled by the print quality settings in the printer software. The best results were obtained with the photo print quality option selected and the bi-directional printing option turned off.

Figures 7.10 and 7.11 show polarized-light micrographs of CNC grid and honeycomb patterns, respectively, on glass substrates with different surface properties. Inkjet printers control ink deposition in the vertical direction by moving the substrate forward and backward beneath the print head and in the horizontal direction by moving the print head left and right across the substrate. The micropatterns were designed to test the vertical and horizontal printing ability (grid pattern) and the diagonal printing ability (honeycomb pattern) of the printer.

The micropatterns on the untreated, soap-cleaned, aqua regia-cleaned, and solvent-cleaned glass substrates (Figures 7.10-a through 7.10-d and 7.11-a through 7.11-d) had a line spacing of 250 μm. The micropatterns on the PEG-grafted glass substrates (Figures 7.10-e and 7.11-e) were printed earlier during the study and had a line spacing of 450 μm.

As seen in Figures 7.10 and 7.11, the degree of definition of the micropatterns depended strongly on the surface properties of the substrate. The micropatterns on the soap-cleaned glass substrates (Figures 7.10-b and 7.11-b) exhibited extensive droplet coalescence. The soap-cleaned glass substrates had the highest surface free energy and most polar surface character of the substrates, promoting the spreading and coalescence of the aqueous droplets. The PEG-grafted substrates (Figures 7.10-e and 7.11-e), having the lowest surface free energy and least polar surface character as well as the highest RMS surface roughness, showed fairly well defined micropatterns with minimal droplet coalescence, due to the restriction of droplet spreading. A certain degree of droplet coalescence is, however, desired for the formation of continuous lines.

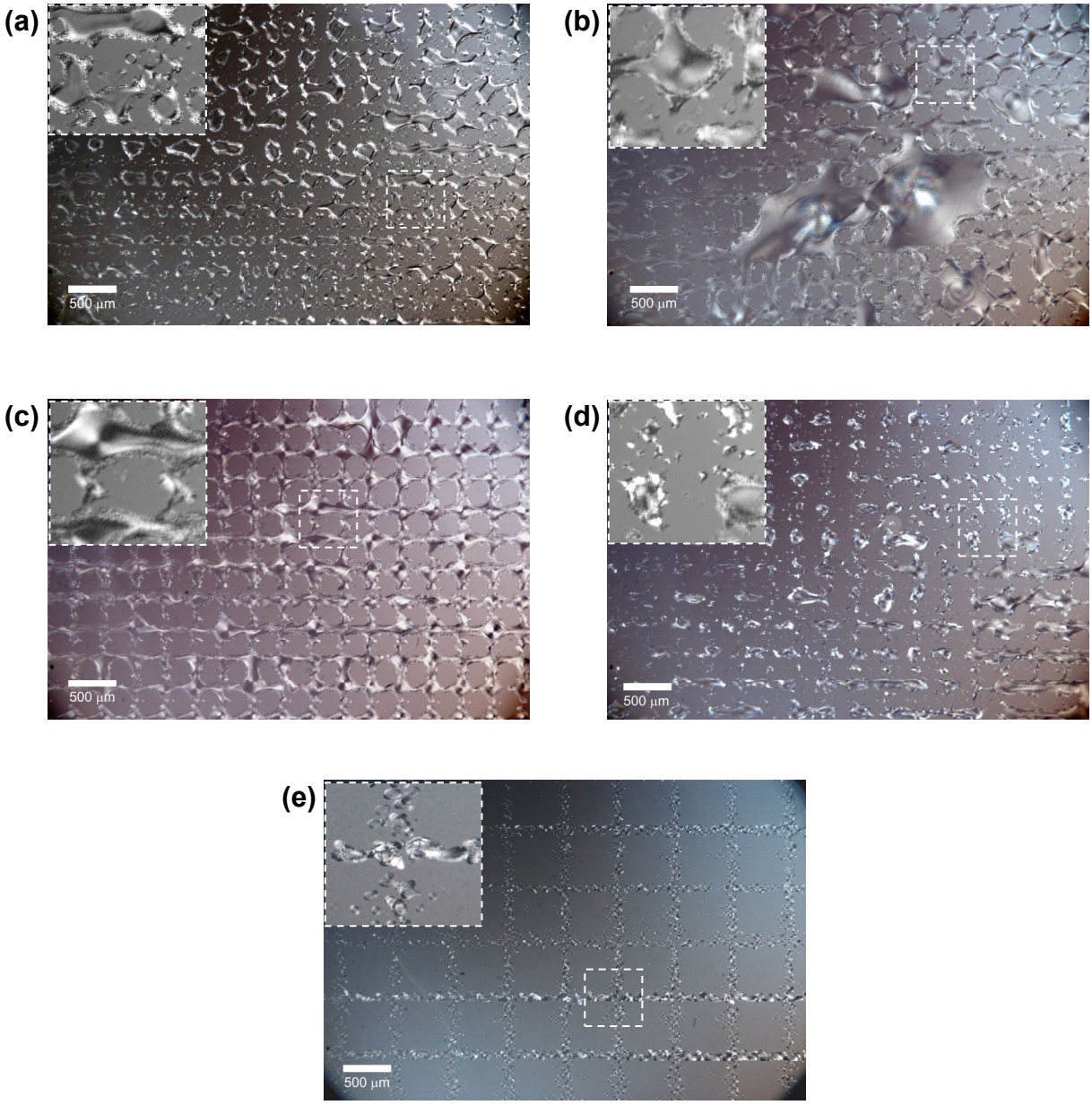

Figure 7.10. Polarized-light micrographs of inkjet-deposited CNC grid patterns on glass substrates with different surface properties: (a) untreated, (b) soap-cleaned, (c) aqua regia-cleaned, (d) solvent-cleaned, and (e) PEG-grafted. The line spacing was 250 μm in micrographs (a) through (d) and 450 μm in micrograph (e). Insets show selected regions at higher magnification.

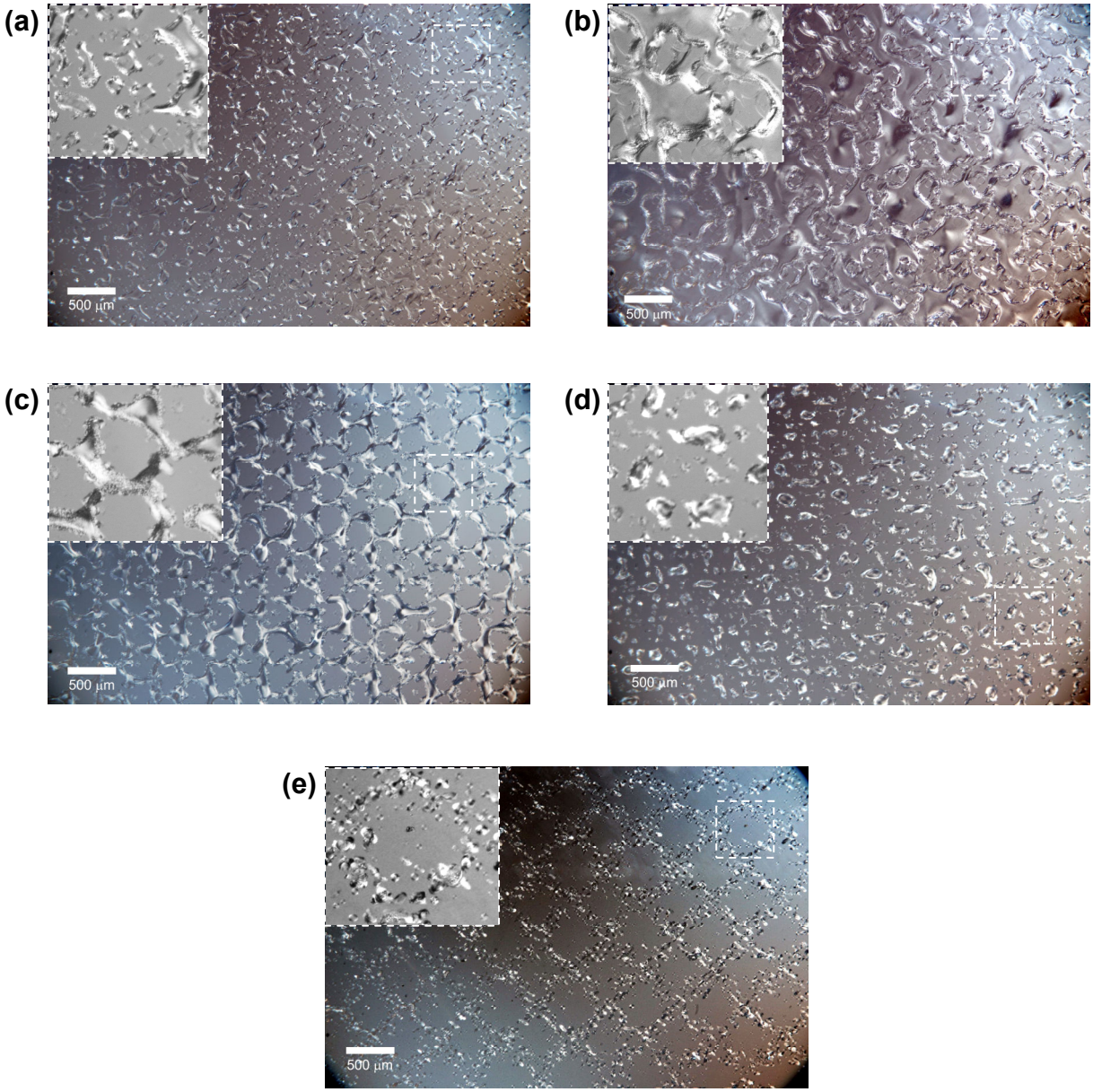

Figure 7.11. Polarized-light micrographs of inkjet-deposited CNC honeycomb patterns on glass substrates with different surface properties: (a) untreated, (b) soap-cleaned, (c) aqua regia-cleaned, (d) solvent-cleaned, and (e) PEG-grafted. The line spacing was 250 µm in micrographs (a) through (d) and 450 µm in micrograph (e). Insets show selected regions at higher magnification.

The best micropatterns with fairly well defined continuous lines were observed on the aqua regia-cleaned glass substrates (Figures 7.10-c and 7.11-c). These substrates had a surface free energy and polarity intermediate to those of the soap-cleaned and PEG-grafted substrates. The same was true for the untreated and solvent-cleaned glass substrates. Yet, these substrates exhibited poorly defined micropatterns. The observed differences between the micropatterns on the untreated, aqua regia-cleaned, and solvent-cleaned glass substrates suggested that factors other than the surface free energy and surface polarity played a role. Although not expected to play a major role, the RMS surface roughness of the aqua regia-cleaned substrates was significantly lower than those of the untreated and solvent-cleaned substrates. Probably more important were the differences in the surface chemical compositions of the substrates.[27]

The degree of definition of the honeycomb patterns (Figure 7.11) was overall lower than that of the grid patterns (Figure 7.10). The lower degree of definition of the honeycomb patterns indicated that droplet deposition for diagonal lines was less precise than droplet deposition for horizontal and vertical lines.

7. 5. Conclusions

The objectives of this study were to determine the factors that govern the morphology of inkjet-deposited droplet residues and micropatterns of CNCs on glass substrates and to evaluate inkjet printing of CNCs as a method for the fabrication of cellulose micropatterns. In light of the above results, the following conclusions can be drawn. Because of the “coffee drop effect”, inkjet-deposited droplets of dilute CNC suspensions form ring-like residues. The “coffee drop effect” can be suppressed and dot-like residues can be obtained by use of higher CNC concentrations.

The CNCs in dot-like residues are radially oriented as a result of shear-induced alignment of the elongated particles by the radial outward liquid flow during droplet drying. For the prevention of clogging of the print head nozzles, the concentration of the CNC suspension in the printer cartridge should not exceed 1 wt %. The molecular interactions between the CNCs and the substrate’s surface as well as the degree of definition of the printed micropatterns can be controlled by tailoring the surface properties of the substrate. A high surface free energy and

polarity promotes coalescence of the inkjet-deposited droplets, leading to poorly defined micropatterns. A low surface free energy and polarity, on the other hand, limits droplet coalescence and, thus, prevents the formation of continuous lines in the micropattern. In addition to the surface free energy and polarity, other factors seem to play a role in the formation of the inkjet-printed micropatterns. If these factors can be identified and controlled, inkjet deposition of CNCs could become an attractive method for the fabrication of cellulose micropatterns.

7. 6. Acknowledgements

This project was supported by the National Research Initiative of the USDA Cooperative State Research, Education and Extension Service, grant number 2005-35504-16088, and by the National Science Foundation under grant numbers CHE-0724126 and DMR-0907567. The authors also gratefully acknowledge the generous scholarship support for F. N. by the Mexican Secretariat of Public Education (SEP) through its Professional Development for Teachers Program (PROMEP). Furthermore, additional support from OMNOVA, Inc. and Tembec, Inc. are also acknowledged.

7. 7. References

1. Menard, E.; Meitl, M. A.; Sun, Y. G.; Park, J. U.; Shir, D. J. L.; Nam, Y. S.; Jeon, S.; Rogers, J. A. Micro- and nanopatterning techniques for organic electronic and optoelectronic systems. *Chemical Reviews* **2007,** 107, 1117–1160.
2. Gates, B. D.; Xu, Q. B.; Love, J. C.; Wolfe, D. B.; Whitesides, G. M. Unconventional nanofabrication. *Annual Review of Materials Research* **2004,** 34, 339–372.
3. Geissler, M.; Xia, Y. N. Patterning: Principles and some new developments. *Advanced Materials* **2004,** 16, 1249–1269.
4. Calvert, P. Inkjet printing for materials and devices. *Chemistry of Materials* **2001,** 13, 3299–3305.
5. Sirringhaus, H.; Shimoda, T. Inkjet printing of functional materials. *Mrs Bulletin* **2003,** 28, 802–803.

6. Schubert, U. S. Ink-jet printing of functional polymers and materials: A (future) key technology in polymer science. *Macromolecular Rapid Communications* **2005,** 26, 237–237.
7. Barbulovic-Nad, I.; Lucente, M.; Sun, Y.; Zhang, M. J.; Wheeler, A. R.; Bussmann, M. Bio-microarray fabrication techniques - A review. *Critical Reviews in Biotechnology* **2006,** 26, 237–259.
8. Yap, F. L.; Zhang, Y. Protein and cell micropatterning and its integration with micro/nanoparticles assembly. *Biosensors and Bioelectronics* **2007,** 22, 775–788.
9. Wiegand, G.; Jaworek, T.; Wegner, G.; Sackmann, E. Heterogeneous surfaces of structured hairy-rod polymer films: Preparation and methods of functionalization. *Langmuir* **1997,** 13, 3563–3569.
10. Tanaka, M.; Kaufmann, S.; Nissen, J.; Hochrein, M. Orientation selective immobilization of human erythrocyte membranes on ultrathin cellulose films. *Physical Chemistry Chemical Physics* **2001,** 3, 4091–4095.
11. Tanaka, M.; Wong, A. P.; Rehfeldt, F.; Tutus, M.; Kaufmann, S. Selective deposition of native cell membranes on biocompatible micropatterns. *Journal of the American Chemical Society* **2004,** 126, 3257–3260.
12. Ko, I. K.; Kato, K.; Iwata, H. Antibody microarray for correlating cell phenotype with surface marker. *Biomaterials* **2005,** 26, 687-696.
13. Yokota, S.; Kitaoka, T.; Wariishi, H. Biofunctionality of self-assembled nanolayers composed of cellulosic polymers. *Carbohydrate Polymers* **2008,** 74, 666-672.
14. Kasai, W.; Kondo, T. Fabrication of honeycomb-patterned cellulose films. *Macromolecular Bioscience* **2004,** 4, 17–21.
15. Kontturi, E.; Thüne, P. C.; Alexeev, A.; Niemantsverdriet, J. W. Introducing open films of nanosized cellulose – Atomic force microscopy and quantification of morphology. *Polymer* **2005,** 46, 3307–3317.
16. Kimura, T.; Kamioka, T.; Kuga, S. Filtration-Assisted Magnetic Micropatterning of Bacterial Cellulose. *Polymer Journal* **2007,** 39, 1199-1201.
17. Sides, P. J.; Newman, J.; Hoggard, J. D.; Prieve, D. C. Calculation of the streaming potential near a rotating disk. *Langmuir* **2006,** 22, 9765–9769.

18. Green, P.; Holm, J.; Li, W. Recent developments in ICC color management. *Color Research & Application* **2008,** 33, 444-448.
19. Gupta, M. R.; Garcia, E. K.; Stroilov, A. Learning custom color transformations with adaptive neighborhoods. *Journal of Electronic Imaging* **2008,** 17, 033005.
20. Chapter 4.
21. Dong, X. M.; Revol, J.-F.; Gray, D. G. Effect of microcrystallite preparation conditions on the formation of colloid crystals of cellulose. *Cellulose* **1998,** 5, 19–32.
22. Marchessault, R. H.; Morehead, F. F.; Koch, M. J. Hydrodynamic properties of neutral suspensions of cellulose crystallites as related to size and shape. *Journal of Colloid Science* **1961,** 16, 327–344.
23. Rånby, B. G. Aqueous colloidal solutions of cellulose micelles. *Acta Chemica Scandinavica* **1949,** 3, 649–650.
24. Ganster, J.; Fink, H. P. Physical constants of cellulose. In: Polymer Handbook; 4th ed.; Brandrup, J., Immergut, E. H., Grulke, E. A., Eds.; Wiley & Sons: New York, 1999; pp V/135–V/157.
25. Beck-Candanedo, S.; Roman, M.; Gray, D. G. Effect of reaction conditions on the properties and behavior of wood cellulose nanocrystal suspensions. *Biomacromolecules* **2005,** 6, 1048–1054.
26. Araki, J.; Wada, M.; Kuga, S.; Okano, T. Flow properties of microcrystalline cellulose suspension prepared by acid treatment of native cellulose. *Colloids and Surfaces, A: Physicochemical and Engineering Aspects* **1998,** 142, 75–82.
27. Chapter 5.
28. Scales, P. J.; Grieser, F.; Healy, T. W. Electrokinetics of the Muscovite Mica Aqueous-Solution Interface. *Langmuir* **1990,** 6, 582–589.
29. Gu, Y. G.; Li, D. Q. The zeta-potential of glass surface in contact with aqueous solutions. *Journal of Colloid and Interface Science* **2000,** 226, 328–339.
30. Dong, H.; Carr, W. W.; Morris, J. F. An experimental study of drop-on-demand drop formation. *Physics of Fluids* **2006,** 18, 072102.
31. Deegan, R. D.; Bakajin, O.; Dupont, T. F.; Huber, G.; Nagel, S. R.; Witten, T. A. Capillary flow as the cause of ring stains from dried liquid drops. *Nature* **1997,** 389, 827–829.

32. Deegan, R. D.; Bakajin, O.; Dupont, T. F.; Huber, G.; Nagel, S. R.; Witten, T. A. Contact line deposits in an evaporating drop. *Physical Review E* **2000,** 62, 756–765.
33. Schreckenbach, A. Macroscopic structures in liquid crystal systems prepared with spin coating. *Polymer* **1997,** 38, 3069-3083.

Chapter 8

Conclusions

Conclusions

In light of the research results described in Chapters 3 through 7 and with respect to the objectives of this project given in Chapter 1, the following conclusions can be drawn. Cellulose nanocrystals derived from wood pulp by sulfuric acid hydrolysis are not cylindrical, as frequently assumed, but have a tabular morphology with a width-to-thickness ratio of approximately 3:1. The length and width distributions are broad, positively skewed, and have mean values of approximately 116 and 13 nm, respectively. The thickness distribution is narrow, nearly normal, and has a mean value of slightly over 4 nm. Light scattering-based size analysis methods overestimate the length and diameter of cellulose nanocrystals. Aqueous suspensions of cellulose nanocrystals are Newtonian fluids at low nanocrystal concentrations and shear thinning at higher concentrations. For printing with a commercial, drop-on-demand, piezoelectric inkjet printer, cellulose nanocrystal suspensions should have a concentration of 1 wt % or less. The surface properties of soda–lime–silica glass substrates depend strongly on the substrate cleaning procedure. Cleaning with a detergent solution results in an increased surface free energy, polarity, and ζ-potential, compared to untreated glass substrates. Cleaning with aqua regia results in a reduced surface polarity and surface roughness and an increased negative ζ-potential. Cleaning with an organic solvent mixture results in a reduced surface free energy and polarity, an increased surface roughness, and a slightly increased negative ζ-potential. Glass substrates with an even lower surface free energy and polarity can be obtained by grafting of poly(ethylene glycol) molecules to the surface of the glass substrate. The molecular interactions between cellulose nanocrystals and the substrate surfaces as well as the degree of definition of the printed micropatterns can be controlled by tailoring the surface properties of the substrate. A high surface free energy and polarity promotes coalescence of the inkjet-deposited droplets, leading to poorly defined micropatterns. A low surface free energy and polarity, on the other hand, limits droplet coalescence and, thus, prevents the formation of continuous lines in the micropattern. In addition to the surface free energy and polarity, other factors seem to play a role in the formation of the inkjet-printed micropatterns. If these factors can be identified and controlled, inkjet deposition of CNCs could become an attractive method for the fabrication of cellulose micropatterns.